



**Diana de Oliveira Ribeiro**

BSc in Applied Chemistry

**Using Gold Nanoparticles in Protein  
Crystallography:  
Studies in crystal growth and derivatization**

Dissertation for the Master Degree in  
Structural and Functional Biochemistry

Advisor: Maria João Romão, Full Professor, REQUIMTE/CQFB, FCT-UNL  
Co-advisors: Ricardo Franco, Assistant Professor, REQUIMTE/CQFB, FCT-UNL,  
Ana Luísa de Carvalho, Assistant Researcher, REQUIMTE/CQFB, FCT-UNL

**September 2012**



## Acknowledgments

I would like to express a special acknowledgment to Prof. Maria João Romão and Prof. Ricardo Franco for opening their doors to me and this project two years ago, giving me the opportunity to pursue this investigation, and for their guidance and the encouragement through the course of it. I also wish to express my gratitude to Dr. Ana Luísa Carvalho for the all great help and support given during this past year.

I also would like to acknowledge and thank all the members of the Crystallography laboratory, in particular Cecília Bonifácio and Dr. Abhik Mukhopadhyay for all the big help given, and the Bionanotechnology laboratory, especially Cláudia Couto for all the moral support and friendship and also to Dr. Inês Gomes, Inês Osório and João Luz for their assistance when I needed.

To Dr. Pedro Quaresma, from Departamento de Química e Bioquímica, Faculdade de Ciências da Universidade do Porto, I express my great appreciation for the collaboration with the TEM experiments and the functionalization of AuNPs. I also express my appreciation to Dr. Patrícia Carvalho, from MicroLab - Laboratório de Microscopia Electrónica do Instituto Superior Técnico, Universidade Técnica de Lisboa, for kindly providing time for the TEM equipment.

I thank Prof. Teresa Avilez and Dr. Christophe Fliedel, from Faculdade de Ciências e Tecnologia, Universidade Nova de Lisboa, for their collaboration with the Au(I) synthesis. To Dra. Magdalena Kowacz, from Instituto de Tecnologia Química e Biológica, I thank for the availability and help given regarding the crystallization condition of RNase.

Finally, I wish to express very special words of acknowledge to my mother, for the endless support and belief in me, without it would not have been possible for me to achieve this point. I acknowledge all my family, friends and master course colleagues, as well. To Nuno, I endlessly thank for all the kind support and also great patience through what it has been a difficult but very fulfilling year of hard work.



## Abstract

In the field of protein structural analysis, X-ray crystallography plays a major role to expand the knowledge on how proteins function, as well as their interactions with other molecules. However, several obstacles can be present when attempting to grow protein crystals and subsequently determine its structure. Therefore, strategies that facilitate the production of suitable crystals for X-ray diffraction techniques, such as nucleating agents, or that allow overcoming the phase problem, as the production of heavy atom derivatives, are highly sought for. Additionally, coupling gold nanoparticles (AuNPs) with proteins is of emerging interest and a field that has been growing in recent years, for the development of bionanosystems that benefit of the advantages presented by AuNPs. Understanding these processes at the atomic level, would facilitate the study of the interactions between proteins and AuNPs, and allow a deeper insight into these bionanosystems for their development and optimization.

The number of studies reported in the literature combining protein crystallography and AuNPs is, up to date, very limited. The work developed in this Dissertation aimed to study the crystallization of proteins in the presence of AuNPs, associated to the study of its structural interactions with the AuNPs and gold atoms, and also to investigate the hypothesis of producing gold derivatives of protein crystals using AuNPs. To accomplish this, crystallization studies of HEWL (hen egg-white lysozyme) were carried out in the presence of gold nanoparticles capped with Polyvinylpyrrolidone (AuNP-PVP) and in the presence of a Au(I) compound. X-ray diffraction data from the resultant crystals were then measured at one of the X-ray absorption edges of gold, in order to take advantage of the gold's scattering properties. HEWL structures were then determined exhibiting several binding sites for gold atoms at the protein's surface that were unambiguously identified by recurring to an electron density map calculated from the anomalous differences of the measured intensities. In addition, TEM analyses were carried out to verify the assembly and formation of the AuNPs within HEWL crystals. Zeta-potential and optic spectroscopic measurements were also used to study the AuNP-PVP stability alone and in solution with HEWL.

The potential of gold nanoparticles-induced crystal growth was also explored by using differently functionalised AuNPs as nucleant agents in co-crystallization studies with several proteins. Quite positive results were obtained with the test proteins, HEWL and RNase A (ribonuclease A), and a slight improvement of human phenylalanine hydroxylase (PAH) crystallization was also observed.

*Keywords: gold nanoparticles (AuNPs), gold atoms, anomalous scattering, structure determination, HEWL, RNase, PAH.*



## Resumo

No que respeita à análise estrutural de proteínas, a cristalografia de raios-X desempenha um papel fundamental no conhecimento da função das proteínas, bem como das suas interações com outras moléculas. No entanto, podem ocorrer vários obstáculos nas etapas de cristalização de proteínas e determinação da sua estrutura. Como tal, requerem-se estratégias que facilitem a produção de cristais adequados para as técnicas de difração de raios-X, tais como agentes de nucleação, ou que permitam superar o problema da fase, tal como a produção de derivados de metais pesados. Adicionalmente, verifica-se, nos últimos anos, um interesse crescente no acoplamento de nanopartículas de ouro (AuNPs) com proteínas, com vista ao desenvolvimento de bionanosistemas que tiram partido das vantagens que as AuNPs possuem. Entender estes processos ao nível atómico, facilita o estudo das interações entre proteínas e AuNPs, proporcionando um melhor conhecimento para o desenvolvimento e optimização dos bionanosistemas.

A quantidade de estudos que combinem a metodologia da cristalografia de proteínas com AuNPs é muito limitada. Tendo em conta este facto, este trabalho teve como objetivos a cristalização de proteínas na presença de AuNPs, associada ao estudo das interações estruturais com as AuNPs e átomos de ouro, e ainda o estudo da viabilidade de produção de derivados de cristais de proteínas com ouro utilizando AuNPs. Com esta finalidade, foram realizados estudos de cristalização de HEWL (lisozima da clara de ovo de galinha) na presença de AuNPs funcionalizadas com polivinilpirrolidona (AuNP-PVP) e na presença de um composto de Au(I). A difração dos cristais assim resultantes foi medida por técnicas de difração de raios-X a comprimentos de onda coincidentes com a absorção de raios-X pelos átomos de ouro, a fim de tirar partido das propriedades anómalas destes átomos. As estruturas dos complexos foram assim resolvidas, exibindo vários sítios de ligação a átomos de ouro na superfície da proteína. A presença dos átomos de ouro foi identificada de forma inequívoca por recurso ao cálculo de mapas de densidade electrónica usando as diferenças anómalas das intensidades medidas. Análises de TEM foram realizadas para verificar a deposição e a formação de AuNPs no interior dos cristais de HEWL. Foram ainda realizadas medições de potencial-zeta e de espectroscopias ópticas para o estudo da estabilidade AuNP-PVP em solução, isoladas e na presença de HEWL.

Por último, o potencial da indução do crescimento de cristais de proteínas foi explorado usando AuNPs (funcionalizadas com diferentes ligandos) como agentes nucleantes, em estudos de co-cristalização com diferentes proteínas. Foram assim obtidos resultados positivos com as proteínas de teste, HEWL e ribonuclease A (RNase A), sendo também observado uma ligeira melhoria da morfologia dos cristais de phenylalanina hydroxylase (PAH).

*Palavras chave: nanopartículas de ouro, átomos de ouro, sinal anómalo, determinação da estrutura, HEWL, RNase, PAH.*





## Table of Contents

Acknowledgments .....	III
Abstract .....	V
Resumo .....	VII
Table of Contents .....	IX
Index of Figures.....	XIII
Abbreviations.....	XV
<b>CHAPTER 1 .....</b>	<b>1</b>
<b>Introduction.....</b>	<b>1</b>
1.1. Protein crystallography .....	3
1.2. The importance of anomalous scattering and heavy metals in protein structure determination .....	7
<i>Heavy metals and isomorphous replacement in structure determination.....</i>	<i>9</i>
1.3. The role of gold nanoparticles in biochemistry .....	10
<i>AuNPs functionalization .....</i>	<i>12</i>
<i>Biofunctionalization .....</i>	<i>14</i>
1.4. The chemical properties of atomic gold .....	14
1.5. Techniques to study interactions between proteins and gold nanoparticles .....	15
<i>UV-visible spectroscopy.....</i>	<i>15</i>
<i>Zeta potential .....</i>	<i>16</i>
<i>Agarose gel electrophoresis.....</i>	<i>16</i>
<i>Transmission Electron Microscopy (TEM) .....</i>	<i>17</i>
1.6. Proteins used as control subjects in the crystallization studies .....	17
<i>Hen Egg White Lysozyme (HEWL).....</i>	<i>17</i>
<i>Ribonuclease A (RNase A) .....</i>	<i>18</i>
1.7. State-of-the-art .....	19
<b>CHAPTER 2 .....</b>	<b>23</b>
<b>Materials and Methods.....</b>	<b>23</b>
2.1. Gold and gold nanoparticles solutions synthesis .....	25
2.1.1. AuNP-PVP synthesis .....	25
2.1.2. Au(I) synthesis .....	25

2.1.3. AuNP-MUA, AuNP-CALNN, AuNP-CALKK and AuNP-SPEG synthesis and functionalization .....	26
2.2. Protein crystallization studies.....	26
2.2.1. Co-crystallization experiments .....	27
<i>HEWL and RNase with AuNP-PVP</i> .....	27
<i>HEWL with Au(I)</i> .....	27
2.2.2. Soaking experiments.....	27
2.2.3. Crystallization studies using AuNPs as nucleating agents .....	27
2.2.4. Cryogenic protection of the crystals .....	28
2.3. Structure determination.....	28
2.3.1. X-ray diffraction and data collection.....	28
2.3.2. Data processing, structure refinement and gold atoms position determination .....	29
2.4. TEM analysis.....	29
2.5. AuNP-PVP stability and interactions studies with HEWL .....	29
2.5.1. Spectrophotometric analysis .....	29
<i>Stability study of the AuNP-PVP solution</i> .....	30
<i>Stability study of the AuNP-PVP in solution with HEWL</i> .....	30
<i>Stability study of the AuNP-PVP in solution with RNase crystallization condition</i> .....	30
2.5.2. Agarose gel electrophoresis .....	30
2.5.3. Zeta potential analysis .....	30
<b>CHAPTER 3</b> .....	33
<b>Results and Discussion</b> .....	33
3.1. Project I .....	35
Incorporation of gold nanoparticles within protein crystals .....	35
3.1.1. Studies with HEWL .....	37
3.1.1.1. Co-crystallization experiments .....	37
3.1.1.2. Soaking experiments .....	40
3.1.1.3. TEM analysis.....	41
3.1.1.4. Zeta-potential analysis .....	43
3.1.1.5. Spectroscopic studies .....	44
<i>Stability study of the AuNP-PVP solution</i> .....	44
<i>Stability study of the AuNP-PVP in solution with HEWL</i> .....	45

3.1.1.6. Agarose gel electrophoresis studies .....	47
3.1.1.7. Structural analysis by X-ray crystallography .....	48
<i>Of crystals obtained by co-crystallization experiments with AuNP-PVP</i> .....	48
<i>Of crystals obtained by soaking experiments with AuNP-PVP</i> .....	51
3.1.2. Studies with RNase.....	54
3.1.2.1. Co-crystallization experiments .....	54
3.1.2.2. Soaking experiments .....	55
3.1.2.3. Spectroscopic studies .....	56
3.2. Project II .....	59
Growth of gold nanoparticles within protein crystals .....	59
3.2.1. Co-crystallization experiments .....	61
3.2.2. TEM analysis.....	62
3.2.3. Structural analysis by X-ray crystallography.....	63
3.2.4. Structural comparison between HEWL structures obtained in the presence of AuNP-PVP and Au(I) .....	66
3.3. Project III .....	69
Gold nanoparticles-induced protein crystal growth .....	69
3.3.1. HEWL.....	71
3.3.2. RNase .....	73
3.3.3. Phenyl Alanine Hydroxylase (PAH) .....	74
<b>CHAPTER 4</b> .....	<b>77</b>
<b>Conclusions</b> .....	<b>77</b>
<b>References</b> .....	<b>81</b>
<b>Appendix</b> .....	<b>89</b>



## Index of Figures

<b>Figure 1.1.</b> Illustrative scheme of the hanging-drop vapour diffusion method. ....	3
<b>Figure 1.2.</b> Assembly of unit cells in a three-dimensional crystal lattice. ....	4
<b>Figure 1.3.</b> Location of nucleation zones in a protein crystallization diagram.....	5
Figure 1.4. Schematic representation for the production of X-ray radiation. ....	6
<b>Figure 1.5.</b> Process of protein structure determination by single crystal X-ray diffraction. ....	7
<b>Figure 1.6.</b> Anomalous scattering factors predicted for gold atoms, plotted against other elements that could be found in HEWL crystallization conditions. ....	9
<b>Figure 1.7.</b> Changes in solution colour over time during the AuNPs synthesis by reduction of HAuCl <sub>4</sub> by sodium citrate.....	11
<b>Figure 1.8.</b> AuNP UV-visible spectra of a solution as synthesized and in an aggregated state. ....	11
<b>Figure 1.9.</b> Gold nanoparticle functionalized with MUA. ....	12
<b>Figure 1.10.</b> Chemical structure of pentapeptide CALNN. ....	13
<b>Figure 1.11.</b> Chemical structures of MUA and SPEG ..... ..	13
<b>Figure 1.12.</b> Chemical structure of PVP ..... ..	13
<b>Figure 1.13.</b> Bionanoconjugate of AuNPs functionalized with MUA.....	14
<b>Figure 1.14.</b> Schematic representation of a particle's $\zeta$ -potential <sup>3</sup> . ....	16
<b>Figure 1.15.</b> HEWL tertiary structure (PDB ID 193L). ....	17
Figure 1.16. Crystal lattice structure of tetragonal HEWL crystal. ....	18
<b>Figure 1.17.</b> RNase A tertiary structure (PDB ID 5rsa) ..... ..	19
<b>Figure 1.18.</b> Microscope image of AuNP-assembled HEWL crystal, reported by Takeda et al..	20
<b>Figure 1.19.</b> Microscope images of single crystals of lysozyme grown in the presence of Au(I) at different days of growth. ....	20
<b>Figure 3.1.</b> Microscope images of the HEWL crystals grown in the presence of AuNP-PVP ....	38
<b>Figure 3.2.</b> Microscope images of HEWL co-crystallized with AuNP-PVP at pH ranging from 4 to 10.....	39
<b>Figure 3.3.</b> Microscope images of the HEWL crystals prior to soaking and soaked with 34 nM of AuNP-PVP.....	41
<b>Figure 3.4.</b> Electron micrographs of the AuNP-PVP solution and of the HEWL crystals grown in the presence of AuNP-PVP, previously dissolved in Milli-Q water ..... ..	42
<b>Figure 3.5.</b> Microscope images of HEWL 2D crystals co-crystallized with AuNP-PVP.....	42
<b>Figure 3.6.</b> Electron micrographs of the HEWL-AuNP-PVP 2D crystals at pH 4 and at pH 8 directly placed upon the TEM grid.....	43
<b>Figure 3.7.</b> $\zeta$ -potential measurements of the AuNP-PVP solution at a pH range from pH 4 to pH 10.....	44
<b>Figure 3.8.</b> Absorption spectra of AuNP-PVP solutions measured as function of NaCl's ionic strength and absorption spectra of AuNP-PVP as a function of the solution's pH. ....	45
<b>Figure 3.9.</b> Absorption spectra of AuNP-PVP and HEWL solutions.....	46
<b>Figure 3.10.</b> Agarose gel of AuNP-PVP in solution with different ratios of HEWL AuNP-PVP ..	47
<b>Figure 3.11.</b> Electron density map obtained from one of the HEWL-AuNP-PVP crystals.....	48

<b>Figure 3.12.</b> HEWL three-dimensional structures solved from crystals grown in the presence of AuNP-PVP.....	49
<b>Figure 3.13.</b> Superimposition of HEWL structures determined from the crystals grown in the presence of AuNP-PVP at pH 4 and pH 8. ....	49
<b>Figure 3.14.</b> Crystal lattice of HEWL tetragonal crystals grown in the presence of AuNP-PVP. ....	50
<b>Figure 3.15.</b> Electron density map obtained measured from one of the HEWL crystals soaked with AuNP-PVP .....	51
<b>Figure 3.16.</b> HEWL three-dimensional structures solved from crystals soaked with AuNP-PVP .....	52
<b>Figure 3.17.</b> Superimposition of HEWL three-dimensional structures solved from crystals soaked with AuNP-PVP at pH 4 and pH 8 .....	53
<b>Figure 3.18.</b> Crystal lattice of HEWL tetragonal crystals soaked with of AuNP-PVP.....	53
<b>Figure 3.19.</b> Microscope images of RNase crystals obtained from 50mg/ml of protein in 50mM sodium acetate pH 5.5 using 3 M NaCl and 1.2 M of (NH <sub>4</sub> ) <sub>2</sub> SO <sub>4</sub> as precipitant. ....	54
<b>Figure 3.20.</b> Microscope images of RNase control crystals obtained from 50mg/ml of protein in 50mM sodium acetate pH 5.5 using 3 M NaCl and 1.2 M of (NH <sub>4</sub> ) <sub>2</sub> SO <sub>4</sub> as precipitant and RNase co-crystallized with AuNP-PVP 34 nM in the same conditions .....	55
<b>Figure 3.21.</b> Microscope images of RNase crystals prior to soaking and soaked with AuNP-PVP .....	56
<b>Figure 3.22.</b> Absorption spectra of AuNP-PVP solution prepared in sodium acetate pH 5.5 and the mixture of NaCl and (NH <sub>4</sub> ) <sub>2</sub> SO <sub>4</sub> , in the same proportion of 1:1 as present in RNase crystallization drops prepared with 3 M NaCl and 1.2 M (NH <sub>4</sub> ) <sub>2</sub> SO <sub>4</sub> .....	56
<b>Figure 3.23.</b> Microscope photographs of the HEWL crystals (7x magnification) grown in the presence of Au(I) obtained from 75mg/mL of protein and 35mM of Au(I) in 0.1M sodium acetate pH 4.5, at 20 days, 30 days and 60 days after the drops were prepared. ....	61
<b>Figure 3.24.</b> Electron micrographs of the HEWL crystals grown in the presence of Au(I). ....	62
<b>Figure 3.25.</b> Electron density map obtained from one of the HEWL-Au(I) crystals.....	63
<b>Figure 3.26.</b> Summary of the HEWL structures solved from the crystals grown in the presence of Au(I) after 20, 40 and 60 days of growth .....	64
<b>Figure 3.27.</b> Superimposition of the six HEWL structures solved from the crystals grown in the presence of Au(I) after 20, 40 and 60 days of growth .....	65
<b>Figure 3.28.</b> Crystal lattice of HEWL tetragonal crystals grown in the presence of Au(I) .....	66
<b>Figure 3.29.</b> Superimposition of the HEWL structures solved from the crystals grown in the presence of Au(I) and AuNP-PVP.....	67
<b>Figure 3.30.</b> Microscope images of HEWL crystals grown in the presence of AuNPs.....	72
<b>Figure 3.31.</b> Microscope images of RNase crystals grown in the presence of AuNPs. ....	73
<b>Figure 3.32.</b> Microscope images of PAH crystals grown with optimized crystallization conditions in the presence of AuNPs.....	74

## Abbreviations

Au(I)	$\text{ClAuS}(\text{CH}_2\text{CH}_2\text{OH})_2$
AuNP	Gold nanoparticle
CALKK	Cysteine-Alanine-Leucine-Lysine-Lysine Pentapeptide
CALNN	Cysteine-Alanine-Leucine-Asparagine-Asparagine Pentapeptide
HEWL	Hen Egg White Lysozyme
MUA	Mercaptoundecanoic acid
NP	Nanoparticle
PAH	Phenylalanine Hydroxylase
PVP	Polyvinylpyrrolidone
RNase A	Ribonuclease A
SPEG	2-(1-mercaptoundec-11-yloxy)-ethanol
SPR	Surface Plasmon Resonance
TEM	Transmission Electron Microscopy





# **CHAPTER 1**

---

## **Introduction**



## 1.1. Protein crystallography

X-ray crystallography is the foremost method to acquire atomic resolution for proteins. The limiting step in crystallography is obtaining protein crystals that can be suitable for structure solution, and only proteins that can be crystallized and whose structures can be determined easily are studied<sup>1</sup>.

In order to form a protein crystal, protein molecules must separate from solution and self-assemble into a periodic crystal lattice structure. It normally starts from a protein solution of appropriate high concentration (in the mg/ml range) to which reagents that reduce protein solubility – precipitants – are added. Once the solubility limit of the protein is exceeded, the solution becomes supersaturated and metastable, and if the conditions are favorable and a nucleation site is present, crystals may start to grow<sup>2</sup>.

The most frequently used technique for crystallization experiments is the vapour diffusion technique associated to the Hanging-drop method<sup>2</sup> (Figure 1.1). In this method, a few microliters of the protein solution are mixed with an equal quantity of the reservoir solution containing the precipitant reagent. A drop of the mixed solutions is made upon a silanized glass slide, which covers and seals the reservoir. Since the protein-precipitant mixture in the hanging drop is less concentrated than the reservoir solution, water evaporates from the drop and as a result, the concentrations of both protein and precipitant in the drop slowly increase until the protein solubility reaches its limit. As the drop solution becomes supersaturated, nucleation and phase separation occur, and protein crystals may form<sup>2</sup>.

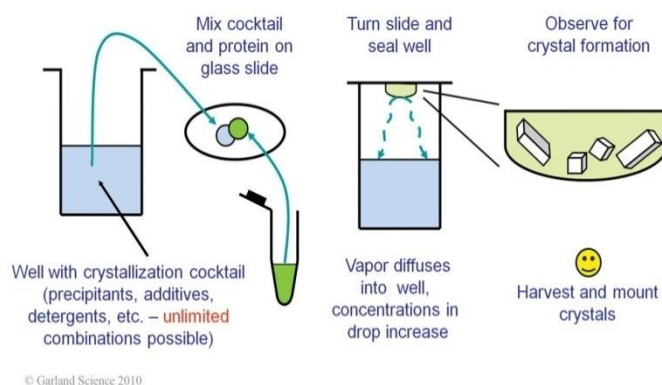


**Figure 1.1.** Illustrative scheme of the hanging-drop vapour diffusion method<sup>2</sup>.

For the purpose of structure determination the growth of a single crystal useful for X-ray diffraction (with size in the range of 50µm to 0.5mm) is important. Single crystals are generally constituted of many growth domains, nearly identically aligned and very often can display sharp edges and well-defined faces<sup>2</sup>.

Protein crystals often form beautiful single crystals, with well-defined edges and crystal faces. However, perfectly formed crystals may not diffract, while unsightly fragments dissected from crystal clusters can produce good diffraction patterns<sup>2</sup>.

Crystals consist of periodic assemblies of fundamental building blocks – unit cells – orderly disposed like solid bricks in a rigid three-dimensional crystal lattice<sup>2,3</sup> (Figure 1.2). These unit cells can either be atoms, small molecules or whole proteins, forming a sparse network of weak intermolecular interactions<sup>2</sup>.

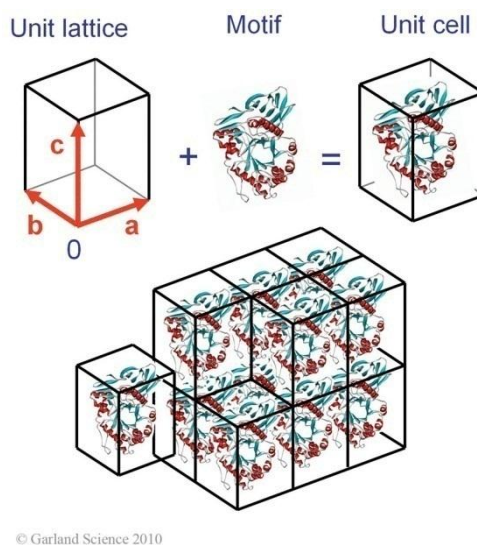


**Figure 1.2.** Assembly of unit cells in a three-dimensional crystal lattice<sup>3</sup>.

Only a limited number of molecular interactions exist forming the network of weak intermolecular forces that keep the large protein molecules connected, such as dipole-dipole, hydrogen bonds, salt bridges, van der Waals contacts and hydrophobic interactions. Interactions have to take place at specific locations on the surface of the protein molecules, in order to self-assemble the molecules into a well-formed, periodic crystal<sup>2</sup>. These intermolecular contacts between the protein molecules are very specific, and inherent of each particular protein<sup>2</sup>.

When protein crystal can be formed, they are generally very fragile, soft and sensitive to environmental variations. As building blocks, proteins consist of long macromolecular chains of twenty different amino acids, often many residues long, which fold into a three-dimensional, irregular shaped protein molecule. Also, proteins frequently present irregular shapes and dangling ends, and disordered termini or flexible loops, are not easily stacked and assembled into a regular, periodic lattice. In addition to the weak intermolecular forces keeping the molecules together in the crystal, the substantial size of protein molecules, and low number of contacts per unit volume, also difficult the crystals' stability. Also, protein crystals contain on average around 50% solvent, mostly disordered in large solvent channels between the stacked molecules, and also along plain rotation axes in the crystal structure<sup>2</sup>.

For any protein crystallization process, the first step is to coerce the protein gently out of the solution, so that in the process of phase separation crystals may form. When the protein solubility limit is exceeded, the solution becomes supersaturated and, given a nucleation event, the excess of protein separates from solution and, in favorable conditions, the molecules may self-assemble into crystals. Solubility-reducing agents or precipitants are however the primary component in this process. The pH of the crystallization cocktail, usually stabilized by a buffer, also determines the level of protein solubility, and shifts the local surface charge distribution of the protein. Temperature also affects protein solubility, which depending on the precipitant composition, may either increase or decrease with temperature. In addition, protein crystallization is an entropy-driven process, and the release of water molecules from across hydrophobic and polar residues during the crystal formation, contributes to the entropy gains of the system<sup>2</sup>.

Initially, in the protein solution, molecules are found in random orientation, surrounded by water and precipitant molecules (Figure 1.3). Interactions between solvent and protein are stronger than among protein molecules themselves. Once the solubility limit is exceeded, the solution becomes metastable. With increase to the supersaturation phase, spontaneous or homogeneous nucleation occurs<sup>2</sup>. During the nucleation stage, the solute protein molecules dispersed in the solvent start to gather into clusters and form stable nuclei. These clusters are stable only if they reach some critical size, which depends on physical conditions, such as supersaturation, temperature and pressure. Once this critical size is reached, the protein crystal will grow spontaneously as long as the solution is in the supersaturated state<sup>4</sup>. Crystal growth stops when the equilibrium is reached or for other kinetics reasons<sup>2</sup>.

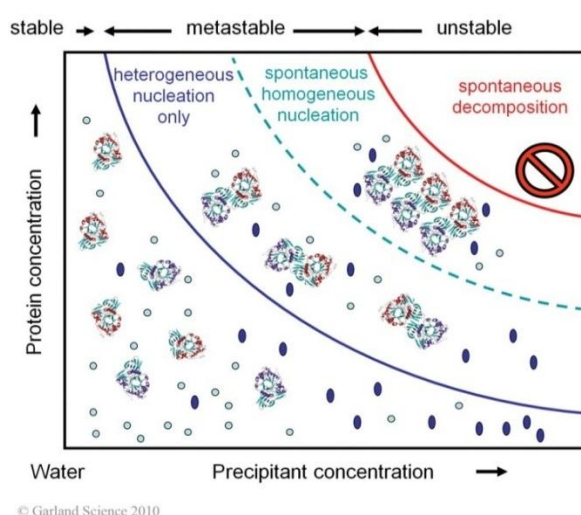


**Figure 1.3.** Location of nucleation zones in a protein crystallization diagram<sup>2</sup>. Nucleant agents showed in blue.

A crystallization experiment generally goes through two different phases of procedure: an initial screening step, which establishes the most promising condition to form crystals; followed by an

optimization step, where the fine-tuning of the initial conditions takes place, in order to obtain well-diffracting crystals for data collection and protein structure solving. The resulting crystals are usually classified as suitable crystals when they display well defined, sharp edges and have similar dimensions<sup>2</sup>.

Once a suitable single crystal with preferably regular, blocky shape, is observed, it is harvested under the microscope and mounted on the X-ray diffractometer. Crystals of about 20-50  $\mu\text{m}$  are considered amenable for synchrotron data collection<sup>2</sup>.

X-rays are composed by electromagnetic radiation ranging from 0.1 to 100  $\text{\AA}$  and can be produced by bombarding a metal target, most often copper, with an electrons beam that is generated by a heated filament and accelerated by an electric field. As a result a high-energy electron then collides with the metal target displacing an electron of the metal from a low-lying orbital and making an electron from a higher orbital to drop to the vacated one. This transition of the electron from an M-shell to a K-shell results in the emission of the electrons' energy in excess in the form of an X-ray photon<sup>5</sup> (Figure 1.4).

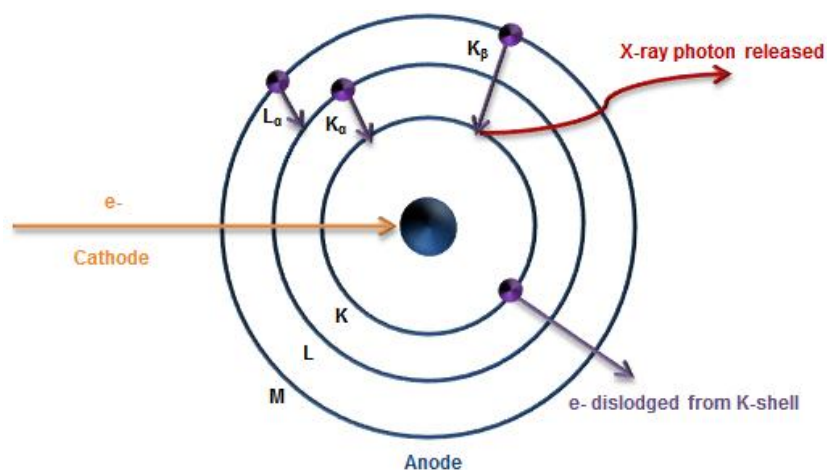


**Figure 1.4.** Schematic representation for the production of X-ray radiation.

By exposing a single crystal of a protein to an X-rays beam, the X-rays are scattered in all directions by the atoms present in the crystal and, from the resulting constructive waves (according to Bragg's law), a set of diffraction spots called reflections is recorded on the detector. Each reflection, results from the electrons transitions of all the atoms in the crystal when they interact with the X-ray, at the same diffraction angle, and contains information from all atoms in the structure<sup>1,6</sup>. The intensities of the reflections in the obtained diffraction images (and after the phases are estimated) permits the calculation of electron density maps and the generation of an initial trace of the model. Multiple cycles of validation, model re-fitting and refinement against the diffraction data and geometric restraints produce a model of the protein<sup>1</sup> (Figure 1.5).

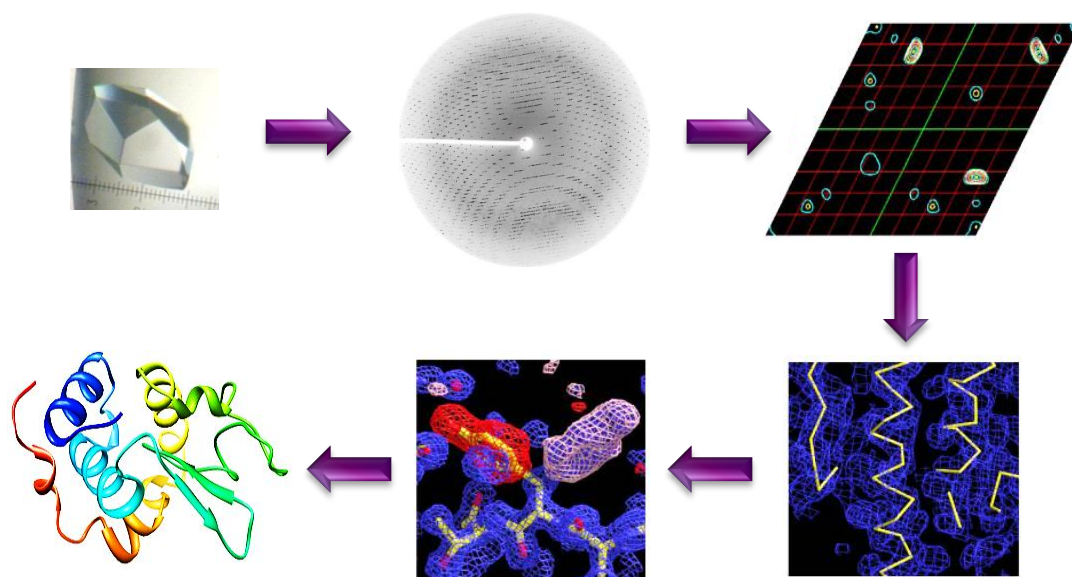


**Figure 1.5.** Process of protein structure determination by single crystal X-ray diffraction, adapted from Pusey *et al.*

## 1.2. The importance of anomalous scattering and heavy metals in protein structure determination

At atomic resolution, the three-dimensional structure of biological macromolecules comprises a set of vectors that describes the positions of all the atoms in the macromolecule relative to an appropriate origin, containing herein the set of interatomic vectors between all pairs of atoms. Anomalous scattering can be used to calculate the interatomic vector magnitudes of selected metal atom pairs, as well as to determine the appropriate positional vectors for a particular metal atom within a macromolecule<sup>7</sup>.

The anomalous, or resonance, X-ray scattering and anomalous diffraction are occurrences resulting from the anomalous dispersion concomitant with the absorption of X-rays from the materials in study<sup>8</sup>. This phenomenon allows determining with great precision the vector positions of particular atoms within a three-dimensional molecular structure. Using heavy atoms for anomalous scattering, the interatomic vectors of the metal atoms can provide the interatomic vector magnitudes, and in doing so allowing to determine the complete three-dimensional structure for the selected atoms involved, at atomic resolution<sup>7</sup>.

Heavy atoms have capacity to absorb X-rays of specified wavelength and, as a result, Friedel's law no longer applies, as the resulting reflections  $(h,k,l)$  and  $(-h,-k,-l)$  are not equal in intensity. The anomalous scattering, or dispersion, is what is called to this disparity in the intensities of symmetry-related reflections<sup>5</sup>.

This change in absorption as a function of the wavelength is termed the absorption edge, and an element exhibits anomalous scattering when the X-ray wavelength is near the element's

absorption edge<sup>8,5</sup>. When these conditions are applied to heavy atoms, a fraction of the radiation is absorbed by the metal and reemitted with altered phase. Light elements, such as carbon, nitrogen and oxygen do not possess absorption edges near the wavelength of X-rays used in protein crystallography, and so do not contribute to anomalous scattering. Conversely, absorption edges of heavy atoms are in this range, which allows the X-ray data to be collected under conditions that makes the most of the heavy atom anomalous scattering<sup>5</sup>.

Furthermore, the electric field vector in X-rays excites electrons to oscillate, and at certain frequencies, electronic resonance occurs and hence energy transfer is possible, occurring a change in the energy level of the electrons. During X-ray absorption not only valence electrons are affected but also the core electron levels. Given that the most tightly bound electrons in inner K-shells absorb at highest energy, and the less tightly electron in higher shells, which generate the L- or M-edges, absorb at lower energies<sup>8</sup>. This means that only heavier elements have higher shells filled and can exhibit L- or M-edges at X-ray energies suitable for diffraction experiments<sup>7,8</sup>.

For incident X-ray energies in the vicinity of the absorption edge, the scattering factor,  $f$ , for an element is no longer just proportional to the atomic number and becomes wavelength or energy-dependent,  $f + f' + f''$ <sup>7,8</sup>. The energy dependence of  $f''$ , the imaginary component<sup>8</sup>, follows that of the absorption edge itself<sup>7</sup>, while  $f'$ , the real component<sup>8</sup>, is the Kramers-Kronig transform of  $f''$ , being generally negative, and has an energy dependence that is approximately symmetrical around the edge<sup>7</sup>. The contribution of the anomalous scattering factor cause changes in both phase and amplitude of an overall acentric structure factor, leading to a disruption of Friedel's Law<sup>8,5</sup> and generating anomalous differences between the symmetry-related reflections which, under these conditions, are designated Bijvoet pairs<sup>8</sup>.

The numerical values of anomalous scattering factors depend on the chemical environment of the dispersive element, so it cannot be accurately calculated without former knowledge<sup>8</sup>. However, for free atoms, the dispersive  $f'$  and anomalous  $f''$  scattering components can be derived through the theoretical approximation developed by Cromer and Liberman. Accurate anomalous scattering factors values can be obtained for the selected elements far from the absorption edge, without accounting for the effects of adjacent atoms<sup>9</sup> (Figure 1.6).



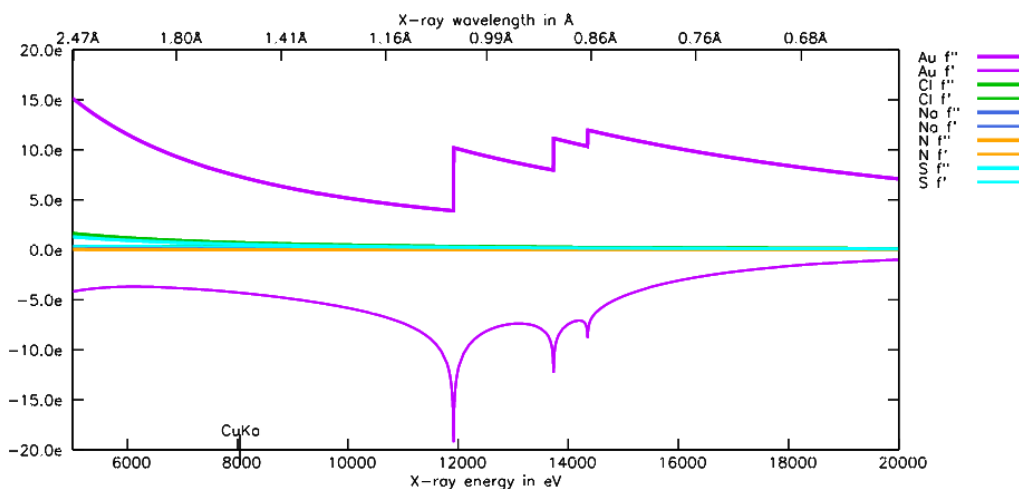


**Figure 1.6.** Anomalous scattering factors predicted for gold atoms (purple line), plotted against other elements<sup>9</sup> that could be found in HEWL crystallization conditions, showing that only gold promotes anomalous diffraction in this X-ray region.

A very important aspect to take into account is that, in order to take advantage of an X-ray anomalous scattering event, the use of energy-tuneable synchrotron radiation sources in the X-ray region is essential. By varying the wavelength of the synchrotron source, X-ray data can be collected under conditions that take the most out of the anomalous scattering by the heavy atoms<sup>7,8,5</sup>.

In the present work, the anomalous scattering promoted by the gold atoms was used to determine with great precision its vector positions within the HEWL three-dimensional molecular structure, at the atomic level, by collecting the X-ray data using synchrotron radiation at a specific wavelength, more precisely, at the  $L_{III}$  edge ( $\lambda=1.04\text{\AA}$ ) of the gold X-ray absorption spectrum.

### ***Heavy metals and isomorphous replacement in structure determination***

Production of heavy metals derivatives is a promising strategy most often used in protein crystallography to obtain high resolution structures and also to overcome the phase problem. Isomorphous replacement is the technique that takes advantage of heavy atoms capability of generating isomorphous differences, besides being a source of anomalous signals<sup>2,5</sup>. This can be achieved either by co-crystallization or soaking experiments<sup>2</sup>. However, an important condition to have in mind is that the heavy atom must not disrupt the crystal packing or the protein's conformation, which means that the derivative must be isomorphous to the native crystal<sup>5</sup>.

By recurring then to the heavy metal anomalous scattering properties, the resulting members of a Friedel pair can be used to calculate the phase of a reflection in the heavy atom derivative data, which then allows calculating the phase of the corresponding reflection in the native

crystal data. This is the principle that is employed by the SIRAS (single isomorphous replacement with anomalous scattering) method of structure determination<sup>5</sup>.

Given that heavy metals play such an important role in protein structure determination, along the course of this project, the possibility of using gold, in the form of AuNPs, as a heavy atom for derivatives production was exploited.

### **1.3. The role of gold nanoparticles in biochemistry**

The interest in nanotechnology has been growing in recent years. Nanotechnology offers great potential for the creation of new materials and devices with a wide range of applications in a variety of areas including medicine, agriculture, and energy. The size-dependent optical, electrical, and magnetic properties of nanoparticles make them promising candidates for bioapplications, namely for *in vivo* imaging, sensing, catalysis, therapeutics, and cell targeting<sup>10</sup>.

Metal nanoparticles present several advantages, such as the control over size and morphology at the nanometer-scale, as well as the ability to be functionalized with different bioactive materials<sup>11</sup>. Gold nanoparticles (AuNPs) have excellent biocompatibility and display unique structural, electronic, magnetic, optical and catalytic properties, which have made them a very attractive material<sup>12</sup>. Their similarity in size with biomolecules such as enzymes, as well as their magnetic and conductive properties, may contribute to the improvement of enzymatic systems<sup>11</sup>. The use of nanoparticles or nanostructured materials for enzymatic immobilization may result in an increase of the apparent enzyme activity<sup>11,13</sup>.

AuNPs have also an exceptionally high absorption coefficient, which allows higher sensitivity in optical detection methods. The strong absorption of AuNPs has been widely used in colorimetric detection of analytes, showing great potential for biodiagnostic tests. In addition to its optical properties, AuNPs catalytic activity has also been used for developing highly sensitive detection methods, as electrochemical detection that can be coupled with enzyme assays<sup>14</sup>.

The AuNPs morphology and surface chemistry can be easily controlled by using appropriate synthetic methods<sup>14</sup>. The most commonly used method for the preparation of spherical AuNPs for use in biological assays is the citrate reduction method of Turkevich et al<sup>14-17,19</sup>. Particles synthesized by the citrate reduction method are nearly monodisperse spheres with size control by the initial reagent concentrations. Although sodium citrate is the most frequently used reducing agent, metal nanoparticles can also be synthesized by the use of borohydride and other reducing agents<sup>12</sup>.

AuNPs synthesized by the citrate reduction method present a negative surface charge as a consequence of the weakly bound citrate capping. Through this aqueous synthesis process, at boiling, the reaction begins immediately after the sodium citrate is added into the HAuCl<sub>4</sub> solution and the reaction can be observed from the changes of the colour of the solution. The

initial colour of the  $\text{HAuCl}_4$  solution is yellow, and soon after addition of sodium citrate the colour changes in sequence to colourless, dark blue and finally red colour<sup>12</sup> (Figure 1.7).

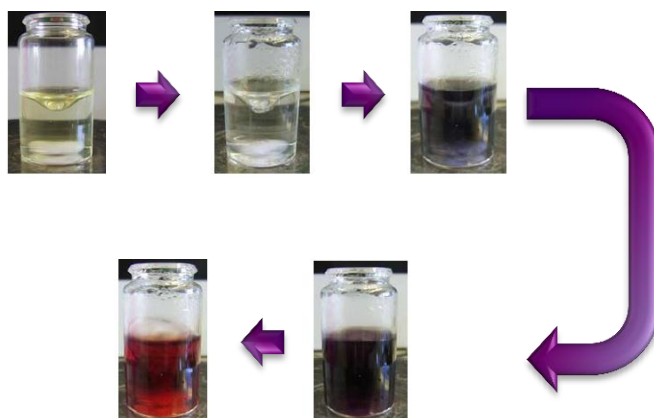


**Figure 1.7.** Changes in solution colour over time during the AuNPs synthesis by reduction of  $\text{HAuCl}_4$  by sodium citrate, adapted from Kurniawan *et al*<sup>12</sup>.

Colloidal solutions of spherical AuNPs with approximate diameters of 10 to 50nm AuNPs exhibit intense absorbance and scattering properties due to surface plasmon resonance (SPR), resulting in the optical absorption maximum around 520 nm responsible for its red colour<sup>19–23</sup>. SPR occurs when the frequency of the exciting light is similar to that of the surface plasmon<sup>19,21,24</sup>. The plasmon band is sensitive to the refractive index in the vicinity of the surface and dependent on the size of the particle, shape, inter-particle distance and the surrounding medium<sup>14,24</sup>, hence explaining the colour changes observed for AuNPs solutions<sup>19–21,24,25</sup>. With the formation of nanoparticle aggregates, plasmon-plasmon coupling occurs which leads to energy loss and a shift of the absorption band towards longer wavelengths (red-shift) as the solution changes in colour from red to blue, or purple<sup>19–21</sup> (Figure 1.8).

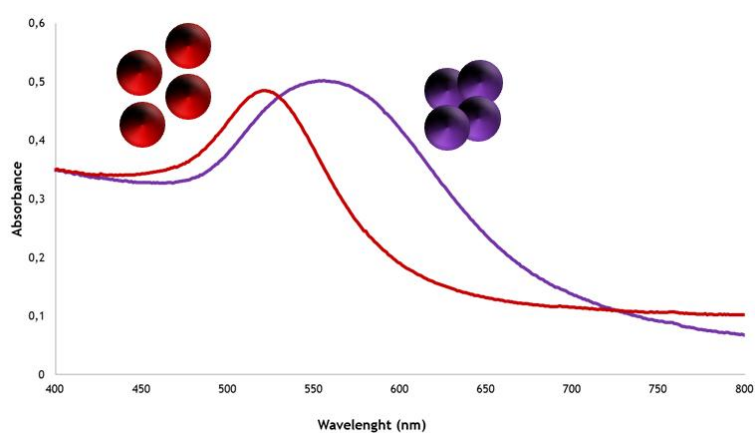


**Figure 1.8.** AuNP UV-visible spectra of a solution as synthesized (red spectra) and in an aggregated state (purple spectra). AuNPs are schematically represented as spheres.

### ***AuNPs functionalization***

Functionalization of AuNPs can be achieved through either chemisorption or physisorption of organic or biological ligands to the AuNPs' surface. In chemisorption, the ligands are adsorbed through the formation of new chemical bonds, where the adsorbed molecules are linked to the surface by valence bonds, characterized by strong interactions between the AuNPs' surface and the ligand. By contrast, physisorption involves intermolecular forces, van der Waals forces, where the perturbation of the electronic states of both AuNPs and ligand are minimal<sup>26,27</sup>.

The use of citrate as a capping agent in the AuNPs syntheses is very advantageous since this labile ligand can be easily replaced by other capping agents bearing an appropriate functionality for binding the biomolecule of interest<sup>14</sup>. Additionally, in order to avoid aggregation of the AuNPs under varying solution conditions, stabilizers made of organic molecules or polymers are often used<sup>18,19,28</sup>.

The most commonly used polymers for the stabilization of AuNPs are polyvinylpyrrolidone (PVP) and poly-(ethylene glycol) (PEG), of different chain lengths<sup>18,19,28</sup>. Gold's natural affinity for sulfur has inspired much scientific interest, since it makes gold and AuNPs a very suitable substrate on which to assemble ordered monolayers of a variety of organic molecules containing –SH groups, mainly alkanethiols<sup>23</sup> (Figure 1.9).

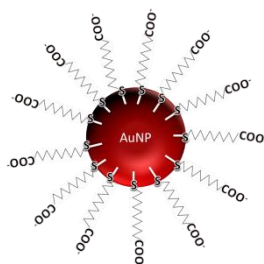


**Figure 1.9.** Gold nanoparticle functionalized with mercaptoundecanoic acid (MUA).

The direct interaction of a protein with the bare AuNPs surface without a spacer can cause steric constraint modifying the protein activity, compared to the protein in solution, and are more likely to cause total or partial protein denaturation and thus decrease its activity<sup>10</sup>.

However, most existing functional nanomaterials lack the degree of internal complexity of proteins, and so the formation of self-assembled monolayers of peptides at the surface of nanomaterials<sup>25</sup> is of great interest. Peptides can be selected, designed and synthesized using standardized methods, and on the other hand AuNPs surfaces can be readily functionalized by using thiolated ligands<sup>25</sup>.

One example is the pentapeptide CALNN (Cysteine-Alanine-Leucine-Asparagine-Asparagine) (Figure 1.10), which converts citrate-stabilized AuNPs into extremely stable, water-soluble AuNP-CALNN with chemical properties analogous to those of proteins<sup>25</sup>. This pentapeptide was

designed in such a manner that the thiol group in the side chain of the N-terminal cysteine is able to establish a covalent bond to the AuNPs. Alanine and Leucine, in positions 2 and 3, possess hydrophobic side chains and promote the self-assembly of the peptide through intermolecular hydrophobic interactions. And Asparagine, in positions 4 and 5, is an uncharged but hydrophilic amino acid due to the amide group on the side chain, and the C-terminal asparagine, in position 5, can bear a negative charge due to the terminal carboxylic group<sup>25</sup>.

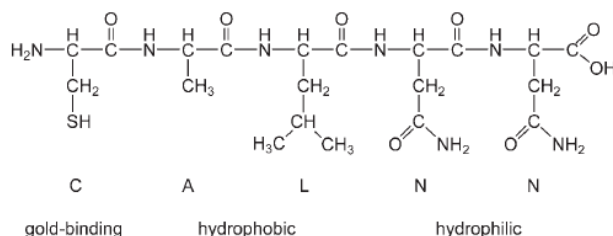


**Figure 1.10.** Chemical structure of pentapeptide CALNN<sup>25</sup>.

In this work and in addition to CALNN, the pentapeptide CALKK, which bears Lysine residues in positions 4 and 5 of the C-terminal, was also used to functionalize AuNPs. Mercaptoundecanoic acid (MUA) (Figure 1.11) was used as a negatively charged capping agent, again bound to the AuNPs by the thiol group, leaving the carboxylic group facing outwards. Finally, thiolated PEG, HSC<sub>6</sub>EG<sub>3</sub>, (SPEG) (Figure 1.11) was also used as a polymer capping agent.

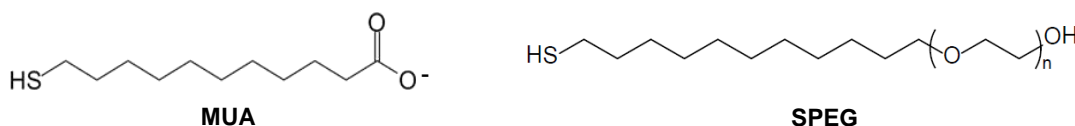


**Figure 1.11.** Chemical structures of MUA and SPEG where the n denotes the polymerization number.

Poly(N-vinylpyrrolidone) (PVP) was also used as a capping agent for AuNPs in the course of this work. PVP is a water soluble biocompatible polymer<sup>29</sup> with a long and soft polyvinyl chain (Figure 1.12) and, as previously stated, it stabilizes AuNPs against agglomeration<sup>18,19,28</sup>, but also promotes metal nucleation, which tends to yield small well-dispersed metal NPs in aqueous phase<sup>30</sup>.

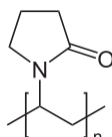


**Figure 1.12.** Chemical structure of PVP, where n denotes the polymerization number.

## **Biofunctionalization**

In order to use AuNPs in biological assays, these can be functionalized with biocompatible ligands, which can have a dual function of preventing their aggregation and promote interaction with biomolecules<sup>10</sup>. The functionalization of AuNPs involves the use of bifunctional ligands in which a moiety is used for anchorage to the nanoparticle (usually a thiol)<sup>14,23</sup>, while the other functional group is directed to the outer-surface for specific interaction with biomolecules<sup>14</sup>, such as proteins.

The interaction between AuNPs surface and proteins, leads to the formation of a protein “corona” around the particles. This protein corona can affect AuNPs properties, including its biological effects, and conversely, AuNPs can effect protein behaviour<sup>10</sup>.

Conjugation of specific biomolecules onto nanoparticle surfaces has an increased interest in the areas of biotechnology and medicine, where it has introduced new advancements in molecular and cellular biology, further leading to vast improvements on *in vivo* gene delivery, clinical diagnosis, medical/cancer imaging and receptor-targeted delivery<sup>10</sup>.

Bioconjugation, by coupling nanoparticles to proteins, is based on the reaction of the proteins' specific and reactive functional groups, such as amino–NH<sub>2</sub> (lysine), carboxylic acid–COOH (aspartic, glutamic), hydroxyl–OH (serine, tyrosine) and –SH (cysteine), with the AuNPs surface, or mainly on electrostatic interactions between the proteins and the AuNPs surfaces. AuNPs are functionalized with bifunctional cross-linker molecules with functional groups such as carboxylic acid, hydroxyl, sulfhydryl and amino groups. Thiolated ligands are widely used to AuNPs functionalization, since gold atoms have strong affinity towards thiol groups forming stable quasi-covalent Au-S bonds<sup>10</sup> (Figure 1.13).

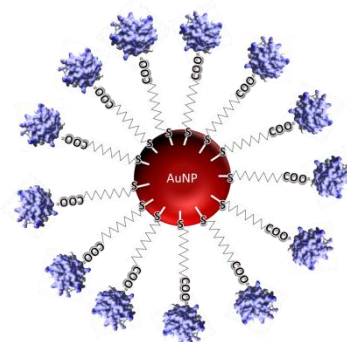


**Figure 1.13.** Bionanoconjugate of AuNPs functionalized with MUA.

### **1.4. The chemical properties of atomic gold**

Gold occupies a unique position among the elements of the periodic table, and its chemical stability, the useful surface chemistry of the materials it generates, and its distinctive optical properties, has made gold an extremely attractive metal to employ in a variety of

technologies<sup>24,23,31</sup>. This is especially true for nanotechnology, as a consequence of these unique properties, it is easier to work with gold at the nanoscale than with any other metal<sup>23,31</sup>.

The reasons that make gold so appealing lie in its special electronic configuration [Xe] 4f<sup>14</sup> 5d<sup>10</sup> 6s<sup>1</sup>, which controls the optical properties, chemical reactivity, and crystal structure. Also, gold's high atomic number confers some other features, independent of its electronic configuration<sup>24</sup>. Native gold is one of the most stable elements available<sup>32</sup>, being also the most electronegative metal on the Pauling scale, with a value of 2.44<sup>24</sup>.

Gold usually has two additional oxidation states, I and III (valency of +1 and +3), besides its metallic ground state (valency 0). Gold(III) is best stabilized by “hard” ligands such as oxygen or nitrogen donors, while gold(I) prefers “softer” sulphur or phosphorus donor ligands<sup>32,33</sup>. However, both gold(III) and gold(I) are easily reduced to metallic gold(0) in the presence of reducing agents and in the absence of ligands capable of stabilizing the gold(I) complexes<sup>33</sup>.

In vivo, gold(I) binds predominantly to proteins and low-molecular weight thiols. For example, 80 to 90% of the extracellular gold in the blood circulation is bound to serum albumin, which is the most abundant plasma protein in humans. This event is due to the fact that albumin is the main source of extracellular thiol groups in the blood. About 10 to 20% is bound to immunoglobulins, proteins that are known to contain an elevated thiol content<sup>34</sup>.

## **1.5. Techniques to study interactions between proteins and gold nanoparticles**

### ***UV-visible spectroscopy***

The UV-visible spectroscopic method is based on the absorption of electromagnetic radiation in the wavelength region of 160 to 780 nm, the ultra-violet and visible regions of the electromagnetic spectrum. The incident energy is transferred to the molecules promoting electrons from ground state states to higher energetic levels, which is then measured in terms of transmittance or absorbance of the solution in study<sup>35</sup>.

In the case of AuNPs colloidal solutions, as mentioned above (subsection 1.3.), the incident light at specific frequencies causes free electrons of gold to resonantly oscillate in the electric field of the light. The light at the resonant frequencies is then absorbed or scattered, due to the SPR, which results in an characteristic plasmon band<sup>19–21,23–25</sup>. AuNPs of 10 to 50 nm of diameter selectively absorb the blue and green light with a maximum of absorbance between 520 and 540 nm, responsible for the solutions' distinctive red colour<sup>19,22,23</sup>. Since the SPR is sensitive to the inter-particle distance and its surrounding medium<sup>15,24</sup>, when AuNPs aggregates, or biomolecules such as proteins conjugate with its surface, a red-shift of the plasmon band occurs resulting in a change of the solution colour towards the blue<sup>19–21</sup>. Is this exact event that makes possible to evaluate possible interactions between the AuNPs and the protein of interest<sup>23</sup>.

## Zeta potential

Light scattering techniques are powerful tools for the characterization of NPs and the conjugates formed thereof and the understanding of their interactions, by the determination of the superficial charge of the functionalized NPs<sup>36</sup>.

Zeta-potential (Figure 1.14) is a physical property exhibited by any particle<sup>37</sup>, which in suspension acquires a charged surface forming an electrical double layer<sup>38</sup>. Its values can be obtained by applying an electric field to the solution and measure the rate of motion of the particles, the electrophoretic mobility ( $\mu E$ ), in a process called electrophoresis. The higher the charge of the particle, the faster it moves in the solution<sup>39</sup>.

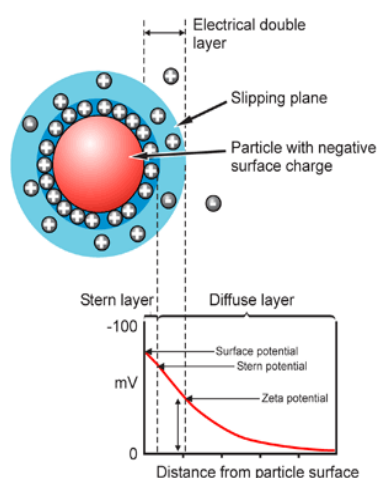


**Figure 1.14.** Schematic representation of a particle's  $\zeta$ -potential<sup>38</sup>.

By measuring the electrophoretic mobility of particles in solution<sup>40</sup>,  $\zeta$ -potential provides an indication of the system long-term stability. If the suspended particles have a high  $\zeta$ -potential, they repel each other and no aggregation occurs, as in the case of AuNPs colloidal solutions. However, if the particles have a low  $\zeta$ -potential value, the repulsion force will not be sufficient to prevent their aggregation. Particles with  $\zeta$ -potential values above +30mV or lower than -30mV, are generally considered stable. Several factors affect the  $\zeta$ -potential exhibited by the particles, especially the pH and ionic strength of the aqueous solution<sup>37</sup>, and so, by measuring the  $\zeta$ -potential values it is possible to understand how those conditions affect the AuNPs.

## Agarose gel electrophoresis

Agarose gel electrophoresis has proven to be a powerful tool in AuNPs research<sup>41–43</sup>. Although agarose gel electrophoresis has been highly employed for biomolecules studies, has been recently applied to the separation and analysis of metal nanoparticles and also to evaluate their conjugation to biomolecules<sup>22,41–45</sup>.



This technique is sensitive to the size, charge, and shape of the AuNPs, having the great advantage of the immediate visual detection of the AuNPs bands without the need for further development. Due to AuNPs characteristic SPR when exposed to light, it is possible to observe the migration of the bands in the gel by its red colour<sup>22,43</sup>. Since the conjugates of AuNPs and biomolecules acquire a different surface charge relative to the AuNPs alone, due to the biomolecule's net charge, agarose gel electrophoresis provides a means of detecting the saturation of the AuNPs with proteins, hence proving bionanoconjugation based on the samples electrophoretic mobility<sup>22,41</sup>.

### **Transmission Electron Microscopy (TEM)**

TEM allows the observation of matter with atomic resolution, in the present case the AuNPs in itself, by shooting electrons through the sample. The changes in the electron beam that arise from scattering by the sample are then measured, producing an image that consists in a projection of the entire object, providing not only direct information about size and shape of the AuNPs but also structural information<sup>46,47</sup>. Nevertheless, this projection is two-dimensional against the viewscreen and so relations in the z-axis between structures are lost. Additionally, TEM samples are required to be thin, otherwise they will absorb too much of the electron beam<sup>46</sup>.

## **1.6. Proteins used as control subjects in the crystallization studies**

### **Hen Egg White Lysozyme (HEWL)**

HEWL (Figure 1.15) is a small (129 amino acid residues) and stable hydrolytic enzyme<sup>48</sup> that forms tetragonal crystals, exhibiting a  $P4_32_12$  space group and different types of solvent channels<sup>49,50</sup>. It was actually the first enzyme to have its three-dimensional structure determined by X-ray diffraction techniques<sup>48,51,52</sup>.

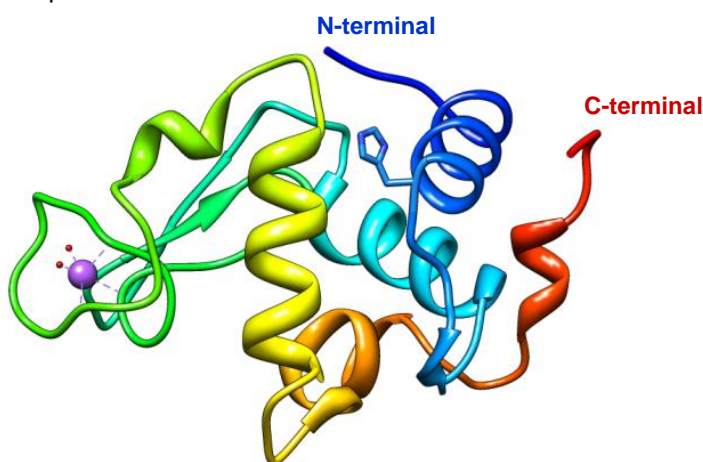


**Figure 1.15.** HEWL tertiary structure (PDB ID 193L) in ribbon representation, drawn with Chimera software, exhibiting its single histidine (His15) and the usual binding spot where Na ions are detected. Water atoms are depicted in red and Na atom in purple. The ribbon colour code varies from N- to C-terminal.

Since HEWL can be easily crystallized in a variety of conditions and pH range, it has been widely used as a model protein for macromolecular crystal growth studies<sup>53</sup> and research into protein structure and function, being the most common protein in the PDB<sup>48</sup>.

HEWL crystals have been known to capture and deposit metal complexes and metal ions when subjected to co-crystallization or soaking techniques<sup>50,54</sup>, and also to function as a biotemplates for preparation of inorganic materials in solution<sup>50</sup>, including metallic nanoparticles<sup>55,56</sup>. These properties of HEWL crystals are due to the presence of coordinating amino acid residues within the pore surfaces (Figure 1.16), such as histidine, lysine, aspartate, and glutamate<sup>50</sup>.

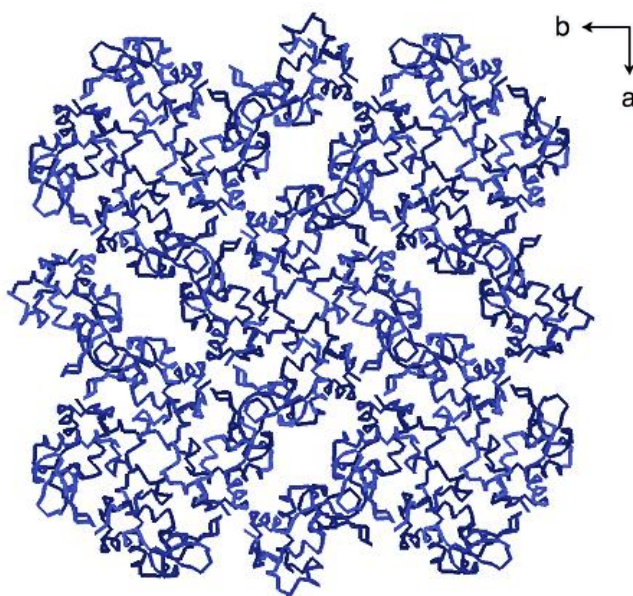


**Figure 1.16.** Crystal lattice structure of tetragonal HEWL crystal, showing its different types of solvent channels.

Over half of the metal-containing HEWL structures deposited on the PDB includes metals bound to the protein through the N $\epsilon$  of the single histidine (His15)<sup>57</sup>, various being transition metals such as Au(I), Ag(I), Mn(II), Pt(II), Re(I), Ru(II) and Rh(III)<sup>50,54,57-59</sup>. Moreover, interaction between HEWL and metal ions have also been observed to occur through asparagine and arginine residues<sup>50,54,57</sup>.

### ***Ribonuclease A (RNase A)***

Bovine pancreatic RNase A (Figure 1.17) is a small (124 amino acid residues) and remarkably stable protein, with four disulphide bonds that are critical to the stability of the native enzyme<sup>60,61</sup>. RNase A was first crystallized by Moses Kunitz in 1940<sup>62,63</sup>, being the third enzyme and fourth protein (after myoglobin, lysozyme and carboxypeptidase A) whose three-dimensional structure was solved by X-ray diffraction techniques<sup>61</sup>.

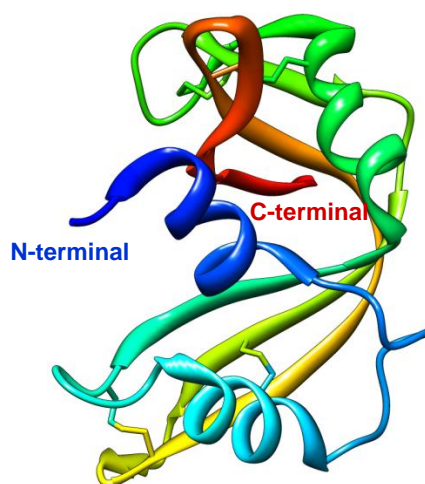


**Figure 1.17.** RNase A tertiary structure (PDB ID 5rsa) shown in ribbon representation, drawn with Chimera software, exhibiting its four disulphide bonds. The colour code varies from N- to C-terminal.

RNase A is, perhaps, the best-studied enzyme of the XX<sup>th</sup> century<sup>62,63</sup>, as it has been the object of ground-breaking work on the folding, stability, and chemistry of proteins and in enzymology and in molecular evolution as well<sup>61</sup>. For this reason, this enzyme was chosen as a subject of study in this work, in parallel with HEWL.

### 1.7. State-of-the-art

So far, the number of studies reported in the literature combining protein crystallography and AuNPs, especially to study proteins interaction with the AuNPs, is very limited.

Takeda *et al.*, developed a method for the three-dimensional assembly of PVP-stabilized AuNPs into HEWL crystals<sup>64</sup>. The assembling of AuNPs into the crystals was evidenced by the appearance of a red coloured hourglass-shape within the crystals (Figure 1.18). Their results showed that the AuNPs tended to be incorporated in the  $\{1\ 0\ 1\}$  sectors of HEWL crystals, more than in  $\{1\ 1\ 0\}$  sectors. It was also observed that the central region of the  $\{1\ 0\ 1\}$  sector contained a larger amount of the nanoparticles than the peripheral region of the same sector due to the depletion of AuNPs throughout the experiment, as the concentration of AuNPs decreases as the crystal grows. The authors suggested that the AuNPs were assembled into the crystals by electrostatic interaction between the AuNPs and HEWL's crystal surface. This electrostatic interaction at the  $\{1\ 0\ 1\}$  surface would be larger than that at  $\{1\ 1\ 0\}$  surface, due to the large contact area between the AuNPs and the  $\{1\ 0\ 1\}$  surface. As a result, the amount of AuNPs incorporated in the  $\{1\ 0\ 1\}$  sectors would be larger than that in  $\{1\ 1\ 0\}$  sectors<sup>64</sup>.

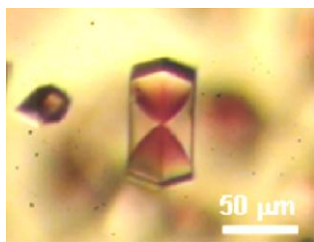


**Figure 1.18.** Microscope image of AuNP-assembled HEWL crystal, reported by Takeda *et al.*<sup>64</sup>.

Also, Wei *et al.*, have reported that intact single crystals of HEWL can be used to study the time-dependent, protein-directed growth of AuNPs<sup>56</sup>. The AuNPs were synthesized from HEWL and  $\text{ClAuS}(\text{CH}_2\text{CH}_2\text{OH})_2$  (Au(I)) using an *in situ* approach. This approach significantly retarded AuNPs growth, allowing the authors to monitor the time-dependent reaction. The crystals gradually changed from the initial colourless to pink, then to red as growth proceeded (Figure 1.19). The colour evolution observed would be originated from the characteristic SPR absorption of AuNPs, hence indicating the growth of AuNPs inside the crystals. The authors hypothesize that the AuNPs' growth could be created from the spontaneous disproportionation of Au(I) to Au(III) and Au(0), followed by accumulation of Au(0) into gold nanoparticles within the crystal. Time-dependent, high-resolution X-ray crystallographic structures of those crystals were obtained at different growth stages. The authors observed an increasing number of gold atoms binding to the protein, namely coordinated by the N $\epsilon$  of the protein's His 15<sup>56</sup>.

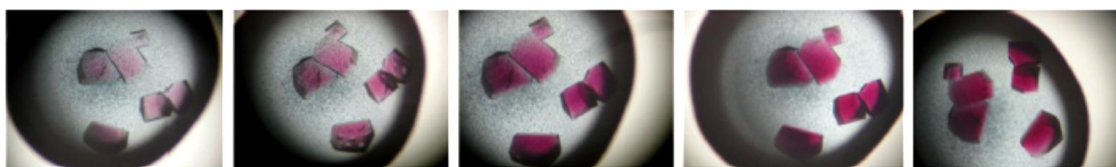


**Figure 1.19.** Microscope images of single crystals of lysozyme grown in the presence of Au(I) at different days of growth, reported by Wei *et al.*<sup>56</sup>.

In parallel studies, efforts have been made on the search for an optimal nucleant to reduce the nucleation energy barrier, and optimize the growth of suitable crystals. Hodzhaoglu *et al.*, have described that AuNPs are effective nucleants for HEWL crystallization<sup>4</sup>. Their study revealed an increase of the nucleation number of HEWL in the presence of as synthesized AuNPs and AuNPs functionalized by alkylthiol with  $\text{COOH}^-$  terminated groups. Their results suggested that AuNPs induced the crystallization of HEWL and also of ferritin. It was claimed that the fact that this technology had worked with such diverse proteins as HEWL and ferritin, could suggest that it might also be applicable for many other proteins, including those which are reluctant to crystallization by known technologies<sup>4</sup>.

In a previous project carried out in 2010, at the light of Hodzhaoglu *et al.* results, crystallization studies of HEWL were carried out in the presence of AuNPs functionalized with different

ligands<sup>65</sup>. The objective of this project was to attest the use of the AuNPs as nucleating agents and if improvement of the crystal growth could be achieved. It was demonstrated that, for some specific conditions, AuNPs could actually act as nucleating agents for HEWL crystallization, promoting its crystal growth in conditions for which the enzyme alone was not able to form crystals. An increase in crystal size was also observed, namely with AuNP-CALNN and AuNP-CALKK<sup>65</sup>.

This project was further explored in the course of the present study, in order to confirm those results and application to other proteins less prone to crystallization, or to give well-diffracting crystals. One further interest was to study the production of gold-derivatized protein crystals, useful in three-dimensional structure solution by isomorphous replacement methods, added to the possibility of using the anomalous scattering of gold atoms.



## **CHAPTER 2**

---

### **Materials and Methods**





Along this chapter, the experimental procedures recurred in the course of this work will be described. Unless otherwise stated, reactants used were purchased from Sigma-Aldrich (Sintra, Portugal), with the highest purity available. Equipment suppliers are identified where is relevant.

## 2.1. Gold and gold nanoparticles solutions synthesis

Before each synthesis all glassware was cleaned with *acqua regia* followed by extensive washing with Milli-Q water until all the acid was neutralized.

The concentration of the AuNPs solutions was always determined using Haiss *et al.* method<sup>66</sup>

### 2.1.1. AuNP-PVP synthesis

Gold nanoparticles capped with polyvinylpyrrolidone (PVP) were synthesized by reduction of  $\text{HAuCl}_4$  by  $\text{NaBH}_4$ , adapted from Takeda *et al.*<sup>64</sup> procedure. 56 mg of PVP K-30 were added to 5 mL of 1mM  $\text{HAuCl}_4$  aqueous solution. Under stirring, 0.5 mL of 10 mM  $\text{NaBH}_4$  aqueous solution was then added to the mixture. The solution immediately changed colour from yellow to brownish red. The synthesis was kept stirred overnight, at room temperature, where its colour changed to a final deep red. The PVP-stabilized AuNPs solution hence produced was dialyzed overnight using a cellulose membrane with a 12-14 kDa cutoff. The resultant AuNP-PVP solution was characterized by UV-Vis and then stored at 4°C until further use. In order to achieve higher concentrations, the AuNP-PVP solution was concentrated using Milipore centrifugal filter units (100 MWCO) for 10 minutes at 3600 rpm (Eppendorf, Centrifuge 5810 R).

### 2.1.2. Au(I) synthesis

$\text{ClAuS}(\text{CH}_2\text{CH}_2\text{OH})_2$  synthesis was performed in collaboration with Dr. Teresa Avilez research group (REQUIMTE, Faculdade de Ciências e Tecnologia, Universidade Nova de Lisboa), by Dr. Christophe Fliedel, based on McCleskey *et al.*<sup>67</sup> method. Au(I) synthesis was accomplished by adding two equivalents of 2,2-thiodiethanol ( $\text{S}(\text{CH}_2\text{CH}_2\text{OH})_2$ ) to 50 mL of 1g of  $\text{HAuCl}_4$  aqueous solution, under stirring, recurring to a Schlenk filtration under nitrogen atmosphere. The resultant white powder was recrystallized with ethanol/ether and stored at -4°C in an ether suspension until further use. Before its use, Au(I) powder was dried under nitrogen atmosphere, weighted, with minimal contact with oxygen as possible, and used immediately afterword by dissolving 0.035 g in 1 mL of sodium acetate pH 4.5 buffer. If exposed to oxygen, the powder would become brown due to oxidation of Au(I) and no longer be suited to use.

### **2.1.3. AuNP-MUA, AuNP-CALNN, AuNP-CALKK and AuNP-SPEG synthesis and functionalization**

Spherical AuNPs were synthesized by the *Turkevich* method with minor modifications<sup>16,17</sup>, where  $\text{HAuCl}_4$  is chemically reduced by citrate. A solution containing 62.5 mL of Milli-Q water and 43  $\mu\text{L}$  of a 30% wt gold salt solution was heated until boiling under reflux, using a sand-bath, always under stirring. At this point 6.25 mL of 36.8 mM sodium citrate solution was quickly added. The solution then changed from the gold complex characteristic yellow colour to colourless, then to black and finally to red. Heating and stirring was continued for another 15 minutes, and nanoparticle colloid was cool down to room temperature. The resultant AuNPs solution was characterized by UV-Vis and stored at 4°C until further use.

These citrate stabilized AuNPs solution were then functionalized with four different capping agents: mercaptoundecanoic acid (MUA), pentapeptide CALNN (CASLO Laboratory), pentapeptide CALKK (CASLO Laboratory) and the thiolated PEG (SPEG)  $\text{HSC}_6\text{EG}_3$  (Prochimia Surfaces). These ligands hold thiol groups which a great affinity for the gold surface, easily replacing the citrate's carboxylic groups. The functionalization with the latter two ligands was performed by Dr. Pedro Quaresma (REQUIMTE, Departamento de Química e Bioquímica, Faculdade de Ciências da Universidade do Porto). The functionalization with MUA and CALNN was carried out by incubating the AuNPs solution with the ligand, for at least 30 minutes at 4°C, at a molar ratio of 1:5000 using 10 mM MUA stock solution in ethanol and 1:1000 from 5 mM CALNN stock solution.

## **2.2. Protein crystallization studies**

Experiments with HEWL were performed using Lysozyme from hen egg-white (EC 235-747-3). For each test, fresh enzyme was dissolved in the appropriate buffer solution regarding each experiment. Pancreatic ribonuclease A (EC 3.1.27.5) was used for studies with RNase, prepared in 50 mM sodium acetate buffer at pH 5.5. The remaining proteins (malectin, malectin-trime, native AOH, AOH- $\Delta\text{His}$  and mutants Y885M and Y885F, YPS and PAH) were kindly provided by work colleagues, as part of their research projects, to be used as subjects in the induction of crystallization conditions studies. Milli-Q water was always used for the preparation of aqueous solutions.

All the crystallization experiments were performed according to the hanging drop method, using 24-well crystallization boxes, at 20°C. The crystallization boxes were kept at 20°C. Observation of the drops was made through an optical microscope (*Olympus SZH10 Research Stereo* microscope, with an Olympus DF Plan Apo IX objective). A 5x magnification was used for the measurement of the crystals size. Photographs of the crystals were taken using a digital camera and, in some cases, an Olympus KPO polarizer lens.

### **2.2.1. Co-crystallization experiments**

#### ***HEWL and RNase with AuNP-PVP***

Drops of HEWL and AuNP-PVP were made using 35 mg/mL of protein and 34 nM AuNP-PVP, in a pH range from 4 to 8. Samples were prepared in buffer solutions at 50mM of concentration using: sodium acetate buffer for pH 4 and pH 5, sodium phosphate buffer for pH 6 and pH 7, boric acid buffer pH 8, Tris buffer for pH 9 and glycine/NaOH for pH 10. 5% NaCl was used as precipitant agent and 700  $\mu$ L were added to the well. Drop setups of RNase were made at 50 mg/mL of protein and 34 nM AuNP-PVP, in 50mM sodium acetate buffer pH 5.5, using 1 mL of a mixture of 3 M NaCl and 1.2 M  $(\text{NH}_4)_2\text{SO}_4$  as precipitant agent added to the well. Drop setups of AuNP-PVP and protein solutions were performed using a sample:precipitant ratio of 1:1, to a total volume of 4  $\mu$ L. 2D HEWL crystals with AuNP-PVP were grown using the same conditions described above for HEWL, but by spreading the drop along the glass slide with the help of a pipette tip. HEWL and RNase control crystals were also grown. HEWL crystals were formed within 24 hours and RNase crystals in three days.

#### ***HEWL with Au(I)***

HEWL crystals were grown in the presence of the synthesized Au(I) compound by using 5  $\mu$ L of 75 mg/mL HEWL in 0.1 M sodium acetate pH 4.5 mixed with 3  $\mu$ L of 35 mM Au(I) in 0.1 M sodium acetate pH 4.5, at room temperature and incubated for 30 minutes. Drops were set up by mixing 7  $\mu$ L of HEWL and Au(I) mixture and 3  $\mu$ L of the well precipitant solution. As precipitant solution it was used 6.5% NaCl (w/v) in 0.1 M sodium acetate pH 4.5, filling the well with 800  $\mu$ L. HEWL control crystals were also grown. Crystals took up to a week to grow and 20 days for colour to be detected within the crystals.

### **2.2.2. Soaking experiments**

Native HEWL and RNase crystals were grown according to the method described above for the co-crystallization experiments with AuNP-PVP. After crystals were detected, one day for HEWL and three days for RNase, AuNP-PVP was added to the drops to a final concentration of 34 nM. 24 hours later, HEWL crystals exhibited a red colouration.

### **2.2.3. Crystallization studies using AuNPs as nucleating agents**

These experiments were carried with AuNP-MUA, AuNP-CALNN, AuNP-CALKK and AuNP-SPEG at a concentration of 3 nM. Solutions of each AuNPs and protein were incubated together, overnight at 4°C. For each condition tested, control drops of protein were always performed.

Drop setups of HEWL were made at 15 and 25 mg/mL of protein concentration in 50mM sodium acetate buffer pH 4.5, using 700  $\mu$ L of 0.5 M NaCl as precipitant agent in the reservoir. Drops of RNase were made at 50 mg/mL of protein concentration in 50mM sodium acetate buffer pH 5.5, using 1 mL of a mixture of 3 M NaCl and 1.2 M  $(\text{NH}_4)_2\text{SO}_4$  as precipitant agent added to the well. Drops of the incubated AuNPs and protein solutions were performed using a 1:1 ratio of sample:precipitant, to a total volume of 4  $\mu$ L.

PAH drops were performed at protein concentrations of 5 and 8.6 mg/mL in 0.1 M HEPES buffer pH 7.5, using 500  $\mu$ L of 1 M sodium-potassium tartrate as precipitant agent added to the well. Drops of the incubated AuNPs and PAH solutions were performed using a 2:1 ratio of sample:precipitant, to a total volume of 3  $\mu$ L and also of 6  $\mu$ L.

#### **2.2.4. Cryogenic protection of the crystals**

In order to avoid radiation damage of the crystals upon exposure to X-ray energies, it was necessary cryocooling the crystals in liquid nitrogen. The crystals were then suspended in a harvesting buffer containing a higher concentration of the same precipitant solution as used for the crystallization, in the same buffer, in order to stop the crystal growth. For HEWL crystals, 8% NaCl was used in the harvesting buffer. With the intent to avoid the formation of ice in the crystals, these are suspended in a cryo buffer, composed of the same solution as the harvesting buffer but adding, in the present case, 30% glycerol. The crystals were then mounted in a loop with appropriate size and flash-cooled in liquid nitrogen.

### **2.3. Structure determination**

#### **2.3.1. X-ray diffraction and data collection**

Preliminary X-ray analysis of HEWL crystals was performed using an in-house copper rotating anode X-ray generator (FR591 Enraf-Nonius) and an imaging plate detector system (MAR-Research), coupled to an Oxford cryo-system.

Data collection of the HEWL crystals grown with AuNP-PVP was carried out using synchrotron radiation at SOLEIL (Proxima I). After a fluorescence scan and identification of gold X-ray absorption edges, a full data set was collected at 0.861  $\text{\AA}$ . Data of HEWL crystals soaked with AuNP-PVP was collected at SLS (Swiss Light Source, Villigen, Switzerland) at beamline X06DA (PXIII) at 1  $\text{\AA}$ , after scanning for gold. HEWL crystals grown with Au(I) data were collected at (Swiss Light Source, Villigen, Switzerland), at beamline X06DA (PXIII) and at 1.038  $\text{\AA}$ , also coincident with the gold X-ray absorption edge.

### **2.3.2. Data processing, structure refinement and gold atoms position determination**

The data collected was processed using iMOSFLM<sup>68</sup> for the HEWL with AuNP-PVP crystals, and XDS (X-ray Detector Software) package<sup>69</sup> for the crystals soaked with AuNP-PVP and the ones grown with Au(I). Data was then scaled and merged using SCALA and reindexed by Pointless and Reindex, from the CCP4 suite<sup>70</sup>.

In order to avoid interference from radiation damage in the structures refinement, data provenient from the crystals grown in the presence of Au(I) were scaled and refined using circa half of the measured images, assuring that completeness was not lost.

HEWL model was built by molecular replacement using 193L structure from PDB using AutoMR and AutoBuild from Phenix suite<sup>71</sup>. For structure refinement, a combination of manual building in Coot<sup>72</sup> was carried out alternated with refinement cycles by phenix.refine from Phenix suite<sup>71</sup>. The anomalous signals that allowed identifying the gold atoms positions within HEWL structures were also calculated using phenix.refine<sup>71</sup>. Molecular graphics and analyses of the protein and gold structures were performed with the UCSF Chimera package<sup>73</sup>.

Since the immediate purpose of this study is the qualitative identification of the positions of the gold atoms, the refinement of the HEWL structures here presented is not yet fully terminated.

### **2.4. TEM analysis**

TEM experiemnts were performed by Dr. Pedro Quaresma at MicroLab - Laboratório de Microscopia Electrónica do Instituto Superior Técnico, Universidade Técnica de Lisboa, cortesy of Dr. Patrícia Carvalho. A sample of 20 µL was deposited over a carbon covered TEM copper grid and then dried at room temperature. TEM images were collected using a microscope HITACHI H-8100, operated with 200 kV of acceleration voltage, and then analysed with ImageJ for the AuNPs count. Origin Pro 8.0 was used to produce the diameters histograms.

The TEM images of HEWL crystals grown with AuNP-PVP and with Au(I) were performed by first washing the crystals in Milli-Q water to eliminate the excess of the crystallization solution and then dissolving them also in Milli-Q. The 2D HEWL crystals with AuNP-PVP were quickly passed through a drop of Milli-Q water and then smashed and deposited over the TEM grid.

### **2.5. AuNP-PVP stability and interactions studies with HEWL**

#### **2.5.1. Spectrophotometric analysis**

UV/Vis spectra were measured with a Unicam UV-Vis Spectrophotometer UV2, using the Scan function and quartz cells of 0,5 mL. Mili-Q water was always used as reference.

### ***Stability study of the AuNP-PVP solution***

Absorption spectra of 3 nM AuNP-PVP solutions were measured with increasing concentrations of NaCl from 0.1 to 1 M, at room temperature. Aqueous solutions were prepared with Milli-Q water. For the pH dependence study, spectra of 3 nM AuNP-PVP in the same buffer solutions as used for the co-crystallization experiments (subsection 2.2.1) at a pH range from pH 4 to pH 10 were also measured. AuNP-PVP solution in Milli-Q was also measured as a control.

### ***Stability study of the AuNP-PVP in solution with HEWL***

Spectra of AuNP-PVP solutions were measured for increasing ratios of AuNP-PVP to HEWL of 1:200, 1:1000 and 1:5000 nM of AuNP-PVP to nM of protein, adjusted to pH 3, 4, 6 and 10, after being incubated overnight at pH 7 which was also measured. AuNP-PVP solution in Milli-Q was also measured as a control.

### ***Stability study of the AuNP-PVP in solution with RNase crystallization condition***

Absorption spectra were measured of AuNP-PVP solution prepared in sodium acetate pH 5.5 and the 3 M NaCl and 1.2 M  $(\text{NH}_4)_2\text{SO}_4$  mixture, in the same volume proportion of 1:1 of sample:precipitate as present in RNase crystallization drops. AuNP-PVP control solution in Milli-Q water was measured as well. The spectra were taken as prepared and after being left overnight. Photographs of the solutions left overnight were taken with a digital camera to show the colour changes that occurred in the samples.

## **2.5.2. Agarose gel electrophoresis**

0.5% agarose gels were prepared by heating agarose in 50 mL Tris-Acetate-EDTA (TAE) buffer pH 8, 1 X, and allowing the gel to form at room temperature. AuNP-PVP solution with HEWL at molar ratios of 1:200, 1:1000 and 1:5000 and AuNP-PVP control sample, in 50 mM sodium acetate buffer pH 4, were pelleted by centrifugation, at 3600 rpm for 10 minutes using Milipore centrifugal filter units. Pellets were then resuspended in 30  $\mu\text{L}$  of the respective buffer and mixed with 3  $\mu\text{L}$  glycerol (10%) prior to loading. 6 wells gels were run at constant voltage of 100 V, with a 15 cm electrode spacing, for 30 minutes, in TAE pH 8, 1 X, using the mini-protean system from BioRad. Photographs of the resultant gel were acquired with a digital camera.

## **2.5.3. Zeta potential analysis**

$\zeta$ -potential measurements were executed with Zetasizer Nano ZS (Malvern Instruments), using appropriate disposable cells (Foldel capillary cells, Zetasizer Nano series, Malvern). Analysis were performed on 3 nM AuNP-PVP solutions prepared in the same buffer solutions as used for the co-crystallization studies (subsection 2.2.1) at a pH range from pH 4 to pH 10, to a final

volume of 1mL. All buffer solutions were filtrated previously to preparing the samples. Mili-Q water was always used for sample preparation, as well as to wash the cells. Three cycles of 100 readings each were performed per sample, at 25 °C, with a temperature stabilization time of 180 seconds. The values presented are an arithmetic average of the three cycles and its respective standard deviation was calculated.





## **CHAPTER 3**

---

# **Results and Discussion**

In this section, a detailed description of the experimental findings is presented divided in distinct projects. The studies are organised in three projects describing the results of the experimental work aimed at studying the incorporation of gold nanoparticles within protein crystals, Project I, the results for the studies on the growth of gold nanoparticles within HEWL crystals, Project II, and the results regarding the study of gold nanoparticles-induced protein crystal growth, Project III.

## **3.1. Project I**

# **Incorporation of gold nanoparticles within protein crystals**



With the intent to study the interactions between AuNPs and proteins and also to pursue the viability of producing protein gold derivatives using AuNPs, Takeda *et al*'s<sup>64</sup> work with HEWL and AuNPs functionalized with PVP was here reproduced, and results were further analysed using X-ray diffraction techniques and TEM experiments. The same approach was tried with RNase as a model protein.

### 3.1.1. Studies with HEWL

#### 3.1.1.1. Co-crystallization experiments

Co-crystallization experiments were initially performed at pH 4 and pH 8, based on Takeda *et al.* studies<sup>64</sup>.

The resulting HEWL crystals at pH 4 were detected and exhibited a deep red colour only in the  $\{1\ 0\ 1\}$  sectors, while the  $\{1\ 1\ 0\}$  sectors remained completely clear, in an analogous way to what was observed by Takeda *et al*'s<sup>64</sup> (Figure 3.1). Since HEWL crystals are colourless, the observed red colour was indicative of the presence of the AuNP-PVP solution within those crystal sectors. It was also perceived that the central region of the  $\{1\ 0\ 1\}$  sector contained a larger amount of the AuNP-PVP than the exterior region of the same sector. This event might indicate that in the initial stages of crystal growth there was a greater assembly of the AuNP-PVP into  $\{1\ 0\ 1\}$  sector and, as the crystals grew, the AuNP-PVP concentration depleted hence resulting in a faded colour towards the extremity of the crystal. On the other hand, at pH 8, the resultant HEWL crystals were only detected after more than a day and, most of the crystals, revealed a deep red colour homogeneously distributed within the whole crystal (Figure 3.1). In a very small number of crystals grown (less than 50% of crystals) it could be observed the dissimilar assembly of the AuNP-PVP into the  $\{1\ 0\ 1\}$  and  $\{1\ 1\ 0\}$  sectors, always more concentrated within the  $\{1\ 0\ 1\}$  sector.

Clear differences were observed in the incorporation of the AuNP-PVP into the crystals grown at pH 4, where the AuNP-PVP were only detected at the  $\{1\ 0\ 1\}$  sectors, and at pH 8, where the AuNP-PVP were observed to be homogeneously distributed within most of the crystals. It was then hypothesized that those differences could be related with different superficial charge of the AuNP-PVP and HEWL's overall surface potential at pH 4 and pH 8, which would promote different electrostatic interactions between the AuNP-PVP and the crystal sectors.

Nonetheless, the assembly of the AuNP-PVP into HEWL crystals did not disrupt its isomorphism, as the resultant crystals presented the tetragonal crystalline structure normally seen for HEWL crystals<sup>49,50</sup>.

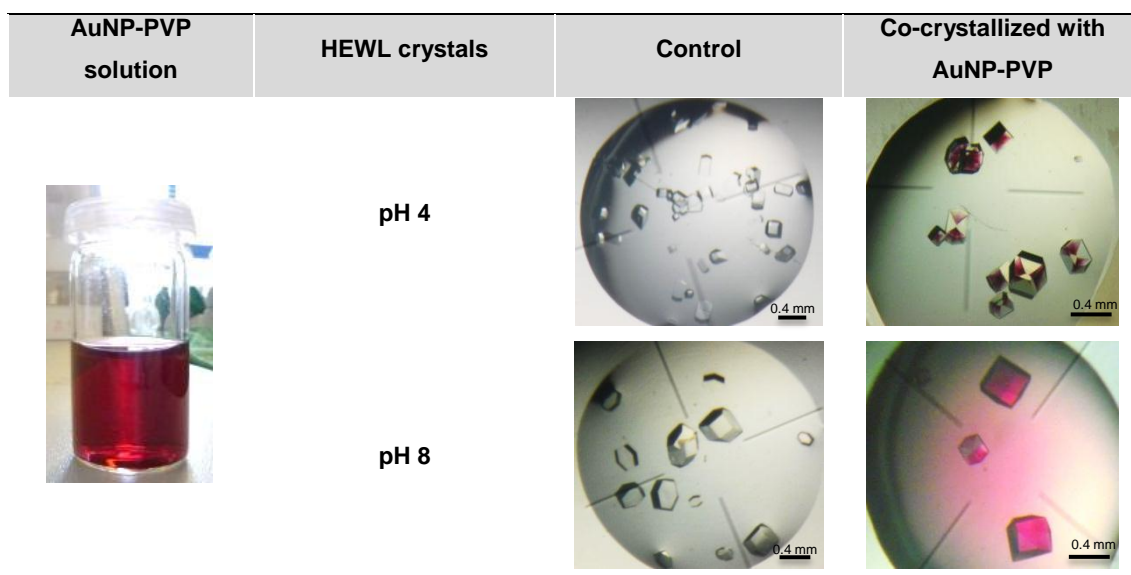


**Figure 3.1.** Microscope images of the HEWL crystals grown in the presence of AuNP-PVP (5x magnification), obtained from 35mg/mL of protein and 34nM of AuNP-PVP and 5% NaCl as precipitant in 50mM sodium acetate pH 4 and 50mM Boric acid pH 8. Images of the respective HEWL control crystals are also presented, as well as a photograph of the AuNP-PVP solution as synthesized, showing its red colour.

In order to explain this observation, a pH dependence study was carried out by making crystallization drops of HEWL with AuNP-PVP at a pH ranging from 4 to 10 (Figure 3.2). However, the resulting crystals did not present the same pattern of the AuNP-PVP assembly as observed before. At pH 4 the AuNP-PVP assembly into the crystals was not only in the  $\{1\ 0\ 1\}$  sectors, but also could be observed, although with a lower intensity, at the  $\{1\ 1\ 0\}$  sector. The same behaviour was observed at pH 5 and pH 6. At pH 7, the AuNP-PVP deposition was mostly detected onto in the  $\{1\ 0\ 1\}$  sectors. At pH 8, like previously observed, and pH 9, it was observed an almost uniform assembly of the AuNP-PVP into the whole crystals with a slightly increased concentration within the  $\{1\ 0\ 1\}$  sectors. Finally at pH 10, the AuNP-PVP were mostly homogeneously distributed throughout the crystals, with a higher concentration of the nanoparticles observed in the centre of the crystal while presenting a more faded colour in the peripheral region.

HEWL crystalline form is greatly dependent on the crystallization condition, and as the drops at the different pH values were almost all made with different buffer solutions (subsection 2.2.1.), the resultant crystals presented dissimilar structures for the diverse pH values (Figure 3.2). Nevertheless, the AuNP-PVP assembly into HEWL crystals did not seem much dependent on the pH value of the medium. In all the pH values tested it was observed that the AuNP-PVP incorporated into the  $\{1\ 0\ 1\}$  sectors as much as homogeneously within the whole crystal, although in less than half of the crystals. So it was not possible to verify the initial observation that the AuNP-PVP incorporated HEWL crystals in different manners at pH 4 and pH 8.

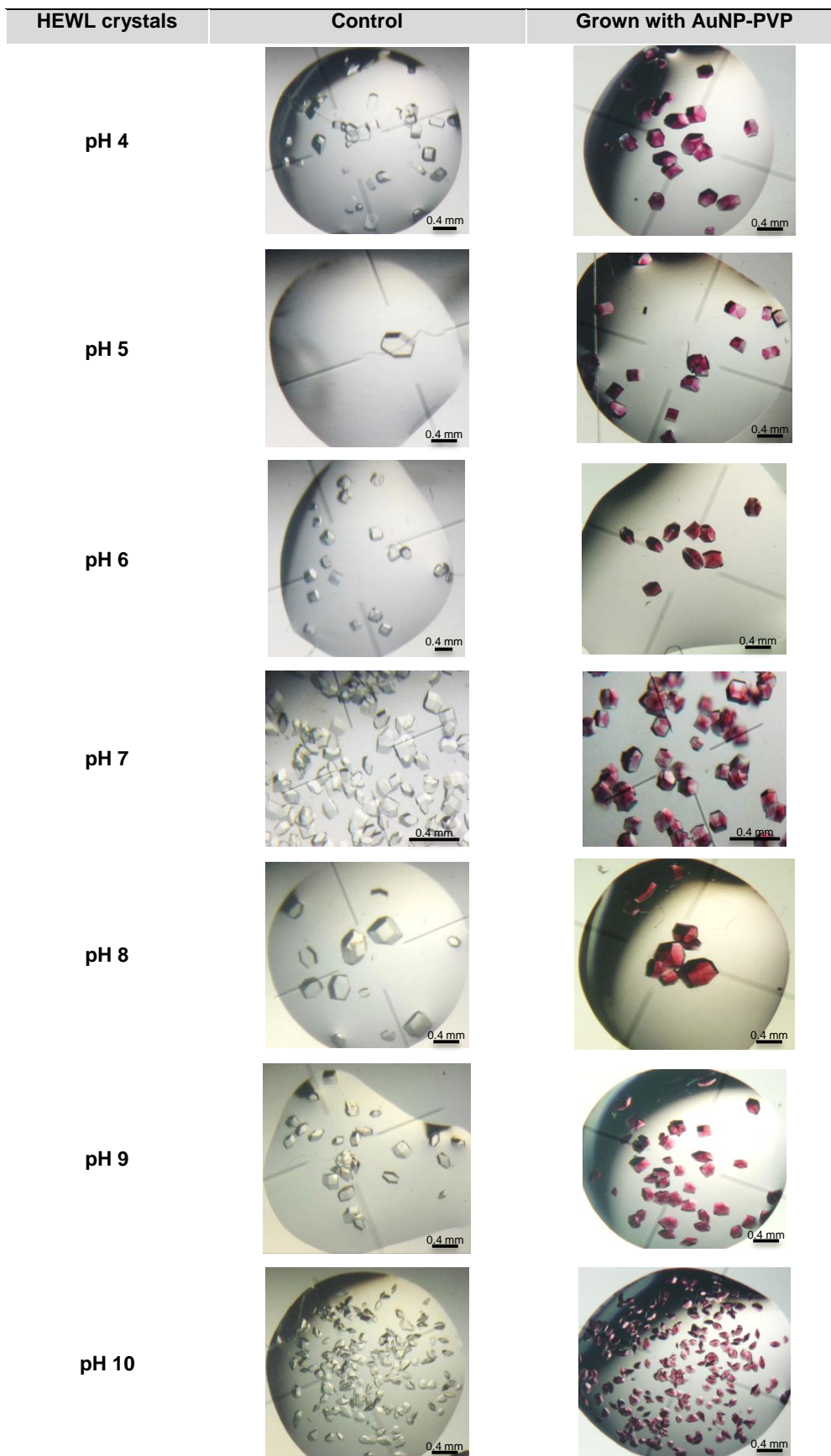


**Figure 3.2.** Microscope images of HEWL co-crystallized with AuNP-PVP (5x magnification and 7x for pH 7), using 35mg/mL of protein and 34nM of AuNP-PVP solution and 5% NaCl as precipitant, at pH ranging from 4 to 10. Images of HEWL control crystals grown in the same conditions but without the addition of AuNP-PVP are also presented.

Additionally, the AuNP-PVP synthesis batch seemed to influence the AuNP assembly within the crystals. Each time a new AuNP-PVP synthesis batch was used to co-crystallize with HEWL, not always was observed the same clear assembly of the AuNP-PVP only into the  $\{1\ 0\ 1\}$  crystal sectors as it was obtained in the first trials at pH 4 (Figure 3.1). In the following co-crystallization experiments, even in the crystals where the incorporation into the  $\{1\ 0\ 1\}$  was distinctive, it was always observed AuNP-PVP in the  $\{1\ 1\ 0\}$  with a lower intensity at all the pH range tested (Figure 3.2). It is possible that each synthesis could produce AuNP-PVP solutions with slightly different characteristics, affecting the sizes distribution and even the stability of the solution, aspects that could influence its assembly into HEWL crystals. An evidence of this event would be the small deviations observed in the SPR band maximum of absorbance of the as synthesized AuNP-PVP solutions which resulted from distinct AuNP-PVP diameters (see Appendix B).

Given those observations, electrostatic interactions depending on the pH of the crystallization medium, could not alone explain the observed dissimilar incorporation of the AuNP-PVP into HEWL crystals, as previously hypothesised.

#### **3.1.1.2. Soaking experiments**

In order to understand if the incorporation of the AuNP-PVP into HEWL crystals would only occur under co-crystallization conditions, soaking experiments were performed in which a AuNP-PVP solution was added to a drop containing HEWL crystals previously grown at pH 4 and pH 8 in the absence of AuNPs (Figure 3.3). After one day, the HEWL crystals presented a red colour resultant from the incorporation of the AuNP-PVP solution. However this incorporation was only observed immediately below the crystal's surface, as if the AuNP-PVP were coating the crystals, as no assembly of the AuNP-PVP into specific crystals' sectors was detected. Additionally, by the time that the incorporation of the AuNP-PVP into the HEWL crystals was observed, several other smaller crystals had grown in the drop at pH 8, that were not initially present. Those crystals had co-crystallized with the AuNP-PVP, and actually presented the nanoparticles assembled into the  $\{1\ 0\ 1\}$  sectors. From these observations it could then be inferred that the co-crystallization process would be essential for the incorporation of the AuNP-PVP within the whole HEWL crystals. The co-crystallization would allow the assembly of the nanoparticles within the crystalline sectors along the crystal growth, and not just its deposition in the crystal surface as observed in the soaking experiments.



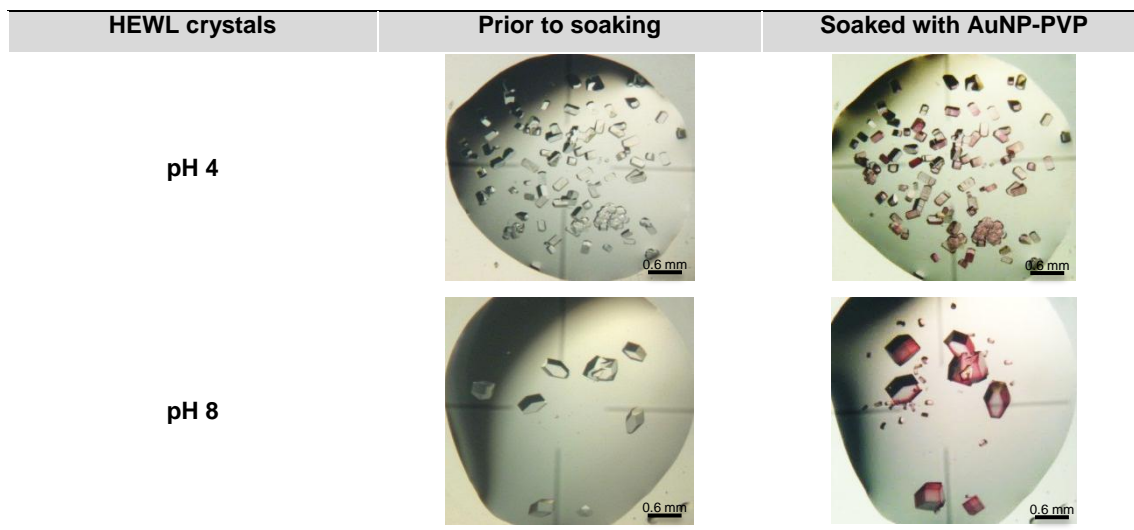


**Figure 3.3.** Microscope images of the HEWL crystals (5x magnification) obtained from 35 mg/ml of protein using 5% NaCl as precipitant, in 50 mM sodium acetate pH 4 and 50 mM boric acid pH 8, prior to soaking and soaked with 34 nM of AuNP-PVP.

### 3.1.1.3. TEM analysis

With the intent of obtaining further evidence that AuNP-PVP incorporated within the HEWL crystals, TEM images were collected from a sample of red HEWL crystals, previously dissolved in Milli-Q water. A sample of the AuNP-PVP solution was measured as well, as a control.

The electron micrographs collected of the AuNP-PVP solution (Figure 3.4.a) revealed a heterogeneous population of spherical gold nanoparticles with an average diameter of  $24.7 \pm 9.5$  nm. Regarding the TEM images obtained for the HEWL crystals grown in the presence of the AuNP-PVP, the presence of spherical gold nanoparticles was also detected (Figure 3.4.b) with an average diameter of  $24.3 \pm 12.4$  nm.

These results came to support the idea that AuNP-PVP were in fact present within the HEWL crystals, in its interior or at its surface, as it was suggested by its deep red colour.

Comparing these results with the control sample (Figure 3.4.a), AuNP-PVP within the HEWL crystals (Figure 3.4.b) presented the same characteristics as AuNP-PVP in solution, with no significant changes on its shape or size.

Although the TEM images showed the presence of AuNPs within the dissolved HEWL crystals, some questions about the localization of the NPs within the crystals remained, since what was analysed was a solution resultant from dissolving the crystals and not the intact crystals. In order to produce TEM micrographs of HEWL crystals incorporated with the AuNP-PVP without its prior dissolution, much thinner crystals were required.

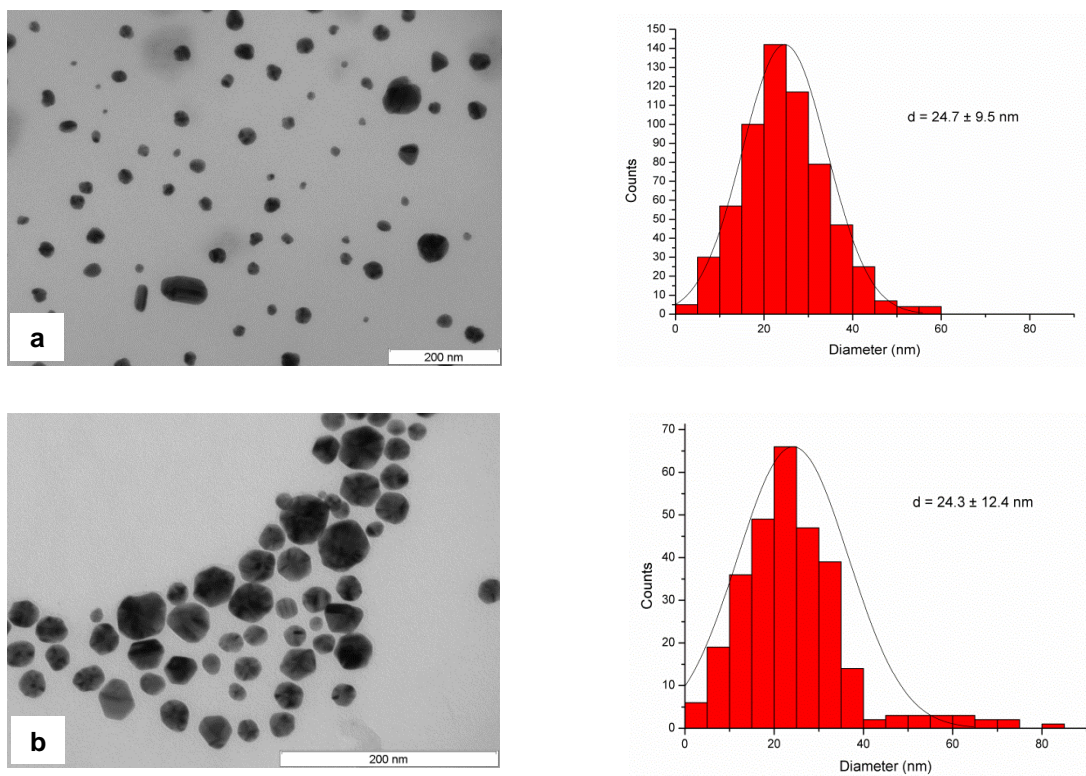


**Figure 3.4.** Electron micrographs of the AuNP-PVP solution **(a)** and of the HEWL crystals grown in the presence of AuNP-PVP, previously dissolved in Milli-Q water **(b)**. The respective sizes distribution histograms are presented on the side.

With that purpose, the production of two-dimensional HEWL crystals that would also incorporate the AuNP-PVP solution was attempted. Those crystals were actually possible to obtain just by spreading the crystallization drop, which allowed the crystals to grow two-dimensionally along the glass slide (Figure 3.5). By co-crystallizing HEWL with the AuNP-PVP using that technique, light-red two-dimensional crystals were obtained at pH 4 and pH 8. Those crystals were then harvested from the crystallization drop and smashed against the TEM grid.

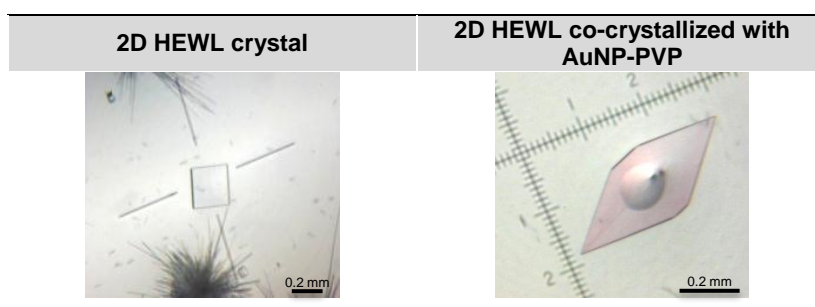


**Figure 3.5.** Microscope images of HEWL 2D crystals (5x magnification) obtained from 35mg/mL of protein in 50mM boric acid pH 8 and 5% NaCl as precipitant, in a spread drop, control and co-crystallized with AuNP-PVP 34nM in the same conditions.

Although it was very difficult to obtain good TEM images from the smashed crystals, due to the presence of high quantities of organic matter, it was possible to detect the existence of spherical AuNPs within the crystals pieces with average diameter of  $28.5 \pm 11.8$  nm from the images taken of the crystals grown at pH 4 and  $22.3 \pm 10.6$  nm from the images taken of the crystals grown at pH 8 (Figure 3.6).

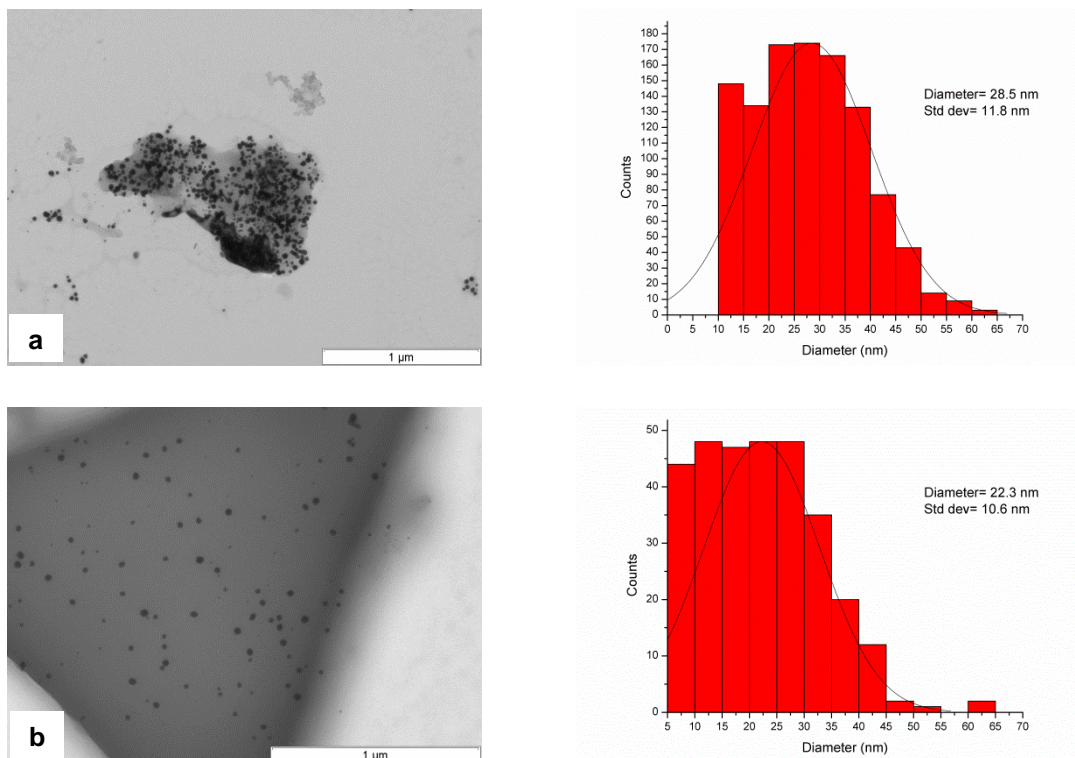


**Figure 3.6.** Electron micrographs of the HEWL-AuNP-PVP 2D crystals at pH 4 (**a**) and at pH 8 (**b**) directly placed upon the TEM grid. The respective sizes distribution histograms are presented at the side.

These two values are well within the error range, and are also related with the previous TEM analyses of the dissolved crystals where  $24.3 \pm 12.4$  nm AuNPs were measured corresponding to the  $24.7 \pm 9.5$  nm of the AuNP-PVP solution itself. So these TEM studies allowed gathering evidence that the AuNP-PVP actually assembled into the HEWL crystals.

#### 3.1.1.4. Zeta-potential analysis

In order to study the PVP-stabilized AuNPs' surface charge dependence on the pH of the medium,  $\zeta$ -potential values were measured for AuNP-PVP solutions in a range from pH 4 to pH 10. The samples were prepared in the same buffer solutions as used in the crystallization studies previously discussed (subsection 3.1.1.1.).

Since the AuNPs functionalization ligand, PVP, is neutral, not possessing any charge or protonable groups, the  $\zeta$ -potential value would only be dependent on the  $H^+$  and  $OH^-$  ions in

solution at each pH value. The AuNP-PVP  $\zeta$ -potential was negative in the entire pH range and decreased with increasing pH, from  $-4.50 \pm 0.65$  mV to  $-21.37 \pm 2.12$  mV (Figure 3.7) (See Appendix A. Table A.1 for the  $\zeta$ -potential values and respective standard deviations). However, as previously discussed,  $\zeta$ -potential measurements only provide a rough estimate of the overall net charge present at the AuNP-PVP surface generated by the ions present in solution at each pH value, and not the AuNPs effective charge.

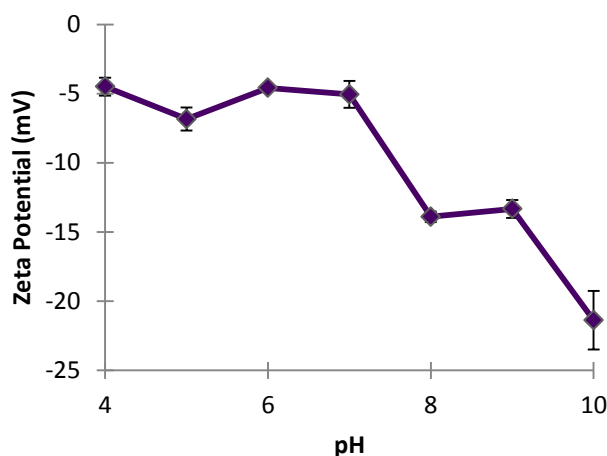


**Figure 3.7.**  $\zeta$ -potential measurements of the AuNP-PVP solution at a pH range from pH 4 to pH 10.

HEWL in solution is positive at pH below its isoelectric point ( $pI = 11.35^{74}$ ) and since  $\zeta$ -potential of the AuNP-PVP solution was always negative, electrostatic interactions would be expected between HEWL and the PVP-stabilized AuNPs at the assayed pH values (4 and 8), which could explain its assembly into HEWL crystals. Nevertheless, and as seen before (subsection 3.1.1.1.), there is no evidence of a direct correlation between the AuNPs surface charge, and hence the pH of the medium, and its assembly into HEWL crystals.

### 3.1.1.5. Spectroscopic studies

#### ***Stability study of the AuNP-PVP solution***

UV-visible experiments were carried out with the purpose to monitor the stability of the PVP-stabilized AuNPs' solution, in terms of the medium ionic strength and pH.

The typical spectrum of the AuNP-PVP solution as synthesized presented an SPR band with a maximum absorbance at around 533 nm (Figure 3.8, red spectrum in the left graphic). From the spectra obtained for the AuNP-PVP solution with increasing concentrations of NaCl, any red-shifts of the SPR band or decrease of its intensity were observed, as all the spectra overlaid with the AuNP-PVP control spectrum (Figure 3.8, left panel). From the spectra taken at a range of pH 4 to pH 10, the same results were obtained (Figure 3.8, right panel). No red-shift of the

plasmon band was detected and the small depletion in intensity of the spectra that seemed to have occurred was merely due to changes in the baseline, and not due to AuNP-PVP precipitation.

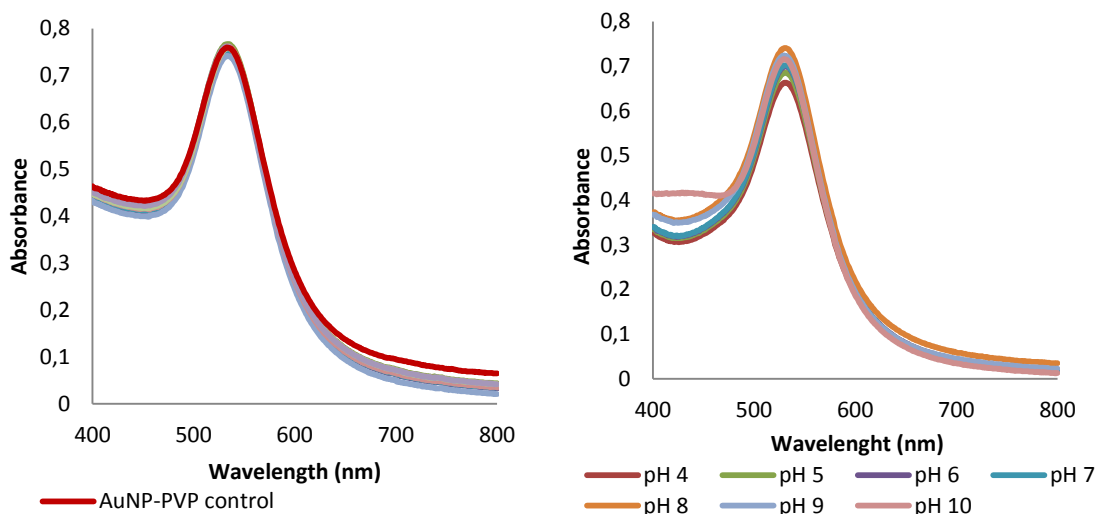


**Figure 3.8.** Left panel: Absorption spectra of AuNP-PVP solutions measured as function of NaCl's ionic strength of 0.1 to 1 M are presented in the left. The absorption spectrum of a control sample of AuNP-PVP is depicted in red; the remaining spectra correspond to increasing concentrations of NaCl which all superimpose with the control spectrum. Right panel: Absorption spectra of AuNP-PVP as a function of the solution's pH.

This behaviour of the AuNP-PVP solution was expectable, showing that the PVP was in fact serving its function as a stabilizer and protecting the AuNPs. Since a relatively large PVP molecule was used for the stabilization of the AuNPs (PVP K30), and being the PVP a non-charged compound, it would be expected that the polymer would form a coiled and dense corona around the AuNPs, hence protecting its core from the surrounding medium. Also, PVP did not possess any protonable groups, not being likely a pH dependence of the AuNP-PVP. Thus, it could be inferred that the AuNP-PVP resultant from this synthesis method were extremely stable in solution.

#### **Stability study of the AuNP-PVP in solution with HEWL**

Previous work showed<sup>65</sup> that differently functionalized AuNPs aggregated and completely precipitated in solution with HEWL, at the same protein to AuNPs ratio as in the crystallization drops. It was then important to study if HEWL would have the same effect on the AuNP-PVP or even if bionanoconjugates would be stable in solution, in the present project. With that intent, spectra of the AuNP-PVP were measured for increasing ratios of AuNP-PVP to HEWL adjusted to four pH values, after being incubated overnight at pH 7. However, the spectra of the resulting solutions (Figure 3.9) did not present any signs that HEWL would have affected the AuNP-PVP. For the three AuNP-PVP to HEWL ratios tested (1:200, 1:1000 and 1:5000 nM of AuNP-PVP to

nM of protein), no red-shift of the plasmon band was detected regarding the control spectrum, indicating no signs of aggregation or precipitation of the AuNPs. The weakening in intensity of the spectra that seemed to have occurred would merely due to changes in the baseline and to some dilution of the solution upon adjustment of the pH, and not due to AuNP-PVP precipitation.

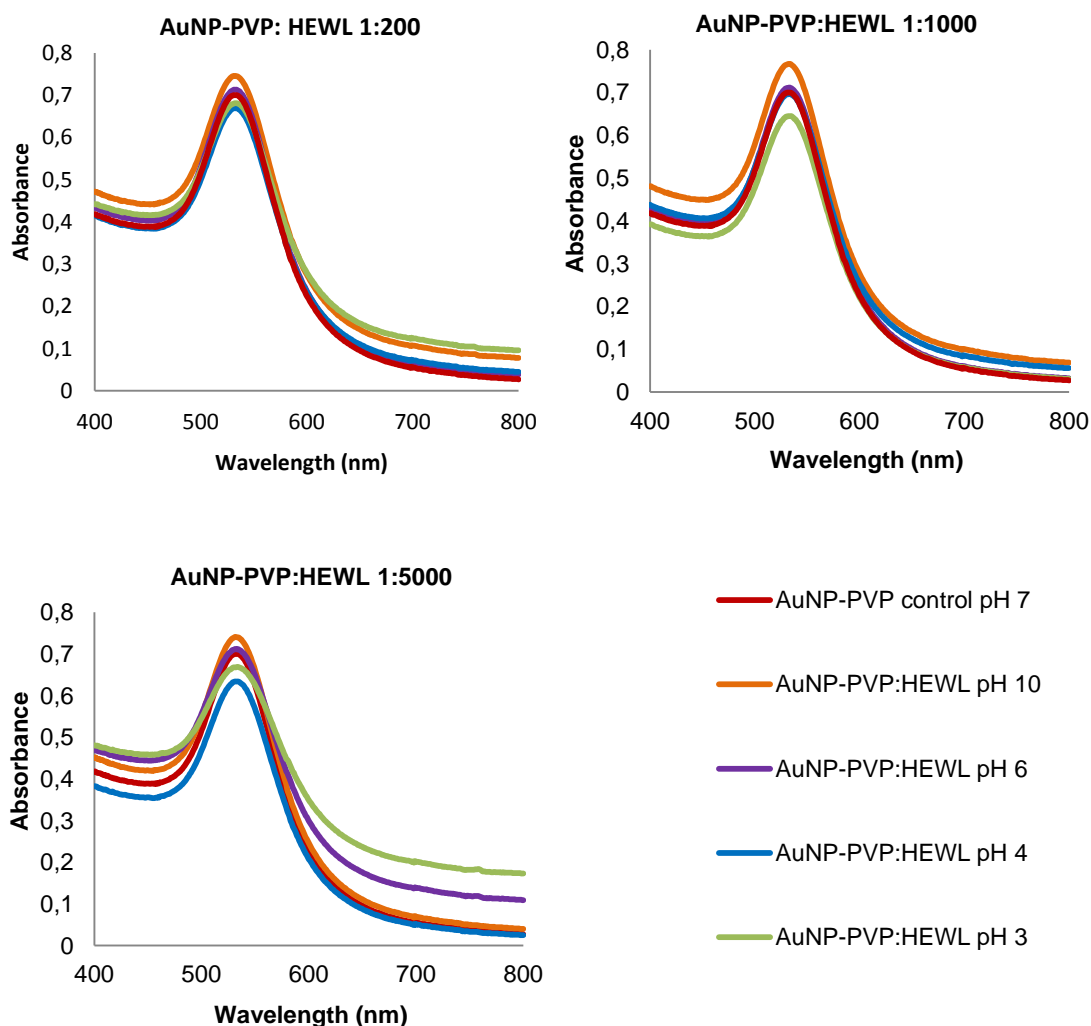


**Figure 3.9.** Absorption spectra of AuNP-PVP and HEWL solutions at 1:200, 1:1000 and 1:5000 ratios, measured at pH 3 (in green), pH 4 (in blue), pH 6 (in purple) and pH 10 (in orange). A control spectrum of an AuNP-PVP solution at pH 7 (in red) was also measured.

No evidences of bionanoconjugation were observed as well. Since, the AuNP-PVP did not aggregated at any pH value, as seen above (subsection 3.1.1.5.), if conjugation with HEWL had occurred it would be expected to see some shift of the SPR band towards higher wavelengths, which was not detected. This high stability of the AuNP-PVP in solution with HEWL would be, once again, due to the AuNPs layer of protection conferred by the PVP polymer that did not allow the protein to directly interact with the AuNPs core and promote its aggregation, as seen before with other different functionalized AuNPs<sup>65</sup>. Giving that, the AuNP-PVP solution would be



able to enter HEWL's crystals through its solvent channels and incorporate into its sectors, while retaining its initial optical properties.

### 3.1.1.6. Agarose gel electrophoresis studies

To gather further evidences that would corroborate that any interaction occurred between the AuNP-PVP and HEWL, as it was observed from the spectroscopic studies (previous subsection), agarose gel electrophoresis of the AuNP-PVP in solution with HEWL at pH 4 testing the same ratios as before was performed. As AuNP-PVP are almost neutral at pH 4 (see Appendix A, table A.1), it would be predictable not to see any migration of the AuNP-PVP control sample in the gel. However, if conjugation occurred, it would be expected to see some migration of the AuNP-PVP samples with HEWL towards the negative pole. Since HEWL possesses an overall positive surface potential, it would confer a more positive charge to the conjugate regarding the AuNP-PVP solution alone. Nevertheless, no migration at all was observed, as all the samples stayed within the well (Figure 3.10), which indicated that no conjugation of HEWL with AuNP-PVP occurred. These results came as intended to support what it was previously observed from the spectroscopic studies.

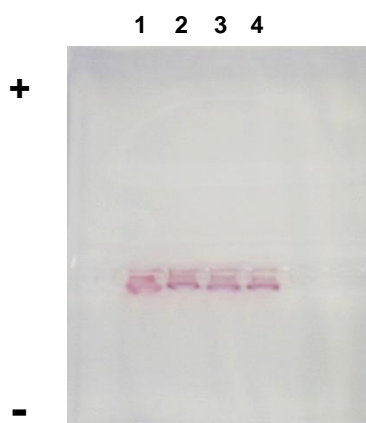


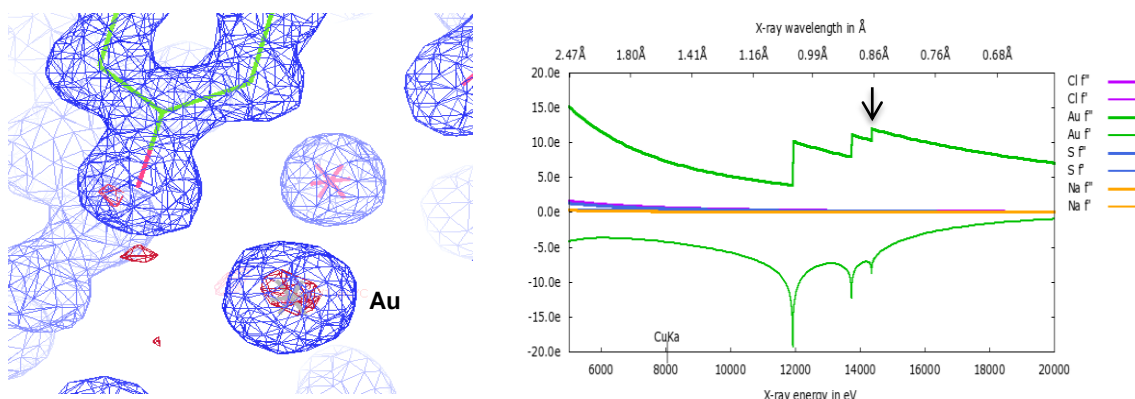
**Figure 3.10.** Agarose gel of AuNP-PVP in solution with different ratios of HEWL, run at 100V for 30 minutes. AuNP-PVP and HEWL samples were prepared in 50mM sodium acetate pH 4: **(1)** AuNP-PVP control; **(2)** AuNP-PVP-HEWL 1:200; **(3)** AuNP-PVP-HEWL 1:500; **(4)** AuNP-PVP-HEWL 1:1000.

If any interaction existed between the protein and the AuNP-PVP it would be too weak to promote the protein's conjugation, which was the expected using PVP as a capping agent. Since the polymer is barely reactive, eventually only maintained weak hydrophobic and Van der Waals interactions with HEWL and even with the gold core as well.

### 3.1.1.7. Structural analysis by X-ray crystallography

#### *Of crystals obtained by co-crystallization experiments with AuNP-PVP*

From the co-crystallization experiments of HEWL with the AuNP-PVP at pH 4 and pH 8, it was possible to obtain well diffracting crystals. Those crystals were then measured by X-ray diffraction techniques at the chosen wavelength of 0.861 Å the  $L_1$  X-ray absorption edge of gold, in order to take advantage of the gold's scattering properties. It was then possible to identify atomic gold at the surface of HEWL structures. By calculating an electron density map using the anomalous differences of the intensities, it was possible to unambiguously identify the positions of the gold atoms (Figure 3.11).

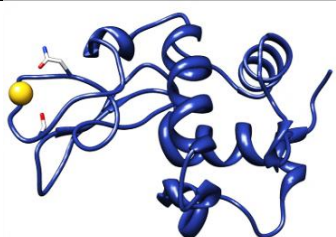
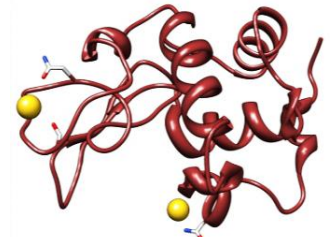
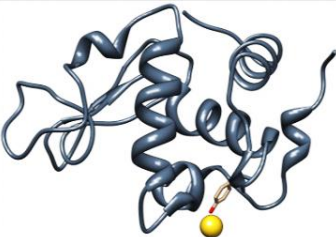


**Figure 3.11.** Electron density map obtained from one of the HEWL-AuNP-PVP crystals measured, showing the anomalous signal (pink density) that allowed identifying the position of the gold atoms. In the left it is presented the diagram used to predict the anomalous scattering factors predicted for gold atoms used to calculate the anomalous differences of the intensities at 0.861 Å.

From the ten crystals measured using synchrotron radiation, seven datasets were collected with good quality data, and from those three HEWL structures were refined holding gold atoms at its surface (Figure 3.12.A, B and C) (see Appendix C, Table C.1 for the respective refinement statistics), refined to a resolution range of 1.05 to 1.50 Å. Although the gold atoms were only identified with partial occupancy, its presence was clear, due to the high anomalous signal centred within its electron density.

Although there were no evidences that the gold atoms were bound to any HEWLs' aminoacid chain, residues already reported to be present in HEWL metal binding sites were observed to be in the vicinity of the gold atoms. This was the case of Asn65 and Ser72<sup>55,56</sup>, at distances of 3.78 Å and 3.471 Å respectively, in the vicinity of the gold atom identified in structure **A** and also in structure **B**. Also in structure **B**, the second metal atom was observed in the vicinity of Asn113 at a distance of 3.450 Å. The structure determined at pH 8, structure **C**, exhibited a single gold atom in the vicinity of Tyr23 residue, at a distance of 2.93 Å (see Appendix F, Figure F.1). This locations were also observed as binding site for gold by Wei and co-workers<sup>56</sup>.



<b>A</b>		Au atoms	1	
		Occupancy	0.21	
		B-factor	35.38	
<b>B</b>		Au atoms	1	2
		Occupancy	0.30	0.35
		B-factor	24.85	21.80
<b>C</b>		Au atoms	1	
		Occupancy	0.32	
		B-factor	16.01	

**Figure 3.12.** HEWL three-dimensional structures solved from crystals grown in the presence of AuNP-PVP using: **(A)** 25 mg/mL of protein in 50mM of sodium acetate pH 4 and 5% NaCl; **(B)** 50 mg/mL of protein in the same buffer and 4% NaCl; and **(C)** 35 mg/mL of protein in 50mM of Boric Acid pH 8 and 5% NaCl. HEWL structures are presented in ribbon representation and gold atoms are shown in yellow as spheres.

By superimposing the structures obtained in the co-crystallization conditions at pH 4 and pH 8 (Figure 3.13), it was observed that the site identified for the gold atom in structure **A** was the exact same position as one of the gold atoms in structure **B** (Figure 3.12), represented half in red and half in blue in Figure 3.13, in the vicinity of Asn65 and Ser72 as referred above.

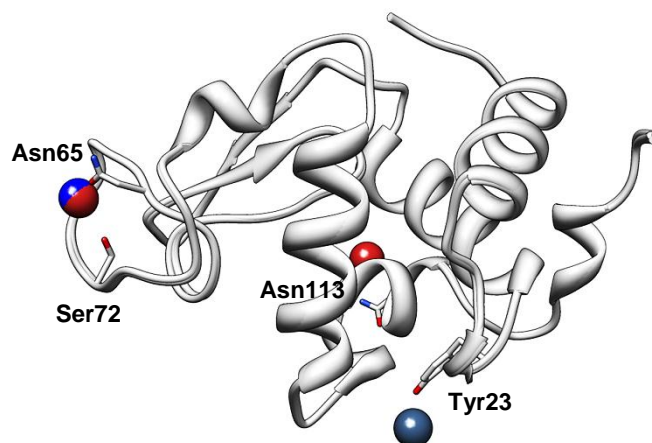


**Figure 3.13.** Superimposition of HEWL structures determined from the crystals grown in the presence of AuNP-PVP at pH 4 and pH 8 (Figure 3.12). HEWL structure is shown in ribbon representation and gold atoms are represented as spheres. The gold atoms are presented in blue for structure **A**, in red for structure **B** and in dark grey for structure **C**.

However, due to the lack of coordination ligands from the protein to the gold atoms, it was not possible to attribute a valence state for the metal atoms determined within HEWL structures.

Analysis of HEWLs' crystal lattice was then carried out with the intent to overview how the atomic gold observed in the protein structures was distributed throughout the crystals (Figure 3.14).

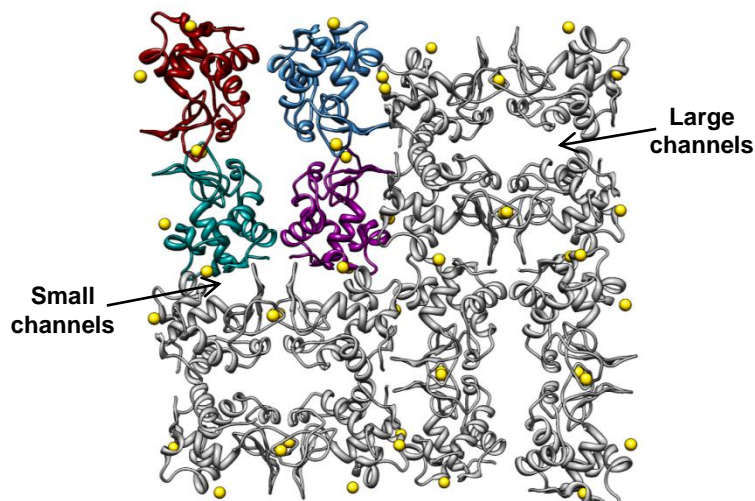


**Figure 3.14.** Crystal lattice of HEWL tetragonal crystals grown in the presence of AuNP-PVP, evidencing the distribution of the gold atoms inside the crystals, produced using Chimera. HEWL structures are drawn in ribbon representation, and four of its monomers are shown in distinctive colours. Gold atoms are represented as spheres depicted in yellow. HEWL crystals' small and large solvent channels are pointed. Image produced using Chimera.

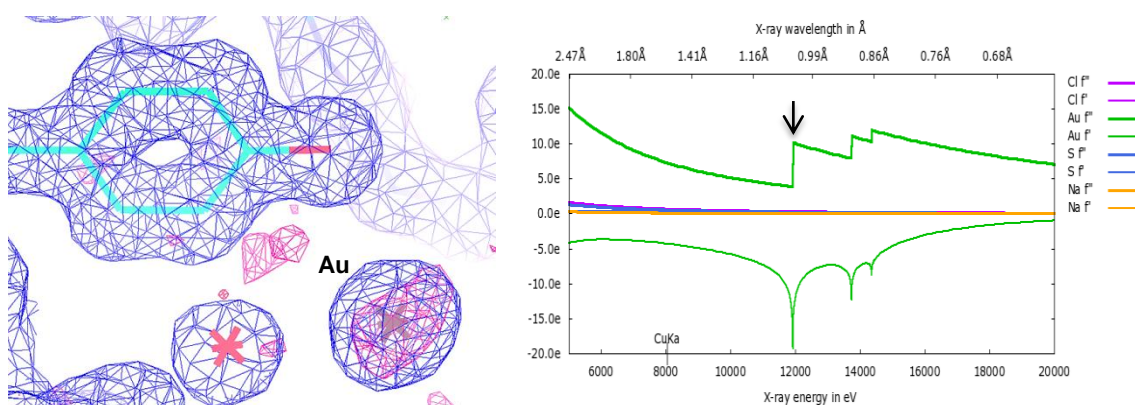
By analysing the crystal lattice of HEWLs' crystals grown in the presence of AuNP-PVP (Figure 3.14), the gold atoms were found in the contact areas between the assembled protein molecules. It was initially thought that the metal atoms would be found in the vicinity of the crystals' solvent channels, since it was hypothesized that the AuNP-PVP solution had incorporated HEWL crystals through these channels. However, it was only determined gold positions within the small solvent channels, and not the large ones. It was also possible that, although the metal atoms would be present within the all solvent channels, the high disorder molecules experience in these channels would not make it possible for the atoms to be present in all the asymmetric units in order for its position to be determined by X-ray diffraction. Nevertheless, the determined gold atoms positions were consistent in the three structures, as all the metal atoms were observed at HEWL's surface between assembled protein molecules, near the small solvent channels. It could then be believed that these sites at the proteins' surface could confer, in a certain manner, a more chemically stable environment for the deposition of atomic gold, making it possible to be determined in the proteins' structures.

It is important to notice that it was atomic gold that was found in the crystallographic structures of HEWL, and not gold nanoparticles. However, considering the isomorphous character of these complex structures when compared to the native structure of HEWL, this method could be a

most relevant option if applied to other protein crystals as a method to produce metal derivatives with the advantage of introducing an anomalous scatterer, which would provide an initial phase estimate in SIRAS methods (Single Isomorphous Replacement with Anomalous Scattering).

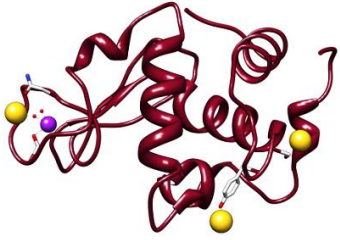
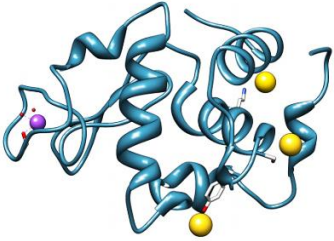
### ***Of crystals obtained by soaking experiments with AuNP-PVP***

From the soaking experiments of HEWL with the AuNP-PVP at pH 4 and pH 8, it was possible to obtain well diffracting crystals. Those crystals were then measured by X-ray diffraction techniques at the chosen wavelength of 1.038 Å the L<sub>III</sub> X-ray absorption edge of gold, in order to take advantage of the gold's scattering properties. It was then possible to identify atomic gold at the surface of HEWL structures. By calculating an electron density map using the anomalous differences of the intensities, it was possible to unambiguously identify the positions of the gold atoms (Figure 3.15).



**Figure 3.15.** Electron density map obtained measured from one of the HEWL crystals soaked with AuNP-PVP, showing the anomalous signal (pink density) that allowed identifying the position of the gold atoms. In the left it is presented the diagram used to predict the anomalous scattering factors predicted for gold atoms used to calculate the anomalous differences of the intensities at 1.038 Å.

From the crystals measured using synchrotron radiation, datasets were collected with good quality data, and from those two HEWL structures were refined holding gold atoms at its surface (Figure 3.16) (see Appendix C, Table C.2 for the respective refinement statistics), refined to a resolution range of 1.38 to 1.45 Å. Although the gold atoms were only identified with partial occupancy, its presence was clear, due to the high anomalous signal centred within its electron density.

pH 4		Au atoms	1	2	3
		Occupancy	0.28	0.25	0.3
		B-factor	21.82	24.43	21.26
pH 8		Au atoms	1	2	3
		Occupancy	0.26	0.31	0.22
		B-factor	22.31	21.44	24.83

**Figure 3.16.** HEWL three-dimensional structures solved from crystals soaked with AuNP-PVP using: 35 mg/mL of protein in 50mM of sodium acetate pH 4 and 5% NaCl and in 50mM of Boric Acid pH 8, using 5% NaCl and then soaked with 34 nM of AuNP-PVP. HEWL structures are presented in ribbon representation and gold atoms are shown in yellow as spheres.

Although there were no evidences that the gold atoms were bound to any HEWLs' residues, by superimposing those structures, two coincident sites were observed (Figure 3.17). Two of the gold atoms present in the structure determined at pH 4 were positioned in the exact same location in the structure obtained at pH 8, in the vicinity of Ser24, at a distance of 3.032 Å, and in the vicinity of Tyr23 residue, at a distance of 2.93 Å (represented half in red and half in blue). Additionally, and like it was also seen in the structures determined by co-crystallization (Figure 3.13), in the structure at pH 4 a gold atom was present in the vicinity of Asn65 and Ser72, at distances of 3.78 Å and 3.471 Å respectively, which was not present in the structure at pH 8. Also in the structure at pH 8, it was determined a second position for a gold atom in the vicinity of Lys33, at a distance of 3.520 Å (see Appendix F, Figure F.1).

However, due to the lack of coordination ligands from the protein to the gold atoms, it was not possible to attribute a valence state for the metal atoms determined within these HEWL structures as well.

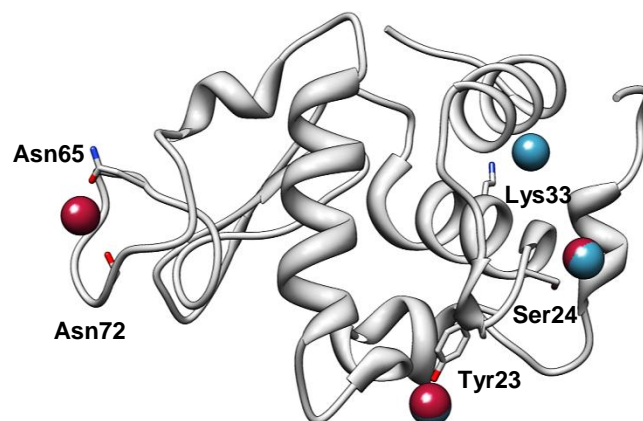


**Figure 3.17.** Superimposition of HEWL three-dimensional structures solved from crystals soaked with AuNP-PVP at pH 4 and pH 8 (Figure 3.16). HEWL structure is shown in ribbon representation and gold atoms are represented as spheres, in blue for the structure at pH 4 and in red for the structure at pH 8.

Analysis of HEWLs' crystal lattice was then carried out with the intent to overview how the atomic gold observed in the protein structures was distributed throughout the crystals (Figure 3.18).

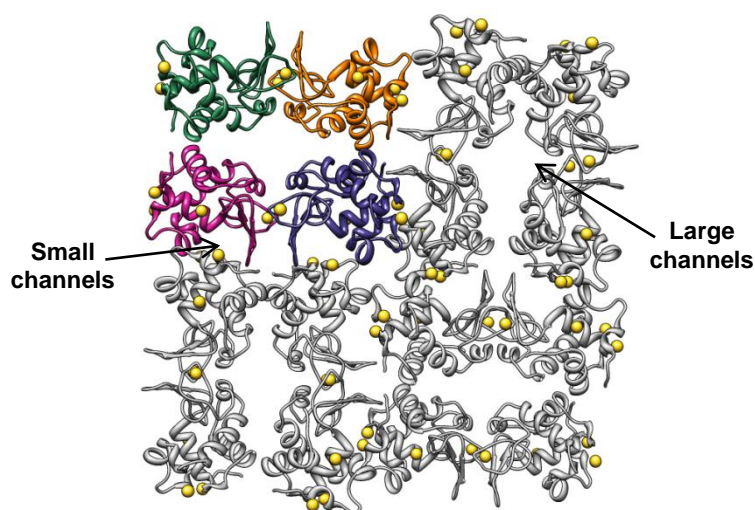


**Figure 3.18.** Crystal lattice of HEWL tetragonal crystals soaked with AuNP-PVP, evidencing the distribution of the gold atoms inside the crystals, produced using Chimera. HEWL structures are drawn in ribbon representation, and four of its monomers are shown in distinctive colours. Gold atoms are represented as spheres depicted in yellow. HEWL crystals' small and large solvent channels are pointed. Image produced using Chimera.

By analysing the crystal lattice of HEWLs' crystals soaked with AuNP-PVP (Figure 3.18), the gold atoms were found in the contact areas between the assembled protein molecules. This observation was coincident with what it was previously seen for the crystals obtained from co-crystallization with AuNP-PVP (Figure 3.14), where the metal atoms were also observed at HEWL's surface between assembled protein monomers, near the small solvent channels.



Once again, it is important to notice that it was atomic gold that was found in the crystallographic structures of HEWL, and not AuNPs. However, considering the isomorphous character of these complex structures when compared to the native structure of HEWL, this method could also be a relevant option if applied to other protein crystals as a method to produce metal derivatives with the advantage of introducing an anomalous scatterer, providing an initial phase estimate in SIRAS methods (Single Isomorphous Replacement with Anomalous Scattering).

### 3.1.2. Studies with RNase

#### 3.1.2.1. Co-crystallization experiments

With the intent to study if the incorporation of AuNP-PVP observed in HEWL crystals (subsection 3.1.1.1.) would also occur with RNase crystals, co-crystallization experiments of RNase with AuNP-PVP were carried out.

Although several crystallization conditions are described for RNase<sup>75-77</sup>, several had to be tested until good crystals were obtained. Such conditions first tried were using 10 mg/ml and 20 mg/ml of protein and as precipitant 3 M NaCl and 0.2 M (NH<sub>4</sub>)<sub>2</sub>SO<sub>4</sub>, or 3 M NaCl and 2 M (NH<sub>4</sub>)<sub>2</sub>SO<sub>4</sub>, in 50 mM sodium acetate pH = 4.5, but no crystals were obtained. A gradient of precipitant concentration was then tried, by increasing the (NH<sub>4</sub>)<sub>2</sub>SO<sub>4</sub> concentration from 0.2 M to 2 M over a period of days, but still no crystals appeared. By trying then to increase the concentration of NaCl in the reservoir until 4 M over a period of days, in drops initially made using 3 M NaCl and 0.2 M (NH<sub>4</sub>)<sub>2</sub>SO<sub>4</sub>, only crystalline plaques resulted. A screening was then tried using 20 mg/ml to 50 mg/ml of protein with 3 M NaCl and 1.2 M (NH<sub>4</sub>)<sub>2</sub>SO<sub>4</sub> as precipitant, in sodium acetate pH 5.5 and pH 6. Suitable crystals were finally obtained after three days only at 50 mg/ml of RNase in sodium acetate pH 5.5 (Figure 3.19).

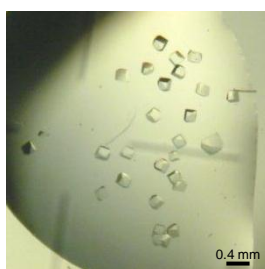


**Figure 3.19.** Microscope images of RNase crystals (5x magnification) obtained from 50mg/ml of protein in 50mM sodium acetate pH 5.5 using 3 M NaCl and 1.2 M of (NH<sub>4</sub>)<sub>2</sub>SO<sub>4</sub> as precipitant.

RNase co-crystallization experiments with AuNP-PVP were then carried out using those conditions, however, some unexpected results were obtained. Instead of incorporating the RNase crystals, the AuNP-PVP had completely precipitated filling the drop with phase

separation bubbles with a purple shade (Figure 3.20). The RNase crystals formed, although smaller and in larger number than the control ones, presented its usual crystalline form (Figure 3.20).

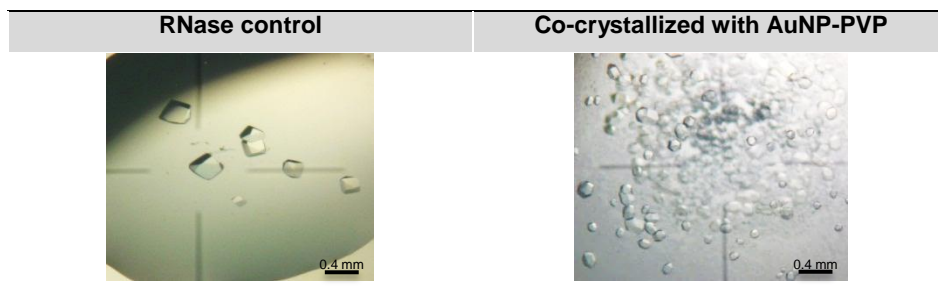


**Figure 3.20.** Microscope images of RNase control crystals (5x magnification) obtained from 50mg/ml of protein in 50mM sodium acetate pH 5.5 using 3 M NaCl and 1.2 M of  $(\text{NH}_4)_2\text{SO}_4$  as precipitant and RNase co-crystallized with AuNP-PVP 34 nM in the same conditions (7x magnification).

We were yet to understand why such stable AuNPs as the AuNP-PVP solution had completely precipitated upon co-crystallization with RNase, and not remained in solution as seen with HEWL. Further experiments were carried on in order to study this event, and results are presented ahead.

### 3.1.2.2. Soaking experiments

In order to try to understand what could be affecting the AuNP-PVP solution, RNase soaking experiments with AuNP-PVP were made. However, exactly the same results were obtained, as previously seen in the co-crystallization drops (see subsection 3.1.2.1., Figure 3.20), as the AuNPs completely precipitated and formed phase separation bubbles. Another approach was then tried, by adding the AuNP-PVP solution to the drops with the RNase plaques initially obtained by increasing the precipitant concentration in the reservoir to 4 M NaCl. Surprisingly, one day after, the RNase plaques exhibited a purple colour, which would be due to the incorporation of the AuNP-PVP solution (Figure 3.21).

Taken these observations, and since the drops where the RNase plaques were formed were initially prepared with 3 M NaCl and 0.2 M  $(\text{NH}_4)_2\text{SO}_4$  and in the following crystallization studies the drops were prepared with 3 M NaCl and 1.2 M  $(\text{NH}_4)_2\text{SO}_4$ , the disruption of the AuNP-PVP stability previously observed could have been caused by the elevated  $(\text{NH}_4)_2\text{SO}_4$  concentration. In order to confirm this theory, spectroscopic studies were carried out and are presented ahead.

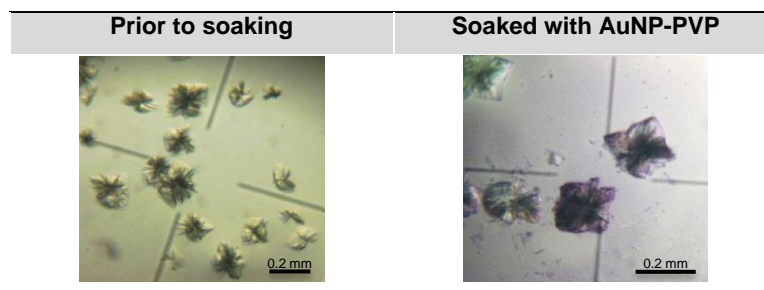


**Figure 3.21.** Microscope images of RNase crystals (7x magnification) obtained from 20 mg/ml of protein in 50 mM sodium acetate pH 4.5 using 3 M NaCl and 0.2 M  $(\text{NH}_4)_2\text{SO}_4$  as precipitant gradually increased to 4 M NaCl, prior to soaking and soaked with AuNP-PVP 34 nM.

### 3.1.2.3. Spectroscopic studies

With the intent to understand what caused to the AuNP-PVP to precipitate in the crystallization drops prepared with 3 M NaCl and 1.2 M  $(\text{NH}_4)_2\text{SO}_4$ , spectra of the AuNP-PVP with the precipitant solution were measured.

By analysing the resulting spectra (Figure 3.22) it could be observed that, while the spectrum of the AuNP-PVP control solution left overnight had barely lowered in intensity regarding the spectrum of the solution as prepared, the spectrum of AuNP-PVP with the RNase precipitant presented a great decrease in intensity in respect to the initial spectrum. This substantial decrease in the spectrum intensity would be due to the precipitation of the AuNP-PVP solution, which could also be observed by the purple colour exhibited by the solution, divergent to the control red colour.

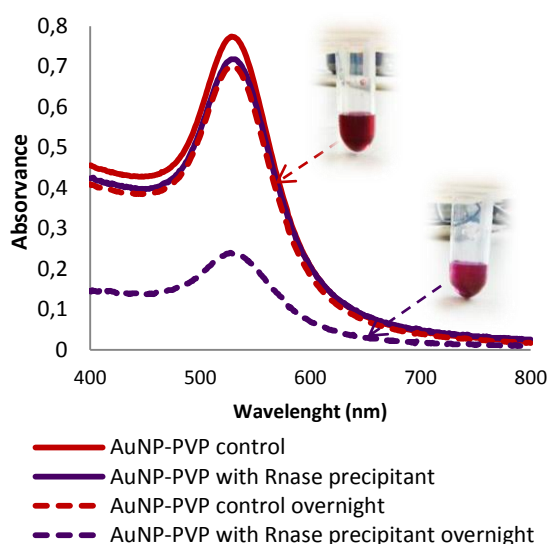


**Figure 3.22.** In purple are presented the absorption spectra of AuNP-PVP solution prepared in sodium acetate pH 5.5 and the mixture of NaCl and  $(\text{NH}_4)_2\text{SO}_4$ , in the same proportion of 1:1 as present in RNase crystallization drops prepared with 3 M NaCl and 1.2 M  $(\text{NH}_4)_2\text{SO}_4$ . The red spectra represent the AuNP-PVP control solution in Milli-Q water. The spectra were measured as prepared (full line) and after being left overnight (dashed line). Photographs of the solutions left overnight are presented showing the red colour for the AuNP-PVP control and the purple colouration for AuNP-PVP with RNase precipitant solution.



Once it was proved that RNase's crystallization condition was responsible for the disruption of the AuNP-PVP solution, and this condition was the only so far where suitable crystals could be obtained, the study with RNase and AuNP-PVP solution was no longer continued.



## **3.2. Project II**

# **Growth of gold nanoparticles within protein crystals**



With the intent to study the formation of AuNPs within HEWL's crystals and its interactions with the protein, Wei *et al.*<sup>56</sup> studies was here reproduced, and results were further analysed using X-ray diffraction techniques and TEM experiments.

### 3.2.1. Co-crystallization experiments

The co-crystallization studies of HEWL with Au(I) here presented were based on Wei *et al.*<sup>56</sup> procedure.

The resulting HEWL crystals could be observed a few days after drop setup, presenting its usual colourless aspect. The crystals started then to change from colourless to pink, first detected around 20 days of growth, and finally to dark red after 40 days, from where no more evolution of the colour was observed (Figure 3.23). This colour evolution would be resultant from the formation of nanostructured gold inside HEWL crystals, where its characteristic SPR band gave rise to the observed colour, which became more intense as the AuNPs were forming larger particles.

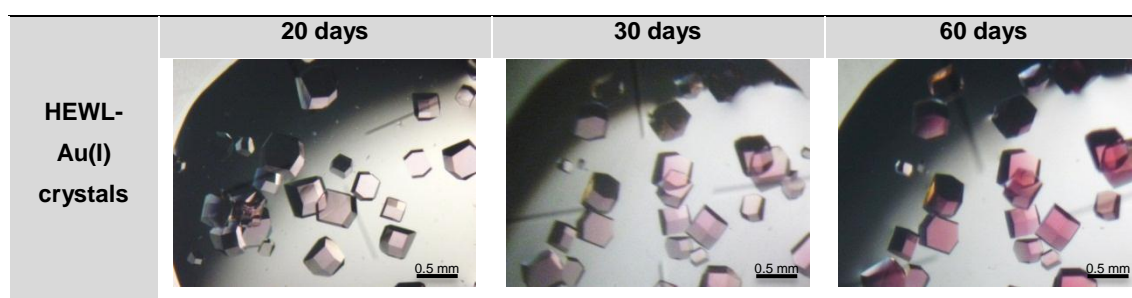
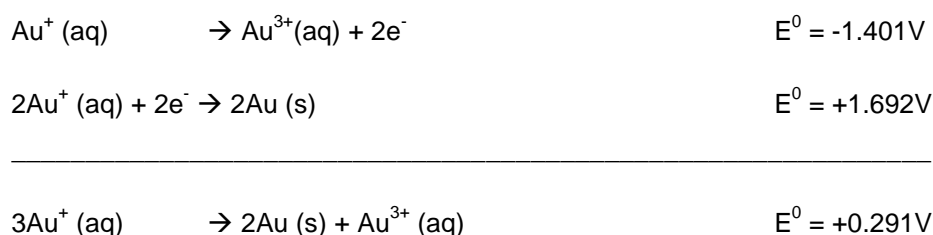


**Figure 3.23.** Microscope photographs of the HEWL crystals (7x magnification) grown in the presence of Au(I) obtained from 75mg/mL of protein and 35mM of Au(I) in 0.1M sodium acetate pH 4.5, at 20 days, 30 days and 60 days after the drops were prepared.

According to Wei *et al.*, the growth of AuNPs inside the crystals would have originated from the spontaneous disproportionation of Au(I) to Au(III) and Au(0). The accumulation of Au(0) within the crystals would then result in the growth of the AuNPs<sup>56</sup>.

Thermodynamically speaking, by looking at gold's half-reactions we would have:



Since, according to Equation 1

$$\Delta G_r^0 = -nFE^0 \quad \text{Equation 1}$$

a reaction that is spontaneous possesses a negative  $\Delta G_r^0$ , consequently having a positive  $E^0$ <sup>78</sup>. Hence, the spontaneous disproportionation of Au(I) into Au(III) and Au(0) would be quite possible, allowing then the growth of AuNPs from the accumulation of the Au(0).

Although the AuNPs had formed within HEWL crystals, its isomorphism remained intact through the growth process. The resultant crystals presented the tetragonal crystalline structure normally seen for HEWL<sup>49,50</sup>, allowing its study by X-ray diffraction techniques, which included the calculation of simple  $F_{\text{obs}} - F_{\text{calc}}$  and  $2F_{\text{obs}} - F_{\text{calc}}$  difference maps.

### 3.2.2. TEM analysis

With the intent to obtain further evidences that AuNPs had in fact grown inside HEWL crystals, TEM images were collected from a sample of crystals with 30 days of growth, previously dissolved in Milli-Q water.

The presence of gold nanoparticles within the protein crystals was in fact evidenced by the TEM measurements, where the presence of a mix population of spherical gold nanoparticles and gold dendrites was detected (Figure 3.24). The dendritic species might have resulted from the reduction of the gold compound by the TEM grid, and were not necessarily initially present in the AuNPs solution.

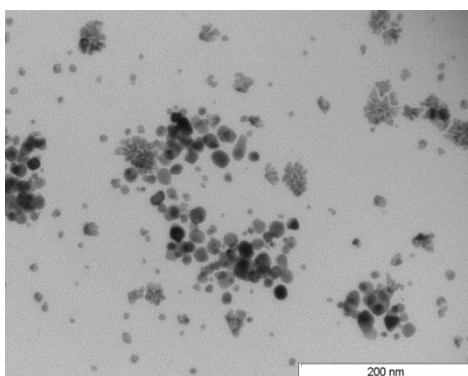


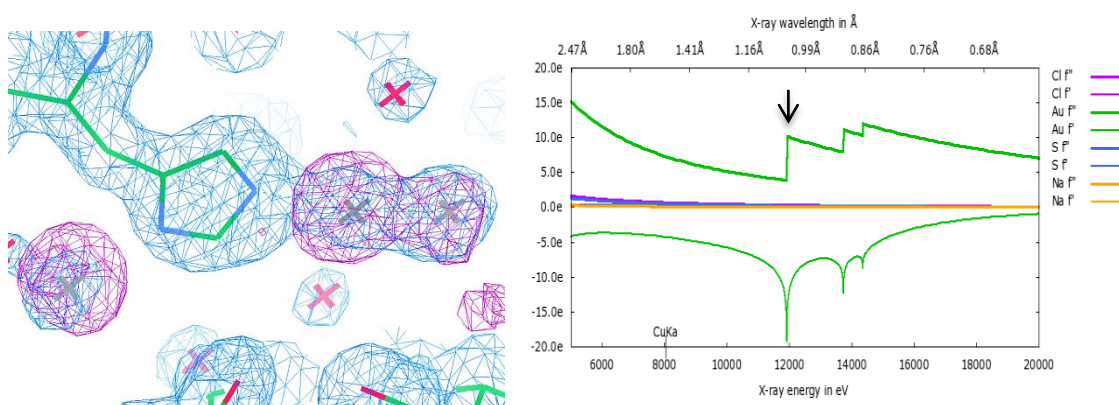
**Figure 3.24.** Electron micrographs of the HEWL crystals grown in the presence of Au(I).

Due to the high heterogeneity of the gold population observed, it was not possible to calculate a size distribution histogram for TEM images obtained, but, by visual measurement, the spherical gold nanoparticle seemed to range from sizes of 19.4 nm to 6.5 nm. These size measurements were actually similar to what was reported by Wei *et al*<sup>66</sup>.

Nevertheless, these results came to reinforce the notion that AuNPs had in fact been formed within the protein crystals, as its colour evolution from colourless to dark red implied (subsection 3.2.1.).

### 3.2.3. Structural analysis by X-ray crystallography

The crystals obtained from the co-crystallization experiments of HEWL with Au(I) were then measured by X-ray diffraction techniques at 20, 30, 40 and 60 days of growth, at the chosen wavelength of 1.038 Å, near the  $L_{III}$  X-ray absorption edge of gold, in order to take advantage of the gold's scattering properties. It was then possible to identify atomic gold at the surface of HEWL structures. An electron density map calculated from the anomalous differences of the intensities allowed to unambiguously identify the positions of the gold atoms (Figure 3.25).

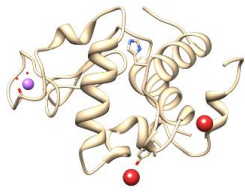
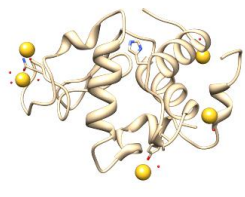
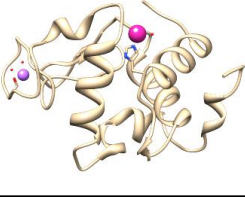
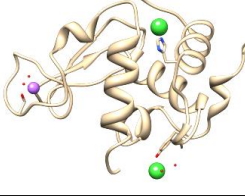
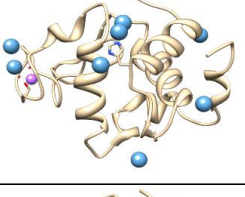
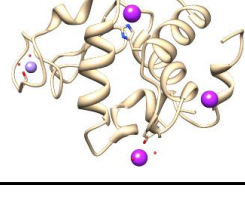


**Figure 3.25.** Electron density map obtained from one of the HEWL-Au(I) crystals measured, showing the anomalous signal (purple density) that allowed identifying the position of the gold atoms. In the left, is presented the diagram used to predict the anomalous scattering factors for gold atoms used to calculate the anomalous differences of the intensities at 1.038 Å.

From the ten crystals measured using synchrotron radiation, eight datasets were collected with quality data and from those, six HEWL structures were solved holding gold atoms at its surface two for each time line (Figure 3.26) (see Appendix D, Table D.1 for the respective refinement statistics), refined to a resolution range of 1.36 to 1.60 Å. Although the identified gold atoms only presented partial occupancy, its presence was clear, due to the high anomalous signal centred on its electronic density. However, it was not possible to establish a time-dependent growth of the AuNPs within HEWL crystals, like described by Wei and co-workers<sup>56</sup>. Controversially, those authors did not present any evidence of the use of anomalous signal to confirm the identity the gold atoms within the crystals structures. Additionally, analysis of the deposited structures on PDB (3P4Z, 3P64, 3P65, 3P66 and 3P68) showed that only a much smaller number of atomic positions could be attributed to gold (see Appendix E, Table E.1 for the revised heteroatoms present in those structures).

From the structures obtained in this project, a highly variable number of gold atoms were identified at the surface of HEWL structures disregarding for the crystal growth time (Figure 3.26). However, a feature that was always observed was the presence and interaction of one gold atom through the  $N\epsilon$  of HEWL's single histidine (His15) between 2.14 and 2.54 Å (Au1), which has been described as a common binding site for metals<sup>50,54-59</sup> (see subsection 1.6.).

Interestingly, that gold atom was only present in the structures solved from the crystals at 40 and 60 days of growth, not being detected in the structures at 20 days.

20 days		Au atoms	1	2						
		Occupancy	0.25	0.22						
		B-factor	20.85	24.16						
		Interaction								
		Au atoms	1	2	3	4	5			
		Occupancy	0.19	0.24	0.26	0.18	0.20			
B-factor		20.06	18.47	18.84	21.05	22.57				
Interaction										
40 days		Au atoms	1							
		Occupancy	0.25							
		B-factor	18.96							
		Interaction	His 2.52Å							
		Au atoms	1	2						
		Occupancy	0.23	0.28						
B-factor		45.65	20.73							
Interaction		His 2.54Å								
60 days		Au atoms	1	2	3	4	5	6	7	8
		Occupancy	0.12	0.19	0.23	0.21	0.23	0.25	0.21	0.1
		B-factor	23.35	24.29	27.44	18.08	14.33	18.18	25.21	22.80
		Interaction	His 2.14Å	Au 1 2.18Å						
		Au atoms	1	2	3					
		Occupancy	0.14	0.26	0.23					
		B-factor	24.66	18.51	20.50					
		Interaction	His 2.47Å							

**Figure 3.26.** Summary of the HEWL structures solved from the crystals grown in the presence of Au(I) after 20, 40 and 60 days of growth. The gold atoms for each structure are depicted with distinctive colours, and the identified Na atoms are represented in light purple. The information regarding the gold atoms identified at the surface of HEWL's structures is presented on the side table.

These observations were basically the opposite to what it was reported by Wei and co-workers<sup>56</sup>, where the gold atom interacting with His15 was present within HEWL structures for the crystals measured at one, two and three days of growth and was not detected after 90 days. Also, for one of the structures solved at 60 days of growth, additional to the gold atom bound to the histidine, a second one was identified bound to the first gold atom at a distance of 2.18Å



(Au2). The distances calculated for the gold atoms interacting with histidine's N $\epsilon$  and between those two gold atoms, were well within the range of N-Au and Au-Au bond lengths in structures deposited in the Cambridge Structural Database (CSD). From a total of fifteen structures searched, distances between nitrogen and a gold atom were found to be between 2.12 to 2.56, and 2.05 to 2.77 between two gold atoms.

As Au1 and Au2 were almost in a linear geometry with the N $\epsilon$  with an angle of 167.1 $^\circ$  (see Appendix F, Figure F.1), Au1 would possibly have a valence of +1. However, any coordination ligands were observed between the remaining gold atoms and HEWLs' residues, making it difficult to assign their valence state.

By superimposing all the six HEWL structures obtained, it could be observed that the gold atoms tended to cluster into a few specific sites at the protein's surface (Figure 3.27). Overall, seven assembling spots for atomic gold could be identified at the surface of HEWL, including the binding spot to the histidine residue. The highest number of gold atoms has been observed at the His15 site and at B and C positions.

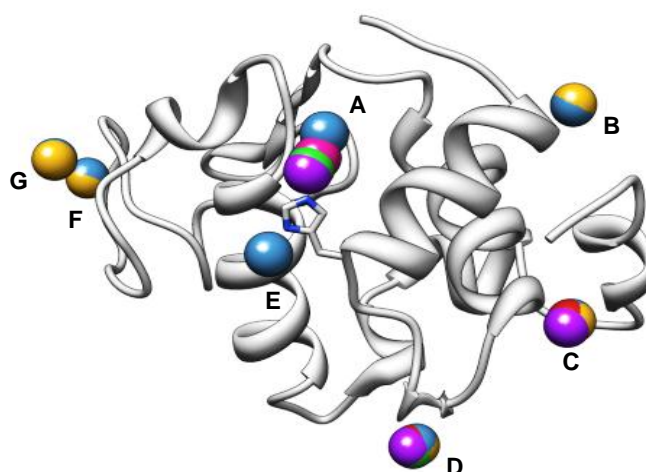


**Figure 3.27.** Superimposition of the six HEWL structures solved from the crystals grown in the presence of Au(I) after 20, 40 and 60 days of growth, produced using Chimera. HEWL structure is shown in ribbon representation and the gold atoms for each structure are represented as spheres in different colours. The letters indicate the different sites where the gold atoms were found.

The position at the His15 residue is a well known binding site for a variety of metal ions and complexes<sup>50,54-59</sup>, which can explain the high number of gold atoms observed bound to His15 (site A) in this study. In site B, gold atoms were found to be in the vicinity of Lys33, at a distance of 3.250 Å. The metal atoms in site C were observed near Ser24 residues, at approximately 2.86 Å, where other metals had also been observed<sup>55,56</sup>. As also seen by Wei and co-workers<sup>56</sup>, a significant number of gold atoms were here found at site D, at an approximate distance of 2.93 Å of Tyr 23. Gold atoms observed in sites F and G were located in the vicinity of Asn65, at distances of 3.97 Å and 3.003 Å respectively, and site G was also near Ser72 at 3.47 Å, which were also reported sites for gold and other metals<sup>55,56</sup> (see Appendix F, Figure F.1).

Analysis of HEWLs' crystal lattice was then carried out with the intent to overview how the atomic gold observed in the protein structures was distributed throughout the crystals (Figure 3.28).

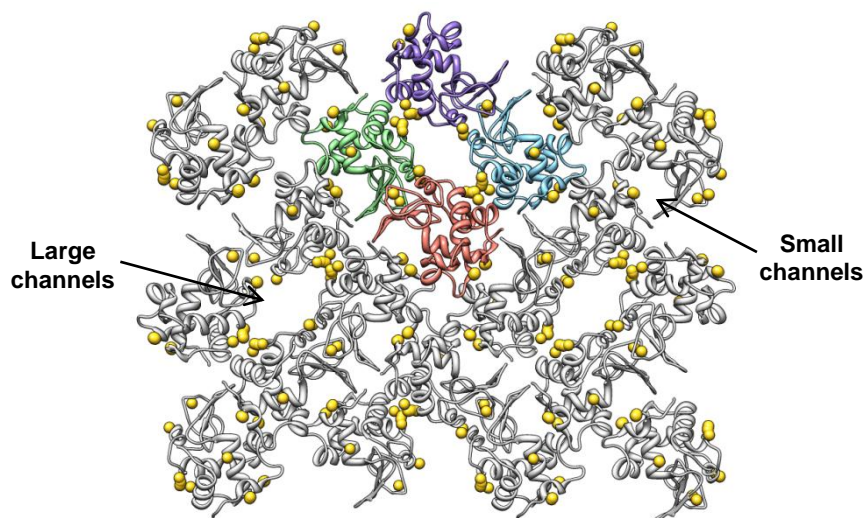


**Figure 3.28.** Crystal lattice of HEWL tetragonal crystals grown in the presence of Au(I), evidencing the distribution of the gold atoms inside the crystals, produced using Chimera. HEWL structures are drawn in ribbon representation, and four of its monomers are shown in distinctive colours. Gold atoms are represented as spheres depicted in yellow. HEWL crystals' small and large solvent channels are pointed. Image produced using Chimera.

By analysing the crystal lattice of HEWLs' crystals grown with Au(I) (Figure 3.28), the majority of the gold atoms were observed at the surface of the large solvent channels, where the His15 binding site was located, although a few were also detected within the small channels. Also, as seen previously in the structures from the crystals co-crystallized with AuNP-PVP (subsection 3.1.1.7., Figure 3.14), the metal atoms were clustered in the contact areas between the protein molecules assembled into the crystal. It would be expected to observe an accumulation of the gold atoms within the crystals' solvent channels, given that the Au(I) solution would have incorporated the crystals through these channels and then spontaneously disproportionate into Au(III) and Au(0). The Au(III) and Au(0) accumulated into the contacts between the proteins' molecules near the solvent channels, which probably conferred a more chemically stable environment for the metal atoms, hence its great affinity towards these sites.

#### **3.2.4. Structural comparison between HEWL structures obtained in the presence of AuNP-PVP and Au(I)**

In order to analyze the positions of the determined gold atoms between the structures obtained by co-crystallization with Au(I) and with AuNP-PVP (subsection 3.1.1.7.), a superimposition of the resultant structures was carried out (Figure 3.29).

It was then observed that two of the three sites determined for gold in the structures solved from the crystals grown in the presence of AuNP-PVP corresponded exactly to sites E and C of the structures obtained from the crystals grown with Au(I) (Figure 3.27), in the vicinity of Asn65 and Tyr23 (see Appendix F, Figure F.1).

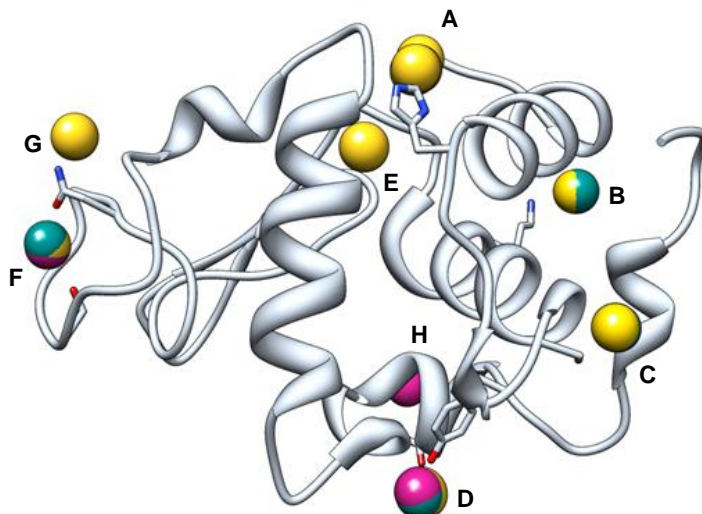


**Figure 3.29.** Superimposition of the HEWL structures solved from the crystals grown in the presence of Au(I) and AuNP-PVP, produced using Chimera. HEWL structure is shown in ribbon representation. The gold atoms are represented as spheres and depicted in violet and cyan corresponding to the structures obtained by co-crystallization and soaking experiments with AuNP-PVP, respectively, and in yellow corresponding to the crystals grown with Au(I). The letters indicate the different sites where the gold atoms were found.

Although no other specific interactions were detected between the gold atoms and HEWL, besides with the His15 residue, it was showed that gold has a great affinity to assemble at the protein's surface. This affinity would explain why it seemed that HEWL's crystals promoted an environment favourable to the formation and assembly of AuNPs. Although, HEWL is known to bind a variety of metal ions and complexes, and along these studies it seemed that gold atoms would bind randomly to the protein's surface, in the end we observed that the protein actually possesses a great number of possible binding sites for gold as well (see Appendix F, Figure F.1). Regarding the crystallographic method used to obtain these crystals, the determined structures revealed the presence of gold atoms in coincident sites for all three studies, which is the case of sites B, C, D and F. Surprisingly, the interaction of the gold atoms with His15, being this residue such a common metal binding site in HEWL, was only observed in the crystal structures obtained by co-crystallization with Au(I).



### **3.3. Project III**

## **Gold nanoparticles-induced protein crystal growth**



Previous studies, demonstrated that gold nanoparticles could act as nucleants for HEWL crystallization, promoting its crystal growth in conditions for which the enzyme alone was not able to form crystals, and also an increase in crystal size in some specific conditions, such as in the presence of 3nM AuNP-CALNN and AuNP-CALKK<sup>65</sup>.

In order to confirm those results, crystallization studies with HEWL in the presence of AuNPs were repeated. The previously used AuNP-MUA, AuNP-CALNN and AuNP-CALKK, AuNP-PEG was also employed in the present work. Since PEG is a common additive and precipitant agent used in crystallization studies, it would be interesting to test the effect of AuNPs functionalized with this polymer. The enzyme RNase was also used as a subject of test, with the intent to see if the AuNPs effects observed in HEWL crystal growth would also occur with RNase.

The potential of the gold nanoparticles-induced crystal growth was then explored by applying the method to several other proteins available in the laboratory and that have revealed to be reluctant to crystallization, or from which no well-diffracting crystals could be obtained. In total, eight proteins were tested: malectin, malectin-trime, native AOH, AOH-ΔHis and mutants Y885M and Y885F, YPS and PAH. With PAH interesting results were obtained. From the remaining proteins tested, no improvement on its crystallization was obtained and hence no results are here reported.

### **3.3.1. HEWL**

The previous studies were carried by screening each type of the AuNPs at concentrations of 1, 2, 3 and 4 nM against a range of HEWL concentrations from 25 to 50 mg/ml<sup>65</sup>. Although it was not possible to unequivocally determine the crystallization conditions that could be the most successful on improving HEWL crystals growth for the four AuNPs types, the conditions with 3nM of AuNPs for the lower HEWL concentrations allowed the best results<sup>65</sup>. Thus, this was the chosen concentration to work with in the present study. For HEWL, the concentration of 25 mg/ml was chosen (since being a limit concentration it is less prone to give crystals), for it would be easier to prove the induction of the crystal growth by the AuNPs against the control protein drops.

An important aspect worth to be pointed out, also accordingly to the previous results<sup>65</sup>, is that the addition of HEWL to the AuNPs solutions resulted in aggregation of the nanoparticles. After the overnight incubation, some solutions presented a purple deposit at the bottom of the tube. This purple precipitate resulted from the AuNPs aggregation and further precipitation, which was most significant for AuNP-MUA, AuNP-CALNN and AuNP-CALKK in the present study. Those precipitates were also present in the crystallization drops and for most cases the resulting crystals were formed on the same area where the precipitated AuNPs were present<sup>65</sup>.

In the present study, the control crystals were detected after four days of drop setup, while in the presence of AuNP-CALKK and AuNP-SPEG it took only two days for the crystals to grow.

On the other hand, the crystals grown in the presence of AuNP-MUA and AuNP-CALNN seemed to have appeared at the same time as the ones in the control drop (Figure 3.30). Furthermore, it was observed that in the presence of the AuNPs only single crystals grew in each drop, presenting also larger sizes, whereas in the control drop a higher number of smaller crystals were detected (Figure 3.30).

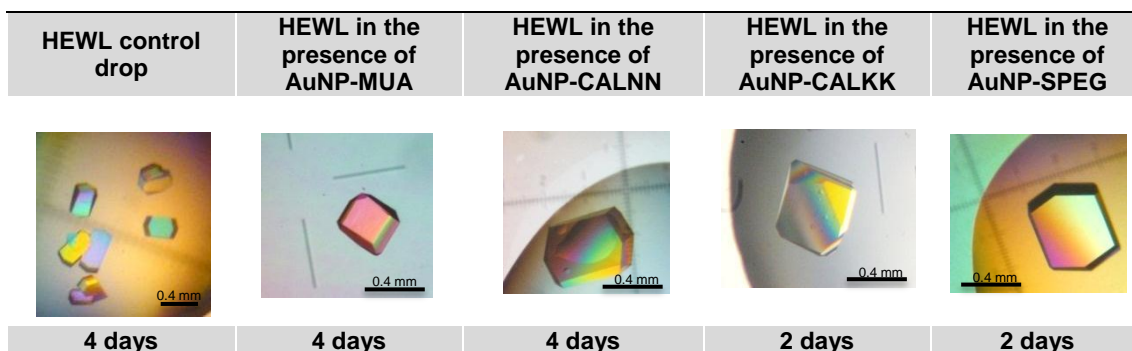


**Figure 3.30.** Microscope images of HEWL crystals (7x magnification) grown in the presence of AuNPs, using 25mg/mL of protein and 3nM of AuNPs in 50mM sodium acetate pH 4.5, and 50mM NaCl as precipitant, taken at the time of the crystals detection.

Comparing with the HEWL control, these results indicated that an improvement on crystal growth occurred specially in the presence of AuNP-CALKK and AuNP-PEG, with single crystals being formed prior to the control ones. However, the presence of AuNP-CALNN and AuNP-MUA also promoted the growth of single HEWL crystals, although taking as long as the control drop.

As a control for the crystals grown in the presence of AuNP-SPEG, drops were also made using PEG 200 as an additive, in order to clarify if the results observed would be due to the presence of PEG or if AuNPs also played a part in it. Since no crystals grew in the drop made with PEG 200, it could be inferred that the behaviour observed in HEWL crystallization in the presence of AuNP-PEG it was not entirely a result of the PEG influence as it was of its conjugation with the AuNPs.

Regarding the crystals isomorphism, the crystals grown in the presence of the AuNPs showed the tetragonal crystalline structure normally seen for HEWL, so the presence of the AuNPs did not disrupt HEWL's usual crystal lattice<sup>49,50</sup>.

These results confirmed the observations of the previous study<sup>65</sup>, reinforcing that AuNPs could in fact act as nucleating agents for the improvement of proteins crystal growth, stimulating the appearance of single crystals which are what it is most desirable for X-ray diffraction experiments.

HEWL possesses an overall positive surface potential, and a pI of 11.35<sup>74</sup>, therefore its residues' side chains would be predominantly positively charged at pH 4.5. As hypothesized



before<sup>65</sup>, the AuNPs, which are mostly all negatively charged, could easily interact electrostatically with the positive surface of HEWL, and after the aggregation and further precipitation of the AuNP-lysozyme aggregates, it could promote the reorganization of the remaining protein molecules improving crystal growth.

### 3.3.2. RNase

RNase single crystals, suitable for diffraction experiments, were only possible to obtain at the described conditions (subsection 2.3.1.), and those were the ones tested with the AuNPs in this study.

RNase crystals in the control drops (Figure 3.31) grew within three days, as observed for crystal grown in the presence of the AuNPs. Nevertheless, no crystals were detected in the drops made with AuNP-MUA. For the drops made with AuNP-CALNN and AuNP-CALKK, the number and sizes of the crystals obtained were similar to those on the control drop, however, in the presence of AuNP-SPEG two single crystals were detected (Figure 3.31). Although RNase crystalline structure proved to be strongly dependent on the crystallization conditions, it could be observed that the presence of AuNPs did not change its morphology.

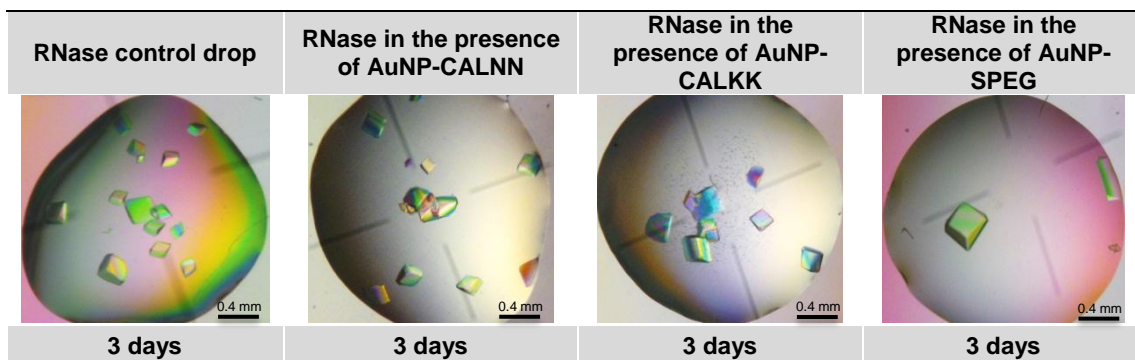


**Figure 3.31.** Microscope images of RNase crystals (5x magnification) grown in the presence of AuNPs, using 50mg/mL of protein and 3nM of AuNPs in 50mM sodium acetate pH 5.5 and 3M NaCl and 1.2M ammonium sulphate as precipitant.

Furthermore, while no induction or improvement of the crystallization process was observed for RNase crystals grown in the presence of AuNP-CALNN and AuNP-CALKK, an improvement of the nucleation process apparently occurred for the growth of the crystals in the presence of AuNP-PEG which allowed the protein molecules to assemble into slightly larger single crystals.

As a control for the crystals grown in the presence of AuNP-SPEG, drops were also made using PEG 200 as an additive, in order to exclude if the results observed would be solely due to the presence of PEG itself or the AuNPs also played a part in it. Since no crystals grew in the drop made with PEG 200, it could be inferred that the behaviour observed in RNase crystallization in

the presence of AuNP-SPEG was not entirely a consequence of the PEG influence as it was of its conjugation with the AuNPs.

Like HEWL, RNase possesses an overall positive surface potential. With an isoelectric point of 9.6<sup>79</sup>, its residues' side chains would also be predominantly positively charged at pH 5.5. Herein, the negatively charged AuNPs would interact electrostatically with the positive surface of RNase, and although no aggregation and precipitation of the AuNPs was seen, it could promote the reorganization of the protein molecules promoting the growth of single crystals. However, this hypothesis could only explain what happened in the drop made with AuNP-PEG, where an induction of the crystals growth seemed to have occurred, which was not observed in the presence of the other AuNPs.

### 3.3.3. Phenyl Alanine Hydroxylase (PAH)

Although PAH crystallization conditions were already known and used in the laboratory, only very small, multiple and poorly diffracting crystals were possible to obtain. Herein, the AuNPs were used as part of the optimization of PAH crystallization.

Since PAH crystals grew in less than twenty four hours resulting in high number of small crystals, its concentrations were lowered from 8.6mg/mL to 5mg/mL with the attempt to slow down the crystal growth and try to obtain fewer and maybe bigger crystals. Bigger drops were also tried.

For the crystals grown in the presence of AuNP-CALNN, AuNP-CALKK in 3 $\mu$ L drops and of AuNP-MUA in 6 $\mu$ L drop a slightly improvement was observed. A smaller number of crystals grew in the presence of the AuNPs, also looking less multiple, although still small (Figure 3.32).

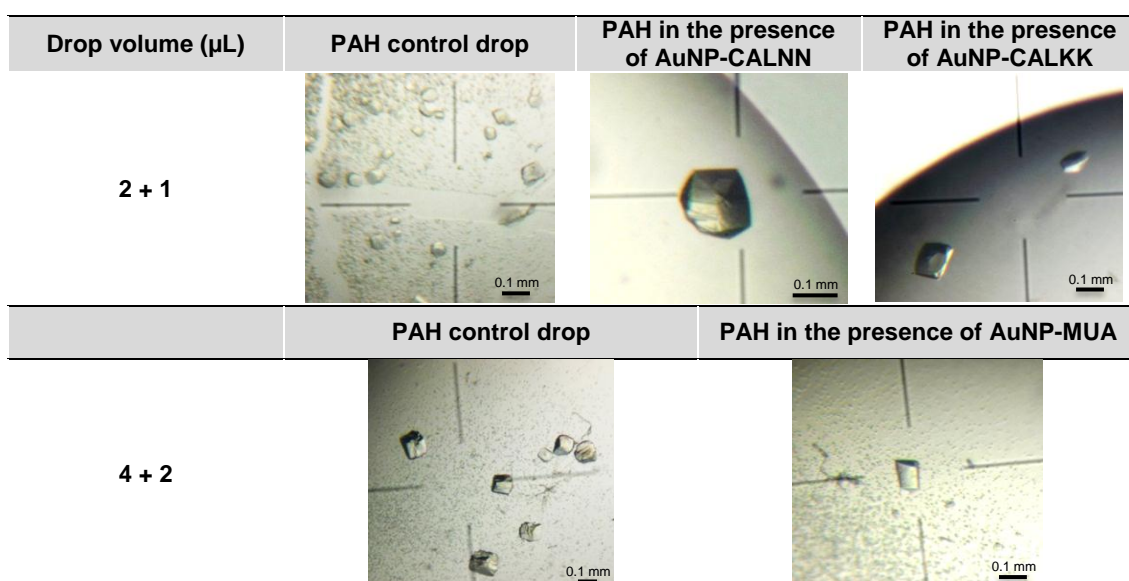


**Figure 3.32.** Microscope images of PAH crystals (7x magnification) grown with optimized crystallization conditions in the presence of AuNPs.

Several of those PAH crystals were later tested for diffraction under synchrotron radiation, but no diffraction was obtained better than 4 Å, which impaired data integration and the confirmation of their isomorphism to the native crystals. Although, PAH crystallization process seemed to have slightly improved with the use of the AuNPs, the crystallization conditions need to be further optimized in order to obtain single crystals suitable for X-rays diffraction. Additionally, PAH crystallization behaviour seemed to be strongly dependent on its purification batch, and it has not been possible so far to reproduce the slight improvement obtained in the first crystallization experiments with the AuNPs with the subsequent batches of the protein. Hence, we were not able to understand which type of AuNPs, between AuNP-CALNN, AuNP-CALKK and AuNP-MUA, that might have had the most success on improving PAH crystals.

In order to solve PAH's crystal structure, it would be very important to obtain better and independent phases. Therefore, it would also be interesting to attempt the incorporation of AuNP-PVP in PAH crystals, like was confirmed in HEWL, as a way to produce a heavy metal derivative to take advantage of Au's anomalous scattering.

Overall, taking into account the results observed for the three proteins described above and in the previous sections (subsections 3.3.1. and 3.3.2.), it was not possible to unequivocally determine a crystallization condition incorporating a type of AuNPs that could be the most successful on improving proteins crystal growth. The response of the proteins crystallization behaviour in the presence of each type of AuNPs might be intrinsically related with its overall surface charge towards the AuNPs surface potential, which would then influence the nucleation process. So for a certain protein, one type of AuNPs could show some improvement on its crystal growth, while having no effect at all on another protein. However, regarding solely the tests with HEWL and RNase, the AuNP-PEG seemed to have the same positive effect in the induction of both proteins crystal growth, making this AuNP functionalization type a good candidate for future crystallization experiments.



# **CHAPTER 4**

---

## **Conclusions**



Considering that the objectives of this work were to study the crystallization of proteins in the presence of AuNPs and their structural interactions with the AuNPs and gold atoms, to pursue the hypothesis of producing gold derivatives of protein crystals using AuNPs and to explore the potential of gold nanoparticles-induced crystal growth, it can be stated that those goals have been achieved.

HEWL crystals were produced exhibiting AuNP-PVP assembled within its growth sectors (Project I), visually detected by the crystals' red colouration, either by co-crystallization or by soaking experiments. TEM analysis confirmed the presence of spherical AuNPs inside these crystals, with average diameters of 22.3 to 28.5 nm. By spectroscopic studies and agarose gel electrophoresis it was not possible to observe if any interactions would occur between the protein and AuNP-PVP.

Unfortunately, RNase showed not to be a suitable protein for crystallization experiments with AuNP-PVP due to the high concentrations of ammonium sulphate used in the crystallization conditions.

Crystallization studies of HEWL with the Au(I) compound (Project II) fulfilled the initial objectives as well, as it was possible to observe the gradual growth of AuNPs within the protein crystals, as their colour changed from colourless to deep red. The formation of AuNPs inside the crystals was also confirmed by TEM measurements, in which populations of spherical AuNPs with average diameters of 6.5 to 19.4 nm could be detected.

High resolution X-ray diffraction data was collected from crystals obtained in the crystallization studies performed in Projects I and II, allowing to unambiguously identify several binding sites for gold atoms at HEWL structure's surface, by recurring to an electron density map calculated from the anomalous differences of the measured intensities at one of gold's X-ray absorption edges. As predicted, the His15 residue was observed as a common binding site for gold atoms, as this is a very usual site for the binding of metal species. Additionally, gold atoms were also identified in the vicinity of Asn65, Ser24, Asn113, Ser72, Lys33, Tyr23, mostly sites already frequently reported as HEWL metal binding sites of metal ions and complexes.

It is important to reinforce the idea that, although TEM results confirmed the incorporation and growth of AuNPs into the HEWL crystals, it was atomic gold that was identified in the protein crystallographic structures. Given that the AuNPs used in this work possess average diameters that are approximately ten times larger than HEWL, it would be nearly impossible to obtain a HEWL's crystal structure with AuNPs trapped within the protein molecules.

The gold nanoparticles-induced crystal growth approach (Project III), confirmed conclusions of the previous work performed by myself two years ago, although revealed not to be a very straight forward method. In fact, a type of AuNPs that seemed to improve a certain protein crystallization process would not have the same effect on another protein. However, regarding solely the tests with HEWL and RNase, AuNP-SPEG seemed to be a potentially good candidate

for future crystallization experiments. Additionally, a slight improvement of PAH crystallization was also observed, namely for crystals grown in the presence of AuNP-MUA and AuNP-CALKK, although it was not so far possible to obtain suitable PAH crystals diffracting under 4 Å.

In the matter of structure determination, crystallization studies with AuNP-PVP proved to be a promising method to produce heavy metal derivatives and it would be very interesting to test this method with other proteins, such as PAH.



## References

---



1. Pusey, M. L. *et al.* Life in the fast lane for protein crystallization and X-ray crystallography. *Progress in biophysics and molecular biology* **88**, 359–86 (2005).
2. Rupp, B. Biomolecular Crystallography: Principles, Practice, and Application to Structural Biology. *Garland Science* Chapter 3 (2009).
3. Rupp, B. Biomolecular Crystallography: Principles, Practice, and Application to Structural Biology. *Garland Science* Chapter 5 (2009).
4. Hodzhaoglu, F., Kurniawan, F., Mirsky, V. & Nanev, C. Gold nanoparticles induce protein crystallization. *Cryst. Res. Technol* **593**, 588–593 (2008).
5. Rhodes, G. Crystallography Made Crystal Clear, A Guide for Users of Macromolecular Models. *Elsevier Inc.* Chapter 6 (2006).
6. Alves, V. D. *et al.* Methods in ENZYMOLOGY. *Elsevier Inc.* **510**, Chapter 21 (2012).
7. Blasie, J. K. & Stamatoff, J. Resonance X-ray Scattering: Its Use in Determining Spatial Relationships Among Metal Atoms Within Macromolecules in a Non-Crystalline State. *Annual Review of Biophysics and Bioengineering* 451–458 (1981).
8. Rupp, B. Biomolecular Crystallography: Principles, Practice, and Application to Structural Biology. *Garland Science* Chapter 6 (2009).
9. Merritt, E. A. Anomalous Scattering Coefficients. *Biomolecular Structure Center at UW* at <[http://skuld.bmsc.washington.edu/scatter/AS\\_form.html](http://skuld.bmsc.washington.edu/scatter/AS_form.html)>
10. Marco, M. D. *et al.* Overview of the main methods used to combine proteins with nanosystems: absorption, bioconjugation, and encapsulation. *International Journal of Nanomedicine* 37–49 (2010).
11. Kim, J., Grate, J. W. & Wang, P. Nanobiocatalysis and its potential applications. *Trends in biotechnology* **26**, 639–46 (2008).
12. Kurniawan, F. New Analytical Applications of Gold Nanoparticles. 2–50 (2008).
13. Cortez, J. *et al.* Bionanoconjugates of tyrosinase and peptide-derivatised gold nanoparticles for biosensing of phenolic compounds. *Journal of Nanoparticle Research* **13**, 1101–1113 (2010).
14. Baptista, P. V. *et al.* Chapter 11 – Nanoparticles in Molecular Diagnostics. *Progress in Molecular Biology and Translational Science* 427–488 (2011).
15. Baptista, P. *et al.* Gold nanoparticles for the development of clinical diagnosis methods. *Anal Bioanal Chem* **391**, 943–950 (2008).
16. Turkevich, J., Stevenson, P. C. & Hillier, J. New Analytical Applications of Gold Nanoparticles. *Discuss. Faraday Soc.* **11**, 55–75 (1951).
17. Kimling, J. *et al.* Turkevich Method for Gold Nanoparticle Synthesis Revisited Turkevich Method for Gold Nanoparticle Synthesis Revisited. *The Journal of Physical Chemistry* **110**, 15700–15707 (2006).
18. Gimeno, M. C. The Chemistry of Gold. *Modern Supramolecular Gold Chemistry: Gold-Metal Interactions and Applications* Chapter 1 (2008).

19. Daniel, M. & Astruc, D. Gold Nanoparticles: Assembly, Supramolecular Chemistry, Quantum-Size-Related Properties, and Applications toward Biology, Catalysis, and Nanotechnology. *Chem. Rev.* **104**, 293–346 (2004).
20. Baptista, P., Doria, G., Henriques, D., Pereira, E. & Franco, R. Colorimetric detection of eukaryotic gene expression with DNA-derivatized gold nanoparticles. *Journal of Biotechnology* **119**, 111–117 (2005).
21. Radwan, S. H. & Azzazy, H. M. Gold nanoparticles for molecular diagnostics. *Expert Rev Mol Diagn* **9**, 511–524 (2009).
22. Hasenoehrl, C., Alexander, C. M., Azzarelli, N. N. & Dabrowiak, J. C. Enhanced detection of gold nanoparticles in agarose gel electrophoresis. *Electrophoresis* **33**, 1251–4 (2012).
23. Cortie, M. . & McDonagh, A. Nanoscience of Gold and Gold Surfaces. *Gold Chemistry, Applications and Future Directions in the Life Sciences* Chapter 7 (2009).
24. Blaber, M. G., Ford, M. J. & Cortie, M. B. The Physics and Optical Properties of Gold. *Gold, Science and Applications* Chapter 2 (2010).
25. Lévy, R. Peptide-Capped Gold Nanoparticles : Towards Artificial Proteins. *Chem. Bio. Chem.* 1141–1145 (2006).doi:10.1002/cbic.200600129
26. Oura, K. *Surface Science, An Introduction*. (Berlin: Springer: 2003).
27. Koopal, L. K. *Manual of symbols and terminology for physicochemical quantities and units, Appendix II: Definitions, Terminology and Symbols in Colloid and Surface Chemistry, Part I* Manual of symbols and terminology for physicochemical quantities and units, Appendix II: (2001). at <[http://old.iupac.org/reports/2001/colloid\\_2001/manual\\_of\\_s\\_and\\_t/manual\\_of\\_s\\_and\\_t.html](http://old.iupac.org/reports/2001/colloid_2001/manual_of_s_and_t/manual_of_s_and_t.html)>
28. Pimpang, P. & Choopun, S. Monodispersity and Stability of Gold Nanoparticles Stabilized by Using Polyvinyl Alcohol. *Chiang Mai J. Sci.* **38**, 31–38 (2011).
29. Quaresma, P., Soares, L., Miranda, A. & Franco, R. Green photocatalytic synthesis of stable Au and Ag nanoparticles. *Green Chem.* **11**, 1889–1893 (2009).
30. Ma, H. *et al.* Synthesis of Silver and Gold Nanoparticles by a Novel Electrochemical Method. *Chem. Phys.Chem.* 68–75 (2004).
31. Schwerdtfeger, P. & Lein, M. Theoretical Chemistry of Gold – From Atoms to Molecules, Clusters, Surfaces and the Solid State. *Gold Chemistry, Applications and Future Directions in Life Sciences* Chapter 4 (2009).
32. Korobushkina, E. D., Karavaiko, G. I. & Korobushkin, I. M. Biochemistry of Gold. *Ecological Bulletins* 325–333 (1983).
33. Merchant, B. Gold, the noble metal and the paradoxes of its toxicology. *Biologicals : journal of the International Association of Biological Standardization* **26**, 49–59 (1998).
34. Pacheco, E. A., Tiekink, E. R. T. & Whitehouse, M. W. Gold Compounds and Their Applications in Medicine. *Gold Chemistry, Applications and Future Directions in Life Sciences* Chapter 6 (2009).

35. Skoog, Holler & Nieman Principles of Instrumental Analysis. *Harcourt College Publishers* Chapter 13 (1998).
36. Gomes, I. *et al.* Probing Surface Properties of Cytochrome c at Au Bionanoconjugates. *J. Phys. Chem. C* **112**, 16340–16347 (2008).
37. Malvern Zeta Potential: An Introduction in 30 Minutes. *Zetasizer Nano series technical note MRK654-01*
38. Malvern Zeta potential measurement using laser Doppler electrophoresis (LDE). accessed at July 30th (2010). at <[http://www.malvern.com/LabEng/technology/zeta\\_potential/zeta\\_potential\\_LDE.htm](http://www.malvern.com/LabEng/technology/zeta_potential/zeta_potential_LDE.htm)>
39. Colloidal Dynamics The Zeta Potential. *Electroacoustics Tutorials* 1–4 (1999).
40. Malvern Zeta potential. accessed at July 30th (2010). at <[http://www.malvern.com/labeng/products/iwrm/zeta\\_potential.htm](http://www.malvern.com/labeng/products/iwrm/zeta_potential.htm)>
41. N, S. & PL, U. Electrophoretic methods for separation of nanoparticles. *J Sep Sci.* **32**, 1889–906 (2009).
42. Hanauer, M., Pierrat, S., Zins, I., Lotz, A. & Sönnichsen, C. Separation of nanoparticles by gel electrophoresis according to size and shape. *Nano letters* **7**, 2881–5 (2007).
43. Patra, H. K., GuhaSarkar, D. & Dasgupta, A. K. Multimodal electrophoresis of gold nanoparticles: a real time approach. *Analytica chimica acta* **649**, 128–34 (2009).
44. López-Lorente, A. I., Simonet, B. M. & Valcárcel, M. Electrophoretic methods for the analysis of nanoparticles. *TrAC Trends in Analytical Chemistry* **30**, 58–71 (2011).
45. Guirgis, B. S. S. *et al.* Gold nanoparticle-based fluorescence immunoassay for malaria antigen detection. *Analytical and bioanalytical chemistry* **402**, 1019–27 (2012).
46. Niederstrasser, H. *Electron Microscopy For Dummies*. (Snaggled Works: 1999).at <[http://www.snaggledworks.com/em\\_for\\_dummies/background.html](http://www.snaggledworks.com/em_for_dummies/background.html)>
47. Rao, C. N. R. & Biswas, K. Characterization of nanomaterials by physical methods. *Annual review of analytical chemistry (Palo Alto, Calif.)* **2**, 435–62 (2009).
48. Goodsell, D. Lysozyme. *RCSB Protein Data Bank* (2000).doi:10.2210/rcsb\_pdb/mom\_2000\_9
49. Petrova, E., Dold, P. & Tsukamoto, K. Growth of tetragonal lysozyme crystals from solutions containing NaCl, CsCl and NaNO<sub>3</sub>. *Journal of Crystal Growth* **304**, 141–149 (2007).
50. Ueno, T. *et al.* Elucidation of metal-ion accumulation induced by hydrogen bonds on protein surfaces by using porous lysozyme crystals containing Rh(III) ions as the model surfaces. *Chem Eur J* **16**, 2730–40 (2010).
51. Blake, C. C. F. *et al.* Structure of hen egg-white lysozyme, a three dimensional fourier synthesis at 2-Ångstroms resolution. *Nature* **206**, 757–761 (1965).
52. Vocadlo, D. J., Davies, G. J., Laine, R. & Withers, S. G. Catalysis by hen egg-white lysozyme proceeds via a covalent intermediate. *Nature* **412**, 835–8 (2001).

53. Forsythe, E. L., H. Snell, E., Malone, C. C. & Pusey, M. L. Crystallization of chicken egg white lysozyme from assorted sulfate salts. *Journal of Crystal Growth* **196**, 332–343 (1999).
54. Santos-Silva, T. *et al.* CORM-3 reactivity toward proteins: the crystal structure of a Ru(II) dicarbonyl-lysozyme complex. *Journal of the American Chemical Society* **133**, 1192–5 (2011).
55. Abe, S. *et al.* Porous protein crystals as reaction vessels for controlling magnetic properties of nanoparticles. *Small (Weinheim an der Bergstrasse, Germany)* **8**, 1314–9 (2012).
56. Wei, H. *et al.* Time-dependent , protein-directed growth of gold nanoparticles within a single crystal of lysozyme. *NATURE NANOTECHNOLOGY* **6**, 93–97 (2011).
57. Panzner, M. J., Bilinovich, S. M., Youngs, W. J. & Leeper, T. C. Silver metallation of hen egg white lysozyme: X-ray crystal structure and NMR studies. *Chemical communications* **47**, 12479–81 (2011).
58. Binkley, S. L., Ziegler, C. J., Herrick, R. S. & Rowlett, R. S. Specific derivatization of lysozyme in aqueous solution with Re(CO)<sub>3</sub>(H<sub>2</sub>O)<sub>3</sub>(+). *Chemical communications* **46**, 1203–5 (2010).
59. Razavet, M. *et al.* Tricarbonylmanganese(I)-lysozyme complex: a structurally characterized organometallic protein. *Chemical communications* **3**, 2805–7 (2007).
60. Goodsell, D. S. Ribonuclease A. *RCSB PDB Molecule of the Month* (2008).
61. Raines, R. T. Ribonuclease A. *Chem. Rev.* **98**, 1045–1065 (1998).
62. Marshall, G. R., Feng, J. A. & Kuster, D. J. Back to the future: Ribonuclease A. *Biopolymers* **90**, 259–77 (2008).
63. Kunitz, M. Crystalline Ribonuclease. *The Journal of General Physiology* **24**, 15–32 (1940).
64. Takeda, Y., Kondow, T. & Mafuné, F. Self-assembly of gold nanoparticles in protein crystal. *Chemical Physics Letters* **504**, 175–179 (2011).
65. Ribeiro, D. Crystallographic Studies of Lysozyme in the Presence of Gold Nanoparticles. (2010).
66. Haiss, W., Thanh, N. T. K., Aveyard, J. & Fernig, D. G. Determination of size and concentration of gold nanoparticles from UV-vis spectra. *Analytical chemistry* **79**, 4215–21 (2007).
67. McCleskey, T. M., Mizoguchi, T. J., Richards, J. H. & Gray, H. B. Electronic Spectroscopy of Gold(I) Pseudomonas aeruginosa Azurin Derivatives. *Inorg. Chem.* **35**, 3434–3435 (1996).
68. Leslie, A. G. W. Recent changes to the MOSFLM package for processing film and image plate data. *CCP4 and ESF-EAMCB Newsletter on Protein Crystallography* **26**, (1992).
69. Kabsch, W. XDS. *Acta Cryst D Biol Cryst* **66**, 125–132 (2010).
70. Collaborative Computational Project. Number 4 (1994).

71. Adams, P. D. PHENIX: a comprehensive Python-based system for macromolecular structure solution. *Acta Cryst Section D* **66**, 213–221 (2010).
72. Emsley, P. Features and development of Coot. *Acta Cryst Section D* **66**, 486–501 (2010).
73. EF, P. *et al.* UCSF Chimera: a visualization system for exploratory research and analysis. *J Comput Chem* **25**, 1605–1612 (2004).
74. Wetter, L. R. & Deutsch, H. F. Immunological studies on egg white proteins: IV. Immunological and physical studies of Lysozyme. *J. Biol. Chem.* **192**, 237–242 (1951).
75. Kowacz, M. *et al.* Hofmeister effects of ionic liquids in protein crystallization: direct and water-mediated interactions. *CrystEngComm* **14**, 4912–4921 (2012).
76. Fedorov, A. A. *et al.* Ionic interactions in crystalline bovine pancreatic ribonuclease A. *Biochemistry* **35**, 15962–79 (1996).
77. Park, C., Schultz, L. W. & Raines, R. T. Contribution of the Active Site Histidine Residues of Ribonuclease A to Nucleic Acid Binding. *Biochemistry* **40**, 4949–4956 (2001).
78. Atkins, P. & Jones, L. Chemical Principles, The Quest for Insight. *W. H. Freeman and Company* 448–456 (2005).
79. Tanford, C. & Hauenstein, J. D. Hydrogen Ion Equilibria of Ribonuclease1. *J Am Chem Soc* **78**, 5287–5291 (1956).





# Appendix

---



## A. Zeta-potential measurements

**Table A1.**  $\zeta$ -potential values and respective standard deviations of the AuNP-PVP solution at a pH range from pH 4 to pH 10.

AuNP-PVP	Zeta Potential
pH 4	$-4.50 \pm 0.65$
pH 5	$-6.84 \pm 0.83$
pH 6	$-4.58 \pm 0.18$
pH 7	$-5.06 \pm 0.98$
pH 8	$-13.90 \pm 0.37$
pH 9	$-13.33 \pm 0.65$
pH 10	$-21.37 \pm 2.12$

## B. AuNP-PVP spectra from two different synthesis batches

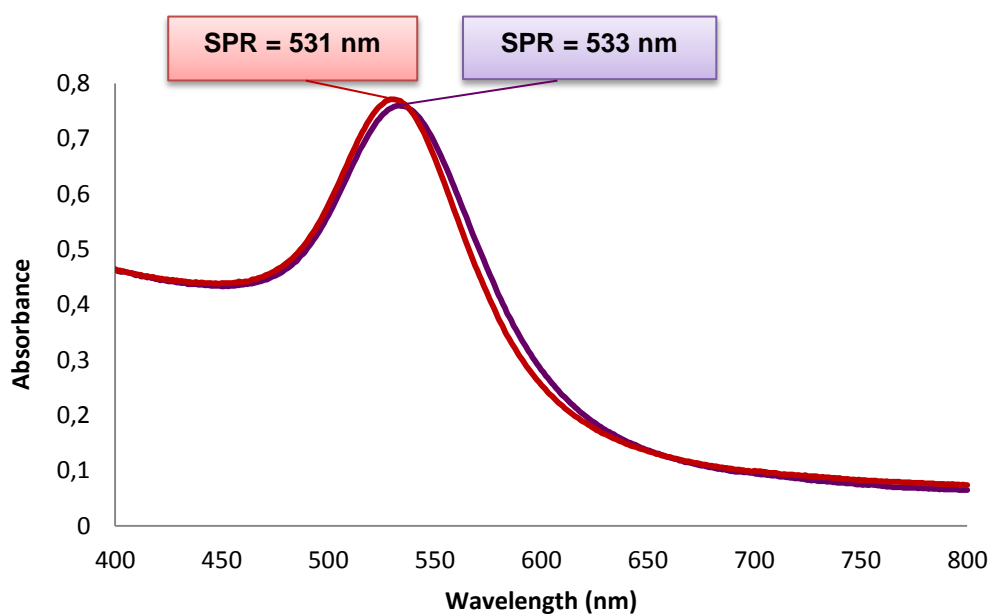


**Figure B.1.** AuNP-PVP spectra from two distinct synthesis batches evidencing a slight deviation of the SPR band regarding the two solutions and the respective AuNPs sizes determined through Haiss *et al.* method<sup>66</sup>.

AuNPs diameter and concentration was determined according to the Haiss *et al.* method<sup>66</sup>, as follows:

The diameter of the AuNPs is measured by ratio between the absorbance at the SPR band and the absorbance at 450 nm (Equation B.1):

$$d = \frac{Abs_{SPR}}{Abs_{450\text{ nm}}} \quad \text{Equation B.1}$$

The concentration is then calculated through a calibration curve, which relates the AuNPs diameter with the extinction coefficient ( $\epsilon$ ), and the Lambert-Beer equation (Equation B.2):

$$c = \frac{Abs_{450\text{ nm}}}{\epsilon_{450\text{ nm}}} \quad \text{Equation B.2}$$

**C. Data collection and processing statistics for the preliminary structural analysis of HEWL crystals co-crystallized and soaked with AuNP-PVP**

**Table C.1.** Data collection and processing statistics for the preliminary structural analysis of HEWL crystals co-crystallized with AuNP-PVP using: **(A)** 25 mg/mL of protein in 50mM of sodium acetate pH 4 and 5% NaCl; **(B)** 50 mg/mL of protein in the same buffer and 4% NaCl; and **(C)** 35 mg/mL of protein in 50mM of Boric Acid pH 8 and 5% NaCl.

<i>Crystal Data</i>	<b>A</b>	<b>B</b>	<b>C</b>
<b>Space Group</b>	P4 <sub>3</sub> 2 <sub>1</sub> 2	P4 <sub>3</sub> 2 <sub>1</sub> 2	P4 <sub>3</sub> 2 <sub>1</sub> 2
<b>Unit Cell</b>			
<b>a (Å)</b>	78.21	77.73	77.45
<b>b (Å)</b>	78.21	77.73	77.45
<b>c (Å)</b>	37.27	37.11	37.47
<b>α (o)</b>	90.00	90.00	90.00
<b>β (o)</b>	90.00	90.00	90.00
<b>γ (o)</b>	90.00	90.00	90.00
<b>Data collection statistics</b>			
<b>Wavelength (Å)</b>	0.861	0.861	0.861
<b>Resolution (Å)</b>	20.61-1.50 (1.58-1.50)	20.49-1.37 (1.37-1.44)	15.7-1.05 (1.11-1.05)
<b>Total number of reflections</b>	83769	138251	254194
<b>Number of unique reflections</b>	18697	46600	53371
<b>R<sub>merge</sub></b>	0.619 (7.0)	0.066 (0.357)	0.057 (0.40)
<b>Redundancy</b>	4.5 (4.6)	3.0 (2.9)	4.8 (3.7)
<b>Completeness (%)</b>	98.2 (99.7)	99.4 (99.1)	99.5 (99.1)
<b>I/σ(I)</b>	10.7 (2.4)	8.7 (2.5)	12.5 (2.5)

**Table C.2.** Data collection and processing statistics for the preliminary structural analysis of HEWL crystals soaked with AuNP-PVP at pH 4 and at pH 8.

<i>Crystal Data</i>	<b>pH 4</b>	<b>pH 8</b>
<b>Space Group</b>	P4 <sub>3</sub> 2 <sub>1</sub> 2	P4 <sub>3</sub> 2 <sub>1</sub> 2
<b>Unit Cell</b>		
<b>a (Å)</b>	78.31	77.43
<b>b (Å)</b>	78.31	77.43
<b>c (Å)</b>	37.09	37.33
<b>α (°)</b>	90.00	90.00
<b>β (°)</b>	90.00	90.00
<b>γ (°)</b>	90.00	90.00
<b>Data collection statistics</b>		
<b>Wavelength (Å)</b>	1.038	1.038
<b>Resolution (Å)</b>	39.16 - 1.38 (1.45 - 1.38)	38.72 - 1.38 (1.45 - 1.38)
<b>Total number of reflections</b>	253147	274053
<b>Number of unique reflections</b>	24038	23784
<b>R<sub>merge</sub></b>	0.059 (0.317)	0.087 (0.341)
<b>Redundancy</b>	10.5 (5.8)	11.5 (8.7)
<b>Completeness (%)</b>	98.9 (94.3)	98.9 (92.4)
<b>I/σ(I)</b>	19.5 (3.9)	13.2 (3.2)

**D. Data collection and processing statistics for the preliminary structural analysis of HEWL crystals co-crystallized Au(I)**

**Table D.1.** Data collection and processing statistics for the preliminary structural analysis of HEWL crystals co-crystallized with Au(I) after 20, 40 and 60 days of growth.

<b>Crystal Data</b>	<b>20 days</b>		<b>40 days</b>		<b>60 days</b>	
<b>Space Group</b>	P4 <sub>3</sub> 2 <sub>1</sub> 2	P4 <sub>3</sub> 2 <sub>1</sub> 2	P4 <sub>3</sub> 2 <sub>1</sub> 2	P4 <sub>3</sub> 2 <sub>1</sub> 2	P4 <sub>3</sub> 2 <sub>1</sub> 2	P4 <sub>3</sub> 2 <sub>1</sub> 2
<b>Unit Cell</b>						
<b>a (Å)</b>	78.07	78.64	78.86	77.89	78.53	77.26
<b>b (Å)</b>	78.07	78.64	78.86	77.89	78.53	77.26
<b>c (Å)</b>	37.18	37.03	37.08	37.30	36.92	37.18
<b>α (°)</b>	90.00	90.00	90.00	90.00	90.00	90.00
<b>β (°)</b>	90.00	90.00	90.00	90.00	90.00	90.00
<b>γ (°)</b>	90.00	90.00	90.00	90.00	90.00	90.00
<b>Data collection statistics</b>						
<b>Wavelength (Å)</b>	1.038	1.038	1.038	1.038	1.038	1.038
<b>Resolution (Å)</b>	39.04 - 1.60 (1.69 – 1.60)	39.32 - 1.36 (1.43 – 1.36)	39.43 - 1.54 (1.63 – 1.54)	38.94 - 1.58 (1.67 – 1.58)	39.26 - 1.54 (1.62 – 1.54)	38.63 - 1.63 (1.72 – 1.63)
<b>Total number of reflections</b>	96162	144066	132176	93661	136324	107270
<b>Number of unique reflections</b>	15588	25272	17581	15472	17473	13661
<b>R<sub>merge</sub></b>	0.07 (0.186)	0.033 (0.251)	0.075 (0.237)	0.074 (0.191)	0.022 (0.047)	0.040 (0.110)
<b>Redundancy</b>	6.2 (6.1)	5.7 (4.6)	7.5 (7.0)	6.1 (4.0)	7.8 (8.1)	7.9 (7.1)
<b>Completeness (%)</b>	99.3 (99.9)	99.3 (95.6)	99.0 (97.7)	96.2 (81.1)	99.0 (96.9)	94.7 (94.2)
<b>I/σ(I)</b>	12.90 (4.8)	23.2 (4.7)	12.9 (4.6)	13.0 (3.5)	55.2 (29.8)	28.3 (11.2)

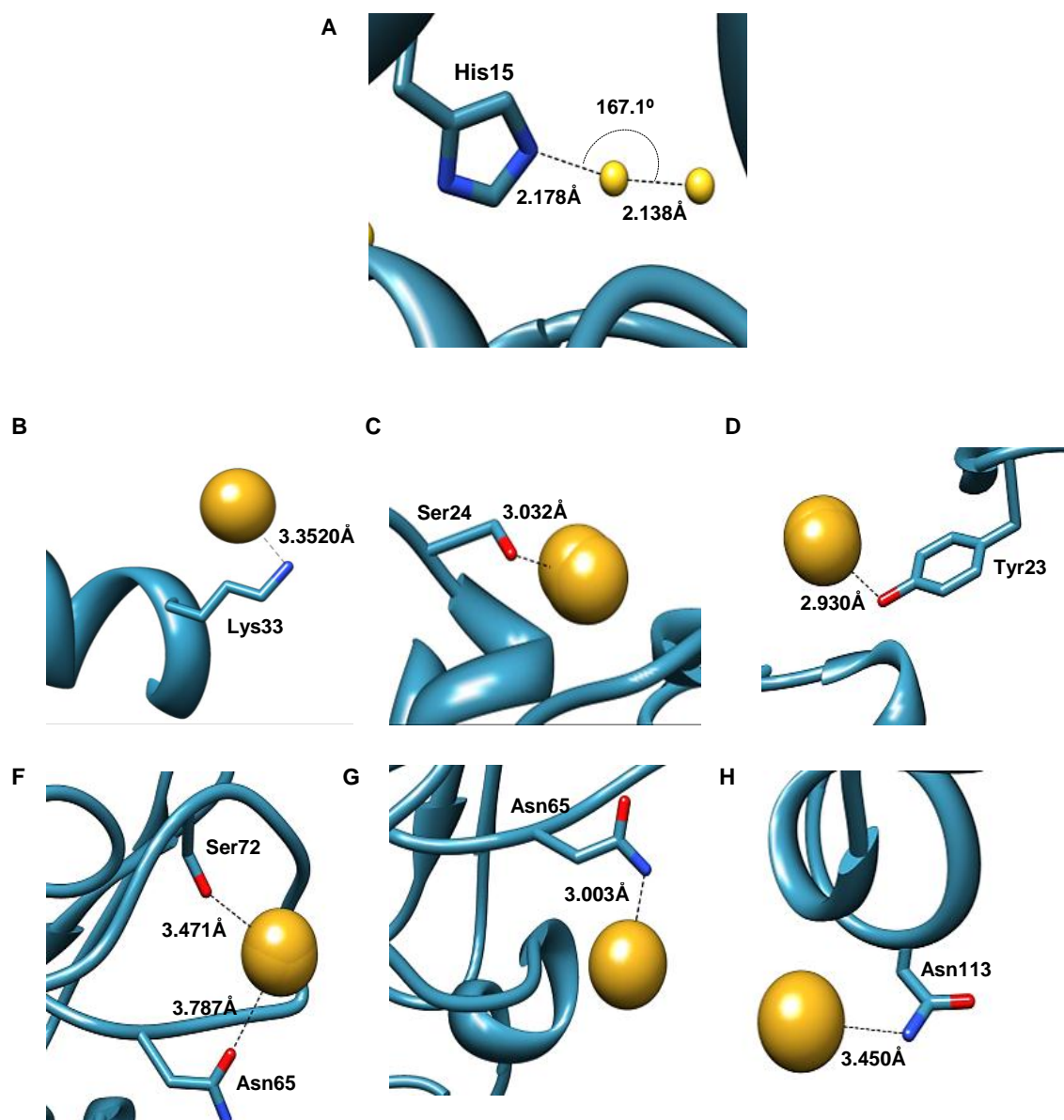
E. Revised heteroatoms from structures deposited on PDB by Wei *et al.*

Table E.1. Comparison between heteroatoms identified by Wei *et al.* in HEWL structures and the same positions refined by our group

Published										Corrected												
<b>Lys crystal grown with Au(I) - 1 Day (3P4Z)</b>																						
	Au1	Au2	Cl							R <sub>work</sub>	R <sub>free</sub>	Au	Cl	H <sub>2</sub> O					R <sub>work</sub>	R <sub>free</sub>		
B.F.	72.45	55.10	34.77							19.33	23.58	32.60	24.24	25.26					17.84	23.88		
Occ.	1.00	0.50	1.00									0.30	1.00	1.00								
A.A.	H15	Y23										H15										
<b>Lys crystal grown with Au(I) - 2 Days (3P64)</b>																						
	Au1	Au2	Au3	Au4	Cl					R <sub>work</sub>	R <sub>free</sub>	Au	Cl	Cl	Cl	H <sub>2</sub> O			R <sub>work</sub>	R <sub>free</sub>		
B.F.	62.15	53.98	66.21	53.22	26.75					20.20	23.41	32.78	21.10	20.08	16.25	15.79			17.00	18.47		
Occ.	0.50	1.00	1.00	0.50	1.00							0.18	1.00	1.00	1.00	1.00						
A.A.	H15	Y23	S24	R68								H15										
<b>Lys crystal grown with Au(I) - 3 Days (3P65)</b>																						
	Au1	Au2	Au3	Au4	Au5	Cl				R <sub>work</sub>	R <sub>free</sub>	Au	Cl	Cl	Cl	H <sub>2</sub> O	H <sub>2</sub> O		R <sub>work</sub>	R <sub>free</sub>		
B.F.	63.95	49.89	59.36	65.44	48.63	25.25				20.85	22.51	31.78	13.55	16.91	15.64	9.29	17.41		17.51	19.66		
Occ.	0.30	1.00	1.00	1.00	0.50	1.00						0.22	1.00	1.00	1.00	1.00	1.00					
A.A.	H15	Y23	S24	R68	R73							H15										
<b>Lys crystal grown with Au(I) - 90 Days (3P66)</b>																						
	Au1	Au2	Au3	Au4	Au5	Au6	Au7	Au8	Au9	R <sub>work</sub>	R <sub>free</sub>		Cl	Cl	Cl	Na	Cl	Cl	H <sub>2</sub> O	H <sub>2</sub> O	R <sub>work</sub>	R <sub>free</sub>
B.F.		48.48	57.10	48.98	50.76	63.92	75.94	55.59	59.31	21.59	24.33		5.72	8.11	4.36	5.48	10.27	11.54	1.94	5.48	17.34	20.78
Occ.		1.00	1.00	1.00	1.00	1.00	1.00	0.50	1.00				1.00	1.00	1.00	1.00	1.00	1.00	1.00	1.00		
A.A.		Y23	S24	R68	R73	N65	N65	T51	T43													
<b>Lys crystal grown with HAuCl<sub>4</sub> (3P68)</b>																						
	Au1	Au2	Au3	Au4	Au5	Au6	Au7			R <sub>work</sub>	R <sub>free</sub>		Cl	Cl	Cl	Cl	H <sub>2</sub> O	Cl	H <sub>2</sub> O		R <sub>work</sub>	R <sub>free</sub>
B.F.	62.52	61.02	71.38	70.85	45.65	79.51	48.02			21.66	25.50		19.75	18.80	24.24	23.61	13.52	26.90	9.98		18.31	21.93
Occ.	1.00	1.00	1.00	1.00	0.50	1.00	0.50						1.00	1.00	1.00	1.00	1.00	1.00	1.00			
A.A.																						



**F. Site motifs of the gold atoms identified within HEWL structures determined from crystals grown in the presence of AuNP-PVP and Au(I)**



**Figure F.1.** The site motifs of the gold atoms identified within HEWL structures determined from crystals co-crystallized and soaked with AuNP-PVP and Au(I). HEWL is represented in ribbon and gold atoms are depicted in yellow. The distances between the gold atoms and HEWL's residues are represented as dashed lines.